

# US Patent & Trademark Office

## Patent Public Search | Text View

---

United States Patent	12383155
Kind Code	B2
Date of Patent	August 12, 2025
Inventor(s)	Castro-Gonzalez; Carlos et al.

---

### Systems, devices and methods for non-invasive hematological measurements

---

#### Abstract

A system for non-invasive hematological measurements includes a platform to receive a body portion of a user and an imaging device to acquire a set of images of a capillary bed in the body portion. For each image, a controller detects one or more capillaries in the body portion of the finger to identify a first set of capillaries by estimating one or more attributes of each capillary (e.g., structural attributes, flow attributes, imaging attributes, or combinations thereof), wherein at least one attribute of each capillary meets a predetermined criterion. The controller also identifies a second set of capillaries from the first set of capillaries such that each capillary of the second set of capillaries is visible in a predetermined number of images of the set of images.

---

**Inventors:** Castro-Gonzalez; Carlos (Cambridge, MA), Butterworth; Ian (Somerville, MA), Bourquard; Aurelien (Cambridge, MA), Ferro; Alvaro Sanchez (Madrid, ES), Tucker-Schwartz; Jason (Melrose, MA), Pablo Trinidad; Alberto (Madrid, ES), Ledesma Carbayo; Maria J. (Madrid, ES), Vettenburg; Tom (Dundee, GB)

**Applicant:** Massachusetts Institute of Technology (Cambridge, MA); UNIVERSIDAD POLITECNICA DE MADRID (Madrid, ES)

**Family ID:** 66173433

**Assignee:** Massachusetts Institute of Technology (N/A, N/A); Universidad Politecnica De Madrid (Madrid, ES)

**Appl. No.:** 18/633176

**Filed:** April 11, 2024

#### Prior Publication Data

<b>Document Identifier</b>	<b>Publication Date</b>
US 20240277243 A1	Aug. 22, 2024

## Related U.S. Application Data

continuation parent-doc US 17666461 20220207 US 11963750 child-doc US 18633176  
continuation parent-doc US 16162006 20181016 US 11244452 20220208 child-doc US 17666461  
us-provisional-application US 62572738 20171016

---

## Publication Classification

**Int. Cl.:** **G06K9/00** (20220101); **A61B5/00** (20060101); **A61B5/026** (20060101); **A61B5/145** (20060101); **A61B5/1455** (20060101); **G06T7/00** (20170101); **G06V40/10** (20220101); **G06V40/14** (20220101)

## U.S. Cl.:

**CPC** **A61B5/0261** (20130101); **A61B5/14546** (20130101); **A61B5/1455** (20130101); **A61B5/489** (20130101); **A61B5/6826** (20130101); **A61B5/7203** (20130101); **A61B5/7267** (20130101); **G06T7/0014** (20130101); **G06V40/10** (20220101); **A61B2576/02** (20130101); **G06T2207/10016** (20130101); **G06T2207/10152** (20130101); **G06T2207/20081** (20130101); **G06T2207/20084** (20130101); **G06T2207/30101** (20130101); **G06V40/14** (20220101); **G06V40/15** (20220101); **Y02A90/10** (20180101)

## Field of Classification Search

**CPC:** **A61B (5/0261); A61B (5/14546); A61B (5/1455); A61B (5/489); A61B (5/6826); A61B (5/7203); A61B (5/7267); A61B (2576/02); G06T (7/0014); G06T (2207/10016); G06T (2207/10152); G06T (2207/20081); G06T (2207/20084); G06T (2207/30101); G06T (7/0012); G06V (40/10); G06V (40/14); G06V (40/15); Y02A (90/10); G16H (50/70)**

---

## References Cited

### U.S. PATENT DOCUMENTS

Patent No.	Issued Date	Patentee Name	U.S. Cl.	CPC
534211	12/1894	English	N/A	N/A
2548378	12/1950	Kleinfeld	N/A	N/A
2588528	12/1951	Howser	N/A	N/A
4425924	12/1983	Riva et al.	N/A	N/A
4694843	12/1986	Casenhiser	N/A	N/A
4998533	12/1990	Winkelman	600/479	A61B 5/14535
5068536	12/1990	Rosenthal	N/A	N/A
5077476	12/1990	Rosenthal	N/A	N/A
5086229	12/1991	Rosenthal et al.	N/A	N/A
5204532	12/1992	Rosenthal	N/A	N/A
5218207	12/1992	Rosenthal	N/A	N/A
5237178	12/1992	Rosenthal et al.	N/A	N/A
5362966	12/1993	Rosenthal et al.	N/A	N/A
5365066	12/1993	Krueger, Jr. et al.	N/A	N/A
5436455	12/1994	Rosenthal et al.	N/A	N/A
5452717	12/1994	Branigan et al.	N/A	N/A

5582705	12/1995	Yeung et al.	N/A	N/A
5596987	12/1996	Chance	N/A	N/A
5598842	12/1996	Ishihara	600/479	A61B 5/0261
5676143	12/1996	Simonsen et al.	N/A	N/A
5782757	12/1997	Diab et al.	N/A	N/A
5791345	12/1997	Ishihara et al.	N/A	N/A
5855212	12/1998	Walker	N/A	N/A
5926261	12/1998	Hoshino	N/A	N/A
5934278	12/1998	Ishihara	600/476	A61B 5/0261
5983120	12/1998	Groner	600/476	G01N 15/06
6041247	12/1999	Weckstrom et al.	N/A	N/A
6154285	12/1999	Teng et al.	N/A	N/A
6179159	12/2000	Gurley	N/A	N/A
6213952	12/2000	Finarov et al.	N/A	N/A
6246786	12/2000	Nishikiori et al.	N/A	N/A
6358208	12/2001	Lang et al.	N/A	N/A
6424851	12/2001	Berman et al.	N/A	N/A
6634367	12/2002	Abraham et al.	N/A	N/A
6687521	12/2003	Sato et al.	N/A	N/A
7477924	12/2008	Chin	N/A	N/A
8145286	12/2011	Arai et al.	N/A	N/A
8858429	12/2013	Mizuyoshi	600/118	A61B 1/0653
9556416	12/2016	Luscher et al.	N/A	N/A
9984277	12/2017	Castro-Gonzalez et al.	N/A	N/A
10433733	12/2018	Wang	N/A	A61B 5/14546
10485309	12/2018	Bonner	N/A	N/A
10952622	12/2020	Fine	N/A	A61B 5/165
11160492	12/2020	Butterworth	N/A	N/A
11244452	12/2021	Castro-Gonzalez et al.	N/A	N/A
11963750	12/2023	Castro-Gonzalez et al.	N/A	N/A
2001/0002431	12/2000	Gurley	N/A	N/A
2005/0209514	12/2004	Oshima et al.	N/A	N/A
2005/0268369	12/2004	Santiago	N/A	N/A
2006/0060770	12/2005	Page et al.	N/A	N/A
2006/0161063	12/2005	Shau	382/128	G06T 7/0012
2007/0092115	12/2006	Usher et al.	N/A	N/A
2007/0116345	12/2006	Peterson et al.	N/A	N/A
2007/0161877	12/2006	Arai et al.	N/A	N/A
2007/0260129	12/2006	Chin	N/A	N/A
2008/0079723	12/2007	Hanson et al.	N/A	N/A
2009/0005693	12/2008	Brauner et al.	N/A	N/A
2009/0018417	12/2008	Wang	N/A	N/A
2009/0093970	12/2008	Lewy et al.	N/A	N/A
2009/0204044	12/2008	Benison	N/A	N/A
2010/0104169	12/2009	Yamada	N/A	N/A
2010/0254582	12/2009	Liu et al.	N/A	N/A
2010/0292629	12/2009	Dacey, Jr. et al.	N/A	N/A

2010/0324407	12/2009	Pichon	600/407	A61B 6/12
2011/0081056	12/2010	Salafia	N/A	N/A
2011/0134426	12/2010	Kaduchak et al.	N/A	N/A
2011/0275908	12/2010	Baumann	N/A	N/A
2011/0299749	12/2010	Rauch	N/A	N/A
2012/0089031	12/2011	Ince	N/A	N/A
2012/0177257	12/2011	Maev et al.	N/A	N/A
2012/0269420	12/2011	Najarian et al.	N/A	N/A
2013/0011055	12/2012	You et al.	N/A	N/A
2013/0216119	12/2012	Baumgart	382/134	A61B 5/150748
2013/0235949	12/2012	Jeckeln	N/A	N/A
2014/0018647	12/2013	Segman	N/A	N/A
2014/0038206	12/2013	Holmes et al.	N/A	N/A
2014/0068513	12/2013	Sakagawa	N/A	N/A
2014/0085482	12/2013	Teich et al.	N/A	N/A
2014/0092377	12/2013	Liu et al.	N/A	N/A
2014/0160481	12/2013	Ahner et al.	N/A	N/A
2014/0232869	12/2013	May et al.	N/A	N/A
2014/0240667	12/2013	Uji et al.	N/A	N/A
2014/0249784	12/2013	Sankaran et al.	N/A	N/A
2014/0273076	12/2013	Adams et al.	N/A	N/A
2015/0141766	12/2014	Fine	600/479	A61B 5/0261
2015/0169641	12/2014	Alldrin et al.	N/A	N/A
2016/0014038	12/2015	Thyagarajan et al.	N/A	N/A
2016/0148038	12/2015	Castro-Gonzalez	600/479	G06T 7/12
2017/0039714	12/2016	Small et al.	N/A	N/A
2017/0138849	12/2016	Tucker-Schwartz et al.	N/A	N/A
2017/0367459	12/2016	Yamasaki	N/A	N/A
2017/0367924	12/2016	Nan	N/A	N/A
2018/0012359	12/2017	Prentasic	N/A	G06V 10/82
2018/0098683	12/2017	Kikuchi	N/A	A61B 1/3132
2018/0211380	12/2017	Tandon	N/A	G06V 20/69
2018/0271382	12/2017	Bezemer	N/A	A61B 5/0013
2019/0228527	12/2018	Ramirez et al.	N/A	N/A
2020/0116698	12/2019	Zelmanovic et al.	N/A	N/A
2020/0237272	12/2019	Lin et al.	N/A	N/A
2021/0374963	12/2020	Gonzalez et al.	N/A	N/A
2022/0113256	12/2021	Verma et al.	N/A	N/A
2022/0192589	12/2021	Butterworth	N/A	N/A
2023/0032932	12/2022	Butterworth et al.	N/A	N/A

#### FOREIGN PATENT DOCUMENTS

Patent No.	Application Date	Country	CPC
1108082	12/1994	CN	N/A
1228014	12/1998	CN	N/A
1342054	12/2001	CN	N/A
1399131	12/2002	CN	N/A
107115099	12/2016	CN	N/A

106803247	12/2020	CN	N/A
0641542	12/1994	EP	N/A
1685794	12/2005	EP	N/A
H07308311	12/1994	JP	N/A
H08206101	12/1995	JP	N/A
2002277747	12/2001	JP	N/A
2007215951	12/2006	JP	N/A
2009063565	12/2008	JP	N/A
2013169296	12/2012	JP	N/A
2012110373	12/2012	JP	N/A
2013545516	12/2012	JP	N/A
2014045868	12/2013	JP	N/A
2014166269	12/2013	JP	N/A
2015515894	12/2014	JP	N/A
2015157071	12/2014	JP	N/A
2016509505	12/2015	JP	N/A
2016086842	12/2015	JP	N/A
2016202442	12/2015	JP	N/A
2017097711	12/2016	JP	N/A
100935455	12/2009	KR	N/A
20130028484	12/2012	KR	N/A
101273692	12/2012	KR	N/A
101452576	12/2013	KR	N/A
0027276	12/1999	WO	N/A
0122741	12/2000	WO	N/A
0207276	12/2001	WO	N/A
2012061078	12/2011	WO	N/A
2013167641	12/2012	WO	N/A
2013173446	12/2012	WO	N/A
2016086023	12/2015	WO	N/A
2017127732	12/2016	WO	N/A
2019079310	12/2018	WO	N/A

## OTHER PUBLICATIONS

U.S. Appl. No. 62/572,738, filed Oct. 16, 2017, Alvaro Sanchez Ferro. cited by applicant

U.S. Appl. No. 62/878,011, filed Jul. 24, 2019, Ian Butterworth. cited by applicant

Allen et al., "Computer based system for acquisition and analysis of nailfold capillary images,"

Medical Image Understanding & Analysis, (2003): 1-4. cited by applicant

Anderson et al., "Computerized nailfold video capillaroscopy—a new tool for assessment of raynaud's phenomenon," J. Rheumatology 32.5 (2005): 841-848. cited by applicant

Bezemer et al. "Validation of near-infrared laser speckle imaging for assessing microvascular (re) perfusion." Microvascular research 79.2 (2010): 139-143. cited by applicant

Bouquard et al. "Analysis of white blood cell dynamics in nailfold capillaries." 2015 37th Annual International Conference of the IEEE Engineering in Medicine and Biology Society (EMBC).

IEEE, 2015, 11 pages. cited by applicant

Bourquard et al., "Non-invasive detection of severe neutropenia in chemotherapy patients by optical imaging of nailfold microcirculation." Scientific reports 8.1 (2018): 1-12. cited by applicant

Brown et al., "Rigidity of Circulating Lymphocytes is Primarily Conferred by Vimentin Intermediate Filaments", The Journal of Immunology, 166.11 (2001): 6640-6646. cited by applicant

Chen "The Research of Measurement and Recognition of the Human Microcirculatory Parameters Based on Image Processor Analysis" Thesis (with abstract), Nanjing Univ. of Aeronautics and Astronautics, 2012, 137 pages. cited by applicant

Chen et al. Deep learning in label-free cell classification. Scientific reports, 6.1 (2016): 21471, 16 pages. cited by applicant

Cheng et al., "Non-invasive assessment of microvascular and endothelial function." JoVE (Journal of Visualized Experiments) 71 (2013): e50008. 8 pages. cited by applicant

Chinese Notice of Allowance and Search Report with English Translation in Chinese Application No. 202080065336.X dated Oct. 19, 2022, 9 pages. cited by applicant

CS&E PCT Collaborative Search and Examination Pilot Upload Peer Contribution mailed Mar. 7, 2019, 58 pages. cited by applicant

Decision of Refusal and English translation dated Jul. 24, 2023 in Japanese App. No. 2020-542060 29 pages. cited by applicant

Decision of Refusal and English translation in Japanese Application No. 2020-542060 dated Nov. 21, 2022, 21 pages. cited by applicant

Delgado-Gonzalo et al., "Spline-based framework for interactive segmentation in biomedical imaging," IRBM 34.3 (2013): 235-243. cited by applicant

Deneux et al., "A processing work-flow for measuring erythrocytes velocity in extended vascular networks from wide field high-resolution optical imaging data." Neuroimage 59.3 (2012): 2569-2588. cited by applicant

Dobbe et al., "Measurement of functional microcirculatory geometry and velocity distributions using automated image analysis." Medical & biological engineering & computing 46.7 (2008): 659-670. cited by applicant

Doshi et al., "Computer-Aided Analysis of Nailfold Capillaroscopy Images." Handbook of Research on Trends in the Diagnosis and Treatment of Chronic Conditions. IGI Global, 2016. 146-158. cited by applicant

Drew et al. "Rapid determination of particle velocity from space-time images using the Radon transform." Journal of computational neuroscience 29.1-2 (2010): 5-11. cited by applicant

Eden et al., "An automated method for analysis of flow characteristics of circulating particles from in vivo video microscopy," IEEE Transactions on Medical Imaging 24.8 (2005): 1011-1024. cited by applicant

Etehad Tavakol, Mahnaz, et al. "Nailfold capillaroscopy in rheumatic diseases: which parameters should be evaluated?." BioMed research international 2015 (2015). cited by applicant

Extended European Search Report dated Apr. 6, 2023, in European Application No. 20843851.5, 14 pages. cited by applicant

Extended European Search Report in European App. No. 23207252.0 dated Jun. 6, 2024, 12 pages. cited by applicant

Extended European Search Report in European Application No. 22172020.4 dated Mar. 20, 2023, 12 pages. cited by applicant

Extended European Search Report in European Patent Application No. 15862463.5 dated Sep. 11, 2018, 7 pages. cited by applicant

Extended European Search Report in European Patent Application No. 18867626.6 dated May 19, 2021, 8 pages. cited by applicant

First Australian Report in Australian App. No. 2023200739 dated Mar. 12, 2024, 5 pages. cited by applicant

First Office Action and Search Report (with translation) in Chinese Application No. 201880076372.9 dated Dec. 5, 2022, 17 pages. cited by applicant

Golan et al., "Noninvasive imaging of flowing blood cells using label-free spectrally encoded flow cytometry," Biomed Opt Express 3.6 (2012): 1455-1464. cited by applicant

Grassi et al., "Capillaroscopy: questions and answers." Clinical rheumatology 26.12 (2007): 2009.

8 pages. cited by applicant

Hofstee et al., "A multicentre study on the reliability of qualitative and quantitative nail-fold videocapillaroscopy assessment," *Rheumatology* (2011): ker403, 749-755. cited by applicant

Hollis et al., "Comparison of venous and capillary differential leukocyte counts using a standard hematology analyzer and a novel microfluidic impedance cytometer," *PloS One* 7.9 (2012): e43702. 8 pages. cited by applicant

Hou et al., "A computerized system of nail-fold capillaroscopy for dry eye disease diagnosis." *Multidimensional Systems and Signal Processing* 23.4 (2012): 515-524. cited by applicant

Howlader et al: "Correlation of severity of chronic venous disease with capillary morphology assessed by capillary microscopy", *Journal of Vascular Surgery*, Elsevier, Amsterdam, NL, vol. 43, No. 3, Mar. 1, 2006 (Mar. 1, 2006), pp. 563-569, XP005314953, ISSN: 0741-5214, DOI: 10.1016/J.JVS.2005.10.077, 7 pages. cited by applicant

Hu et al. Development of Image Analysis System of Nail Fold Microcirculation, *Chinese Journal of Microcirculation*, vol. 5, No. 2, 1995, 6 pages. cited by applicant

Huang et al., "A SR-based radon transform to extract weak lines from noise images," in *Proceedings Int Conf on Image Processing*, Barcelona, Spain 1 (2003): 849-852. cited by applicant

International Search Report and Written Opinion in International Patent Application No. PCT/US18/56100 mailed Mar. 7, 2019, 16 pages. cited by applicant

International Search Report and Written Opinion in International Patent Application No. PCT/US2020/034483 mailed Aug. 4, 2020, 11 pages. cited by applicant

International Search Report and Written Opinion in International Patent Application No. PCT/US2021/034455 mailed Sep. 21, 2021, 11 pages. cited by applicant

International Search Report and Written Opinion issued for PCT/US15/62487, dated Feb. 5, 2016. 13 pages. cited by applicant

Kaur et al., "Nailfold Capillaryscopy Techniques—A Review," *IRACST—IJCSITS* 2.2 (2012): 326-331. cited by applicant

Kim et al., "An original approach for quantification of blood vessels on the whole tumour section." *Analytical cellular pathology* 25.2 (2003): 63-75. cited by applicant

Lefford et al., "Nailfold capillary microscopy in connective tissue disease: a quantitative morphological analysis." *Annals of the rheumatic diseases* 45.9 (1986): 741-749. cited by applicant

MacLennan et al., "Finger-prick blood samples can be used interchangeably with venous samples for CD4 cell counting indicating their potential for use in CD4 rapid tests," *AIDS* 21.12 (2007): 1643-1645. cited by applicant

McKay et al., "Imaging human blood cells in vivo with oblique back-illumination capillaroscopy." *Biomedical Optics Express* 11.5 (2020): 2373-2382. cited by applicant

McKay et al., "Visualization of blood cell contrast in nailfold capillaries with high-speed reverse lens mobile phone microscopy." *Biomedical Optics Express* 11.4 (2020): 2268-2276. cited by applicant

Mengko et al., "Morphological characterization of nailfold capillaries." 2016 International Seminar on Intelligent Technology and Its Applications (ISITIA). IEEE, 2016. 6 pages. cited by applicant

Mercer et al., "Quantitative nailfold video capillaroscopy in patients with idiopathic inflammatory myopathy." *Rheumatology* 49.9 (2010): 1699-1705. cited by applicant

Moeini et al. "Effects of anesthesia on the cerebral capillary blood flow in young and old mice." *Multiphoton Microscopy in the Biomedical Sciences XV*. vol. 9329. International Society for Optics and Photonics, 2015, 7 pages. cited by applicant

Mugii, et al., "Reduced red blood cell velocity in nail-fold capillaries as a sensitive and specific indicator of microcirculation injury in systemic sclerosis," *Rheumatology* 48.6 (2009): 696-703. cited by applicant

Murray et al., "The influence of measurement location on reliability of quantitative nailfold videocapillaroscopy in patients with SSc." *Rheumatology* 51.7 (2012): 1323-1330. cited by

applicant

Decision to Grant in European App. No. 20843851.5 dated Nov. 14, 2024, 2 pages. cited by applicant

Examination Report in European Application No. 22172020.4 dated Dec. 11, 2024, 7 pages. cited by applicant

Australian Office Action (Acceptance) in Australian App. No. 2023200739 dated Sep. 30, 2024, 3 pages. cited by applicant

Decision to Grant with English translation in Japanese Application No. 2020-542060 mailed Sep. 17, 2024, 5 pages. cited by applicant

Notice of Allowance in European App. No. 20843851.5 dated Jul. 3, 2024, 7 pages. cited by applicant

Nagy et al., "Nailfold digital capillaroscopy in 447 patients with connective tissue disease and Raynaud's disease." *Journal of the European Academy of Dermatology and Venereology* 18.1 (2004): 62-68. cited by applicant

Notice of Acceptance in Australian Application No. 2018352526 dated Nov. 18, 2022, 3 pages. cited by applicant

Notice of Allowance in European App. No. 20843851.5 dated Jan. 3, 2024, 8 pages. cited by applicant

Notice of Allowance with translation in Chinese Application No.201880076372.9 dated Apr. 5, 2024, 4 pages. cited by applicant

Office Action in Canadian App. No. 3,079,209 dated Mar. 21, 2024, 4 pages. cited by applicant

Pablo-Trinidad et al., "Automated detection of neutropenia using noninvasive video microscopy of superficial capillaries." *American journal of hematology* 94.8 (2019): E219. 4 pages. cited by applicant

Partial European Search Report in European Application No. 22172020.4 dated Dec. 16, 2022, 14 pages. cited by applicant

PCT International Search and Written Opinion for International App. No. PCT/US2018/056100 dated Mar. 7, 2019, 11 pages. cited by applicant

PCT International Search and Written Opinion for International App. No. PCT/US2020/034483 dated Aug. 4, 2020, 10 pages. cited by applicant

Pennarola et al., "Nailfold capillroscopic monitoring as preventive medicine in subjects exposed to ionising radiation." 11th International Congress of the international Radiation Protection Association. 2004. 6 pages. cited by applicant

Rao et al., "Evaluation of a new point of care automated complete blood count (CBC) analyzer in various clinical settings," *Clinica Chimica Acta* 389.1-2 (2008): 120-125. cited by applicant

Reif et al., "Label-free imaging of blood vessel morphology with capillary resolution using optical microangiography." *Quantitative imaging in medicine and surgery* 2.3 (2012): 207. 6 pages. cited by applicant

Riva et al., "Blue field entoptic phenomenon and blood velocity in the retinal capillaries," *JOSA* 70.10 (1980): 1234-1238. cited by applicant

Russcher et al., "Evaluation of the HemoCue WBC DIFF system for point-of-care counting of total and differential white cells in pediatric samples," *Ned Tijdschr Klin Chem Labgeneesk* 38.3 (2013): 140-141. cited by applicant

Sainthillier et al., "Skin capillary network recognition and analysis by means of neural algorithms." *Skin Research and Technology* 11.1 (2005): 9-16. cited by applicant

Second Office Action (with translation) in Chinese Application No.201880076372.9 dated May 20, 2023, 11 pages. cited by applicant

Shore, "Capillaroscopy and the measurement of capillary pressure." *British journal of clinical pharmacology* 50.6 (2000): 501-513. cited by applicant

Third Office Action (with translation) in Chinese Application No.201880076372.9 dated Jan. 11,



2024, 4 pages. cited by applicant  
Third Office Action with translation in Japanese App. No. 2020-542060 mailed Apr. 1, 2024, 9 pages. cited by applicant  
Uji et al., “The source of moving particles in parafoveal capillaries detected by adaptive optics scanning laser ophthalmoscopy,” Investigative Ophthalmology & Visual Science 53.1 (2012): 171-178. cited by applicant  
USPTO e-Office Action: CTFR—Final Rejection in U.S. Appl. No. 17/666,461 dated Sep. 7, 2023. cited by applicant  
USPTO e-Office Action: CTNF—Non-Final Rejection in U.S. Appl. No. 16/882,966 dated Feb. 19, 2021. cited by applicant  
USPTO e-Office Action: CTNF—Non-Final Rejection in U.S. Appl. No. 14/951,260 dated Sep. 19, 2017. cited by applicant  
USPTO e-Office Action: CTNF—Non-Final Rejection in U.S. Appl. No. 16/162,006 dated May 5, 2021. cited by applicant  
USPTO e-Office Action: CTNF—Non-Final Rejection in U.S. Appl. No. 17/666,461 dated Mar. 15, 2023. cited by applicant  
USPTO e-Office Action: NOA—Notice of Allowance and Fees Due (Ptol-85) in U.S. Appl. No. 16/882,966 dated Jun. 2, 2021. cited by applicant  
USPTO e-Office Action: NOA—Notice of Allowance and Fees Due (Ptol-85) in U.S. Appl. No. 14/951,260 dated Feb. 1, 2018. cited by applicant  
USPTO e-Office Action: NOA—Notice of Allowance and Fees Due in U.S. Appl. No. 16/162,006 dated Sep. 30, 2021. cited by applicant  
Winkelman et al., “Noninvasive Blood Cell Measurements by Imaging of the Microcirculation,” Am J Clin Pathol 113 (2000): 479-483. cited by applicant  
WIPO International Preliminary report on Patentability Chapter 1, Sep. 21, 2021, PCT/US2021/034455 (Year 2021), 9 pages. cited by applicant  
Written Opinion of the International Searching Authority for International App. No. PCT/US2021/034455, mailed Sep. 21, 2021, 8 pages. cited by applicant  
Written Opinion of the International Searching Authority for International Application No. PCT/US2022/039000, dated Oct. 26, 2022, 8 pages. cited by applicant  
Wu, Chih-Chieh, et al. “Accuracy evaluation of RBC velocity measurement in nail-fold capillaries.” Microvascular research 81.3 (2011): 252-260. cited by applicant  
Yap et al., “Mechanical deformation of neutrophils into narrow channels induces pseudopod projection and changes in biomechanical properties”, Journal of Applied Physiology 98.5 (2005): 1930-1939. cited by applicant  
Office Action with Google Translation in Japanese App. No. 2024-200598 dated Jun. 16, 2025, 14 pages. cited by applicant  
European Office Action in European App. No. 23207252.0 dated May 15, 2025, 6 pages. cited by applicant

---

*Primary Examiner:* Nakhjavan; Shervin K

*Attorney, Agent or Firm:* Smith Baluch LLP

---

## **Background/Summary**

CROSS-REFERENCE TO RELATED APPLICATIONS (1) This application is a continuation of, and claims priority to U.S. application Ser. No. 17/666,461, U.S. Pat. No. 11,963,750, filed Feb. 7,

2022, titled “SYSTEMS, DEVICES AND METHODS FOR NON-INVASIVE HEMATOLOGICAL MEASUREMENTS,” which is a continuation of, and claims priority to, U.S. Pat. No. 11,244,452, filed Oct. 16, 2018, titled “SYSTEMS, DEVICES AND METHODS FOR NON-INVASIVE HEMATOLOGICAL MEASUREMENTS,” which claims priority to U.S. Provisional Application No. 62/572,738 filed Oct. 16, 2017, titled “DEVICE AND METHODS FOR NON-INVASIVE HEMATOLOGICAL MEASUREMENTS”, the entire disclosure of which is hereby incorporated by reference.

## TECHNICAL FIELD

(1) The present disclosure relates generally to systems, apparatus, and methods for analyzing blood cell dynamics and cell population dynamics. More specifically, the present disclosure relates to systems, apparatus, and methods for extracting white blood cell information from non-invasive, in vivo, and/or time-lapse images.

## BACKGROUND

(2) White blood cells (WBCs, also referred to as leukocytes or leucocytes) are cells of the immune system that are involved in protecting the body against both infectious disease and foreign invaders. WBCs can exist not only in the blood, but also in the lymphatic system and tissues. Some conditions can trigger a response in the immune system and cause an increase in the number of WBCs (also referred to as WBC count). Other conditions can affect the production of WBCs by the bone marrow or the survival of existing WBCs in the circulation system. Either way, these conditions can cause a change (either an increase or a decrease) of the number of circulating WBCs. Therefore, WBC counts can be a relevant physiological parameter for the diagnosis, monitoring, and treatment of various conditions including, but not limited to, bacterial and viral infections (e.g., pneumonia or meningitis), bone marrow functionality associated with chemotherapy toxicity, and hematologic proliferative processes such as leukemia.

(3) In current clinical practice, most of the tests to derive WBC count are performed with large-scale equipment in central clinical laboratories. Generally, these ex vivo tests are still invasive because blood samples (usually a full vial of blood is needed for each test) are collected from a patient. These blood samples are then transported, queued, and analyzed in laboratory tests, thereby may taking several days to receive any results. This procedure can be burdensome for patients who need regular WBC counts or for patients with emergent conditions as well as their care takers. In addition, due to the ex vivo nature of conventional blood tests, there can be a certain bias of some parameters owing to the inherent differences between the measurements and the true physiological properties.

## SUMMARY

(4) A system includes a platform to receive a body portion of a user during use, and an imaging device coupled to the platform and to acquire a set of images of at least a capillary bed of the body portion. The system also includes a controller communicably coupled to the imaging device and to detect, in each image of the set of images, one or more capillaries in the body portion to identify a first set of capillaries across the set of images. The detecting including estimating one or more attributes of each capillary of the first set of capillaries, the one or more attributes including one or more structural attributes, one or more flow attributes, one or more imaging attributes, or combinations thereof. A first attribute of the one or more attributes of each capillary of the first set of capillaries meets a predetermined criterion for the first attribute. The controller also identifies a second set of capillaries from the first set of capillaries such that each capillary of the second set of capillaries is visible in a predetermined number of images of the set of images.

(5) A method including acquiring a set of images of at least a capillary bed of a body portion of a user, and detecting, in each image of the set of images, one or more capillaries in the body portion to identify a first set of capillaries across the set of images. The detecting includes estimating one or more attributes of each capillary of the first set of capillaries, the one or more attributes

including one or more structural attributes, one or more flow attributes, one or more imaging attributes, or combinations thereof. A first attribute of the one or more attributes of each capillary of the first set of capillaries meets a predetermined criterion for the first attribute. The method also includes identifying a second set of capillaries from the first set of capillaries such that each capillary of the second set of capillaries is visible in a predetermined number of images of the set of images.

(6) A device including a controller to receive a set of images of a capillary bed of a body portion of a user, and to detect, in each image of the set of images, one or more capillaries in the body portion of the finger to identify a first set of capillaries across the set of images. The detecting includes estimating one or more attributes of each capillary of the first set of capillaries, the one or more attributes including one or more structural attributes, one or more flow attributes, one or more imaging attributes, or combinations thereof. A first attribute of the one or more attributes of each capillary of the first set of capillaries meets a predetermined criterion for the first attribute. The controller also identifies a second set of capillaries from the first set of capillaries such that each capillary of the second set of capillaries is visible in a predetermined number of images of the set of images. The controller also detects, for the set of images and in the second set of capillaries, a set of cellular events, each cellular event of the set of cellular events associated with passage of a white blood cell in a capillary of the second set of capillaries. The controller also estimates an event count for the second set of capillaries based on the set of cellular events.

(7) It should be appreciated that all combinations of the foregoing concepts and additional concepts discussed in greater detail below (provided such concepts are not mutually inconsistent) are contemplated as being part of the inventive subject matter disclosed herein. In particular, all combinations of claimed subject matter appearing at the end of this disclosure are contemplated as being part of the inventive subject matter disclosed herein. It should also be appreciated that terminology explicitly employed herein that also may appear in any disclosure incorporated by reference should be accorded a meaning most consistent with the particular concepts disclosed herein.

---

## Description

### BRIEF DESCRIPTION OF THE DRAWINGS

(1) The patent or application file contains at least one drawing executed in color. Copies of this patent or patent application publication with color drawing(s) will be provided by the Office upon request and payment of the necessary fee.

(2) The skilled artisan will understand that the drawings primarily are for illustrative purposes and are not intended to limit the scope of the inventive subject matter described herein. The drawings are not necessarily to scale; in some instances, various aspects of the inventive subject matter disclosed herein may be shown exaggerated or enlarged in the drawings to facilitate an understanding of different features. In the drawings, like reference characters generally refer to like features (e.g., functionally similar and/or structurally similar elements).

(3) FIG. 1 is a flow chart illustrating methods of analyzing blood cell dynamics in accordance with some embodiments.

(4) FIG. 2 is a flow chart illustrating methods of analyzing blood cell dynamics using spatiotemporal profiles and Radon transform in accordance with some embodiments.

(5) FIG. 3 is an example image of a nailfold that can be used in the methods illustrated in FIGS. 1-2 in accordance with some embodiments.

(6) FIGS. 4A-4B are plots of cubic spline interpolation that can be used in the methods illustrated in FIGS. 1-2 for resampling user-specified contour points of capillaries in accordance with some embodiments. FIG. 4A is a plot of a cubic spline interpolation of x-coordinates. FIG. 4B is a plot of

a cubic spline interpolation of y-coordinates.

(7) FIG. 5 is an image of a nailfold including two capillaries, user-specified contour points, and resampled contour curves in accordance with some embodiments.

(8) FIGS. 6A-6B are representations of spatiotemporal profiles extracted from the two capillaries shown in FIG. 5 in accordance with some embodiments. FIG. 6A shows an example spatiotemporal profile  $g''$  of capillary 500 from FIG. 5. FIG. 6B illustrates spatiotemporal trajectories corresponding to WBC events by dashed lines spanning the 2D intensity plot.

(9) FIG. 7 is a representation of a Radon transform performed on a spatiotemporal profile in accordance with some embodiments.

(10) FIGS. 8A-8B are representations of spatiotemporal profiles in the Radon domain with local maxima highlighted to indicate WBC events in accordance with some embodiments. FIG. 8A shows the Radon transform  $\hat{g}$  of the map in FIG. 7, according to some embodiments. FIG. 8B shows the spatiotemporal profile in the Radon domain with identified peaks highlighted in circles.

(11) FIGS. 9A-9B are plots representing experimental results of WBC events occurring inside the two capillaries shown in FIG. 5 in accordance with some embodiments. FIG. 9A shows experimental results of WBC events occurring inside capillary 500. FIG. 9B shows experimental results of WBC events occurring inside capillary 510 shown in FIG. 5.

(12) FIG. 10 is a plot comparing WBC events obtained from methods illustrated in FIG. 2 in accordance with some embodiments and WBC events identified by trained human reviewers.

(13) FIGS. 11A-11C are schematics of systems for analyzing blood cell dynamics using a finger holder and an imager in accordance with some embodiments. FIG. 11A is a side view of the system, and FIG. 11B is a top view of the system, according to some embodiments. FIG. 11C is a system for analyzing blood cell dynamics, according to other embodiments.

(14) FIGS. 12A-12B are schematics of systems for analyzing blood cell dynamics using an imager in vertical configuration in accordance with some embodiments. FIG. 12A is a side view of the system. FIG. 12B is a top view of the system.

(15) FIG. 13 is a schematic of a system for analyzing blood cell dynamics analysis using a smartphone in accordance with some embodiments.

(16) FIGS. 14A-14D are images of systems and apparatus for analyzing blood cell dynamics analysis in accordance with some embodiments. FIG. 14A shows a finger holder coupled to an imager. FIG. 14B shows an imager and a finger holder de-coupled. FIG. 14C shows a finger holder when a finger is placed in the finger hole. FIG. 14D shows a system including a finger holder, an imager, and a computer that is connected to the imager.

(17) FIGS. 15A-15J are views of an adapter for capturing images of a nailfold with a smartphone camera for blood cell dynamics analysis in accordance with some embodiments. FIG. 15A is a perspective view of the adapter. FIG. 15B is another perspective view of the adapter to illustrate the structure of a window section. FIG. 15C is a top view of the adapter. FIG. 15D is a side view of the adapter. FIG. 15E is another side view of the adapter. FIG. 15F is a back view of the adapter. FIG. 15G is a front view (the side receiving the finger) of the adapter. FIG. 15H is a perspective view of the adapter illustrating an illumination channel. FIG. 15I is a perspective cross-sectional view of part of the adapter to illustrate a window and an illumination channel. FIG. 15J is a cross-sectional view of the adapter to illustrate a structure of an illumination channel.

(18) FIG. 16 is a schematic of a system including a smartphone and an adapter for capturing images of a nailfold for blood cell dynamics analysis in accordance with some embodiments.

(19) FIGS. 17A-17B are images of a system including a smartphone and an adapter for capturing images of a nailfold for blood cell dynamics analysis in accordance with some embodiments. FIG. 17A shows a smartphone with an adapter attached to the smartphone so as to allow image taking of a nailfold according to some embodiments. FIG. 17B shows the smartphone and the adapter when a finger is placed in front of the adapter for imaging.

(20) FIG. 18 is an example image captured by the system shown in FIGS. 17A-17B in accordance

with some embodiments.



(21) FIG. 19 is a schematic of a clamp device for performing blood cell dynamics analysis from images of a nailfold in accordance with some embodiments.

(22) FIG. 20 is an image of a clamp device being used to capture images of a nailfold and analyzing blood cell dynamics.

(23) FIGS. 21A-21F and 21G-21O are images and wireframes, respectively, of a smartphone adapter for capturing images of a nailfold with a smartphone camera for capillaroscopy and hematology analysis in accordance with some embodiments. FIG. 21A is a first view of an adapter for capturing images of a nailfold with a smartphone camera. FIG. 21B is another view of the adapter attached to a smartphone. FIG. 21C is yet another view of the adapter to a smartphone. FIG. 21D is yet another view of the adapter to a smartphone. FIG. 21E is yet another view of the adapter to a smartphone. FIG. 21F is yet another view of the adapter, shown here unattached. FIG. 21G is a wireframe view of the adapter. FIG. 21H is another wireframe view of the adapter. FIG. 21I is yet another wireframe view of the adapter. FIG. 21J is another wireframe view of the adapter. FIG. 21K is another wireframe view of the adapter. FIG. 21L is another wireframe view of the adapter. FIG. 21M is another wireframe view of the adapter. FIG. 21N is another wireframe view of the adapter. FIG. 21O is another wireframe view of the adapter.

(24) FIGS. 22A-22D are images illustrating a method of using a smartphone adapter for capturing images of a nailfold with a smartphone camera for capillaroscopy and hematology analysis in accordance with some embodiments. In FIG. 22A, shows index matched fluid disposed on the surface of a nail fold of a user. FIG. 22B is a view of the smartphone positioned over the finger. FIG. 22C is another view of the smartphone positioned over the finger. FIG. 22D is yet another view of the smartphone positioned over the finger.

(25) FIG. 23 illustrates a system for non-invasive hematological measurements, according to embodiments.

(26) FIGS. 24A-24B illustrates Capillary tracking criteria to select suitable capillaries. Each capillary was tracked with a given identifier (id) during 3600 frames of a video. FIG. 24A illustrates capillary tracking criteria, with the black bars=capillary segments used to compute the cell count/Leuko index. The id is selected if the amounts of appearances is more than confidence value custom character=600, (green cases) or discarded if there is more than 3 capillaries selected (red cases). In cases with less than 3 capillaries, the value of custom character=1. FIG. 24B illustrates capillary tracking criteria, with the capillary segments used to compute the leuko index shown in green and red otherwise.

(27) FIG. 25 illustrates capillary detection in a raw video using the neural network-based method/approach described herein, and comparison with human-expert-based performance. Results from the union between two raters (green) vs. results from neural network analysis (red; yellow if overlap).

(28) FIGS. 26A-26C illustrate an averaged time signal. FIG. 26A illustrates an example of a real averaged time signal produced from one of the analysed capillary videos, shown for its 20 first seconds (Frames 1-1200; see left), with positive-valued peaks associated with the detected events, with a two-second zoom around a single event (Frames 650-769; see right). The zoomed time signal around this example event displays a brightness peak, and also a slight 'dip' of some duration subsequently. FIG. 26B illustrates the expected profile of the averaged time signal around the passage of a single event, this event being associated with the passage of a white blood cell in the capillary (see right). In accordance with the zoomed example of (a), an intensity "dip" is supposed to always occur right after the intensity-peak maximum, due to higher accumulation of red blood cells upstream the white blood cell. FIG. 26C illustrates the expected profile of the averaged time signal around the passage of a plasma gap in the capillary (see right); no dip is supposed to occur in this case as there is no white blood cell and thus no accumulation of red blood cells upstream.

(29) FIGS. 27A-27B illustrate cellular event detection by automated approach vs manual raters. FIG. 27A illustrates an example of event detected on a capillary video by one of the human raters (top row) vs. the neural network (bottom row) with event marks in blue and white, respectively. FIG. 27B illustrates how true positives (TP), false positives (FP), and false negatives (FN) were evaluated for event detection with respect to a reference. On the right, average F1 score obtained for the 3 raters (red) and for the algorithm (blue) across the 26 capillary videos analyzed, displaying a comparable performance of the neural network according to that metric (F1 isocurves shown in black dashed lines). The expected behavior of the neural network if tuning the event-detection threshold is shown in red dashed line.

(30) FIGS. 28A-28D illustrate an example event detection method/approach. FIG. 28A illustrates an initial capillary video with selected frames showing a plasma gap flowing through the capillary, with the direction of flow emphasized by the arrow. FIG. 28B illustrates a pre-processed video with the event appearing as the salient feature in an otherwise dark background. The reference pixel Pref is shown in red, and additional pixels P1 and P2 belonging to the capillary are shown in blue. FIG. 28C illustrates a brightness time signal at the reference-pixel location, at P1, and at P2, revealing the effect of the event (green highlight) on the measured brightness as peaks. FIG. 28D illustrates a final time signal obtained as the average between time signals at individual pixel locations, following their alignment with the reference time signal of Pref; the threshold level used for counting is shown as a vertical blue line.

(31) FIGS. 29A-29B illustrate classification results generated by the full automated approach as disclosed herein on 116 data points. FIG. 29A illustrates a box plot showing the classification of raw videos associated with baseline states, or  $ANC > 500$  (blue) vs. raw videos associated with severe-neutropenic states ( $ANC < 500$ ). FIG. 29B illustrates a ROC curve associated with the classification ( $AUC = 0.96$ ).

(32) FIG. 30 is a flowchart of a method for non-invasive hematological measurements, according to some embodiments.

(33) FIGS. 31A-31F illustrate a method of estimating blood volume based on analysis of pixel-intensity values. FIG. 31A shows an image of a capillary section. FIG. 31B shows another image of the capillary sections, where the pixel value in FIG. 31A is greater than the pixel value in FIG. 31B (i.e. FIG. 31A is brighter). FIG. 31C is a reconstructed capillary cross section of the capillary section in FIG. 31A. FIG. 31D is a reconstructed capillary cross section of the capillary section in FIG. 31B. FIG. 31E shows a reconstructed capillary cross section of the capillary section in FIG. 31A, using the method based on pixel intensity analysis. FIG. 31F shows a reconstructed capillary cross section of the capillary section in FIG. 31B, using the method based on pixel intensity analysis.

(34) FIGS. 32A-32C illustrate a method of volume resampling of a capillary profile. FIG. 32A is a representation of a capillary having a constant blood flow speed but varying diameters along the capillary length. FIG. 32B illustrates a spatio-temporal map representing the gray-scale values (color map from blue—dark—to red—bright—) along the linear capillary length (y-axis) across time (x-axis). FIG. 32C illustrates a spatio-temporal map acquired using volume resampling and the map is shown with the capillary length coordinates (y-axis) as a function of the cumulative capillary volume at each cross-section in FIG. 32A.

(35) FIG. 33 illustrate sub-selection of capillaries based on observed size.

(36) FIGS. 34A and 34B illustrate sub-selection of capillaries based on the distribution of time of arrival between observed gaps. FIG. 34A shows the distribution of the time of arrival (TOA) between gaps in a sample with 5,500 WBC/ $\mu$ L. FIG. 34B shows the distribution of TOA between gaps in a sample with 100 WBC/ $\mu$ L.

(37) FIGS. 35A-35C illustrate an apparatus for detecting severe neutropenia based on images of nailfold capillaries. FIG. 35A illustrates a rendered 3D model of the apparatus employed to record microscopy videos of the microcirculation in nailfold capillaries of patients. FIG. 35B illustrates

that patients place their ring finger in a 3D-printed holder. FIG. 35C shows that the finger is placed in such a way that illumination and imaging is directed at the nailfold area.

(38) FIG. 36 illustrates two different timing points to acquire images from patients in a clinical study using the apparatus shown in FIG. 35A.

(39) FIGS. 37A and 37B show examples of raw images acquired by the apparatus shown in FIG. 35A. FIG. 37A shows an image taken with baseline neutrophil concentration (i.e., greater than  $1,500/\mu\text{L}$ ). FIG. 37B shows an image taken with when the patient had severe neutropenia (neutrophils concentration less than  $500/\mu\text{L}$ ).

(40) FIGS. 38A-38E illustrate an example of optical gap flowing in a capillary. FIG. 38A illustrates the optical gap in a first location in a capillary. FIG. 38B illustrates the optical gap in another location in the capillary. FIG. 38C illustrates the optical gap in yet another location in the capillary. FIG. 38D illustrates the optical gap in yet another location in the capillary. FIG. 38E illustrates the optical gap in yet another location in the capillary.

(41) FIGS. 39A-39E show results of blind event rating using the images acquired by the apparatus shown in FIG. 35A. FIG. 39A shows a capillary-video frame (indexed at top right) with cross-shaped event marks from rater 1 (blue), 2 (green) and 3 (yellow). FIG. 39B shows another capillary-video frame. FIG. 39C shows yet another capillary-video frame. FIG. 39D shows aggregated positions of all event marks from all three raters. FIG. 39E shows an ST map displaying the recorded brightness levels along the segmented capillary length (vertical axis) as a function of time (horizontal axis) for a 1.7-second interval around the event of interest.

(42) FIG. 40 shows the number of validated events per minute in all studied capillary pairs.

(43) FIG. 41 shows the discrimination between baseline and severe neutropenia observed in the clinical study.

(44) FIG. 42 illustrates a pre-processing workflow in the clinical study to process images acquired by the apparatus shown in FIG. 35A.

(45) FIG. 43 shows the number of events labeled by one single rater in the clinical study.

(46) FIGS. 44A and 44B show discrimination between baseline and severe neutropenia using capillary aggregates. FIG. 44A shows the number of event counts resulting from integrating  $N=1, 2, 3, 4, 5$  capillaries per patient. FIG. 44B shows the ROC curves for classification of baseline vs. severe neutropenia based on integrating  $N=1, 2, 3, 4, 5$  capillaries per patient.

(47) FIGS. 45A-45C show examples of a capillary segmentation. FIG. 45A shows capillary from a patient. FIG. 45B shows the same capillary with supervised segmentation (red). The scale bar is  $20\ \mu\text{m}$ . FIG. 45C shows the separations between arterial limb (green), venous limb (blue), and loop (red) of the capillary can be defined on a case-to-case basis for visualization.

(48) FIG. 46 shows the expected amount of events per capillary minute under shot noise.

(49) FIG. 47 shows the distribution of capillary diameters at event positions.

(50) FIGS. 48A and 48B show ST maps of capillaries with high versus low ratio ratios of validated events. FIG. 48A shows a ST map for a baseline patient. FIG. 48B shows a ST map for a patient with severe neutropenia.

(51) FIG. 49 shows capillary selection from both experts in raw-video pair for Patient 01, Region 1.

(52) FIG. 50 shows capillary selection from both experts in raw-video pair for Patient 01, Region 2.

(53) FIG. 51 shows capillary selection from both experts in raw-video pair for Patient 02, Region 1.

(54) FIG. 52 shows capillary selection from both experts in raw-video pair for Patient 02, Region 2.

(55) FIG. 53 shows capillary selection from both experts in raw-video pair for Patient 03.

(56) FIG. 54 shows capillary selection from both experts in raw-video pair for Patient 04.

(57) FIG. 55 shows capillary selection from both experts in raw-video pair for Patient 05.

(58) FIG. 56 shows capillary selection from both experts in raw-video pair for Patient 06.

(59) FIG. 57 shows capillary-selection from both experts in raw-video pair for Patient 07.

(60) FIG. 58 shows capillary-selection from both experts in raw-video pair for Patient 08.

(61) FIG. 59 shows capillary-selection from both experts in raw-video pair for Patient 09.

(62) FIG. 60 shows capillary-selection from both experts in raw-video pair for Patient 10.

(63) FIGS. 61A-61B illustrate classification results for video segments of a specific duration. FIG. 61A illustrates classification area-under-the-curve (AUC) as a function of video segment duration[s], with video segment(s) beginning at the very start of the full video. The classification performance is seen to remain optimal and equal to the one based on full 1-min videos for durations of at least 29 seconds, i.e., approximately half the original 1-minute duration. FIG. 61B illustrates classification AUC when using different 29-second video segments when varying the starting time of each video segment in the full 1-minute video; the near-constancy of the resulting AUC values demonstrates the stability of the classification results.

#### DETAILED DESCRIPTION

(64) Following below are more detailed descriptions of various concepts related to, and implementations of, systems, devices and methods for non-invasive hematological measurements. It should be appreciated that various concepts introduced above and discussed in greater detail below may be implemented in numerous ways. Examples of specific implementations and applications are provided primarily for illustrative purposes to enable those skilled in the art to practice the implementations and alternatives apparent to those skilled in the art.

(65) The figures and example implementations described below are not meant to limit the scope of the present implementations to a single embodiment. Other implementations are possible by way of interchange of some or all of the described or illustrated elements. Moreover, where certain elements of the disclosed example implementations may be partially or fully implemented using known components, in some instances only those portions of such known components that are necessary for an understanding of the present implementations are described, and detailed descriptions of other portions of such known components are omitted so as not to obscure the present implementations.

(66) In view of the challenges with conventional blood tests as discussed above, the Inventors have recognized and appreciated various advantages of non-invasive and in vivo techniques to derive WBC counts. These non-invasive and in vivo techniques allow more frequent monitoring, fewer visits to clinics, and more ready access to testing in areas lacking proper laboratory facilities or reagent supplies.

(67) Non-invasive WBC count techniques that exploit the optical properties of WBCs may be used to observe the WBCs as gaps in nailfold capillaries, retinal capillaries, or moving particles in oral mucosa capillaries. However, specialized and/or non-portable devices (e.g., adaptive optics and confocal microscopy) may be required to derive WBC counts. Optical devices referred to as capillaroscopes may be used to acquire optical images of the morphology of nailfold capillaries and diagnose rheumatological diseases; however, the acquired images require time-consuming analysis by trained human reviewers.

(68) Overview of Non-Invasive and In Vivo Analysis of Blood Cell Dynamics

(69) FIG. 1 is a flow chart illustrating non-invasive and in vivo methods of analyzing blood cell dynamics according to some embodiments, including but not limited to, detecting a number of WBCs passing through a given capillary over a time period, the speed of one or more of the WBCs flowing through the capillary, and the total number of WBC events per  $\mu\text{L}$ . In some embodiment, some or all aspects of the method 100 can be implemented by one or more of the systems, apparatuses, and devices as described herein such as, for example, the system 2300 and/or the device 2340, as described in greater detail with respect to FIG. 23.

(70) More specifically, method 100 illustrated in FIG. 1 includes step 110, at which source image(s) of a subject that contains capillaries are normalized and/or registered. Normalization (also referred to as contrast stretching, histogram stretching, or dynamic range expansion) of source images may change the range of pixel intensity values so as to, for example, increase the contrast of images. Registration of source images may align the source images such that same pixel locations on different images correspond to same physical locations on the subject. In some embodiments,



the source images are taken within a finite time span, during which the camera, the subject, or both, may be moving. Image registration may address such movements. In image registration, one of the images (e.g., the first image in the sequence, the last image in the sequence, or the image that might have the desired field of view) may be used as a reference image, and the other images in the sequence may be compared to the reference image to make corrections. Corrections may be made to maximize certain image similarity measures that quantify the similarity between the reference image and the other images. Examples of image similarity measures include, for example, cross-correlation, mutual information, sum of squared intensity differences, and ratio image uniformity.

(71) At step **120** of method **100**, capillary segmentation and/or profile extraction are performed. Capillary segmentation may be used to identify the segments of capillaries in either the original or the registered images (e.g., by identifying the boundaries of the capillary segments). Profile extraction may be used to extract pixel information within the capillary segments for further analysis. Since WBC information is normally contained only in capillaries, it may be helpful to extract pixel information inside the capillary segments and set aside information in other areas in the images. The pixel information to be extracted may include the locations and values (also referred to as intensities) of the pixels inside the capillary segments. The locations of the pixels in each image may be represented in 2D Cartesian coordinates, and the capillaries may be curved. Therefore, it may be helpful to transform the image from the 2D Cartesian coordinate system into a different coordinate system, in which the same points in the same capillary but on different images in the sequence of images have the same coordinates. One example of such a coordinate system is the curvilinear coordinate system, which uses one point in the curved capillary as the origin point and any other point has a one-dimensional (1D) coordinate that is the distance between that point and the origin point.

(72) At step **130** of method **100**, profiles extracted from the sequence of images are compiled into a single image (also referred to as spatiotemporal profile) so as to analyze WBC events. Profiles extracted from each image may include information about spatial distribution (i.e., locations) of WBC events or other events of interest. Profiles extracted from different images, taken at different time points, in the sequence of images may include information about WBC events at different time points. Therefore, the spatiotemporal profile, compiled from all of these extracted profiles from the entire sequence of images, may provide rich information relating to both spatial distribution and temporal evolution of WBC events. For example, traces of a particular WBC may be visualized from the spatiotemporal profile. The velocity of a particular WBC flowing in a capillary also may be derived by, for example, taking into account the time lapse between two or more images in the sequence of images.

(73) At step **140** of method **100**, the spatiotemporal profile is processed to detect and/or analyze WBC events. In some embodiments, the processing is manual. A user may inspect the spatiotemporal profile and identify a WBC event by, for example, detecting a visual gap (e.g., pixels having higher or lower pixel values compared to surrounding pixels) in the spatiotemporal profile. The user also may derive the motion traces and flow speed from the spatiotemporal profile. In other embodiments, the processing is automatic or semi-automatic. For example, the spatiotemporal profile may be, for example, transformed to the Radon domain. WBC events then may be detected based on local maxima in the Radon domain. Based on the detected WBC events, additional analysis, such as WBC counts and WBC flow speed, may be derived. Furthermore, WBC counts, flow speed, etc., may be used for subsequent diagnosis, monitoring, and/or treatment of diseases or conditions.

(74) According to some embodiments, systems, apparatus, and methods for analysis of blood cell dynamics are based on in vivo images of capillaries without blood drawing or other invasions into a subject's body and also without removing WBCs from their natural environment in the subject's body. In addition, these systems, apparatus, and methods may be used for real-time or substantially real-time results. For example, the processing of the images (from source images to the detection of

WBC events and calculation of the WBC counts) may be performed while new images are being taken. WBC events may be monitored to test the response of a subject's body to a medical treatment, thereby providing feedback regarding the efficiency of the treatment. Furthermore, systems, apparatus, and methods here can identify WBC events from relatively low-resolution, low-frame-rate, and noisy source images. For examples, the source images can be frames of a video clip taken by off-the-shelf cameras, cellphone, or other image taking devices.

(75) Methods of Non-Invasive and In Vivo Analysis of Blood Cell Dynamics

(76) FIG. 2 is a flow chart illustrating methods of analyzing blood cell dynamics using Radon transforms of spatiotemporal profiles of capillary images according to some embodiments. Method **200** may be used to detect a WBC event from in vivo capillary data associated with a subject. In some embodiment, some or all aspects of the method **200** can be implemented by one or more of the systems, apparatuses, and devices as described herein such as, for example, the system **2300** and/or the device **2340**, as described in greater detail with respect to FIG. 23.

(77) At step **210** of method **200**, capillary data is non-invasively obtained. The capillary data may include a plurality of images of one or more capillary segments captured over a first time period.

(78) At step **220** of method **200**, the contours of the one or more capillary segments in the images are specified. In particular, for each image in the plurality of images, a first set of two-dimensional (2D) coordinates may be specified to correspond to internal contour points of a capillary segment visible in the images. Step **220** also may include specifying a second set of 2D coordinates corresponding to external contour points of the capillary segment. These sets of 2D coordinates in each image may define the boundaries of the capillary segment in the image.

(79) At step **230** of method **200**, each of the first set of 2D coordinates and the second set of 2D coordinates are interpolated so as to generate a first set of resampled coordinates and a second set of resampled coordinates, respectively. The interpolation may fill potential gaps between adjacent contour points specified at step **220** and therefore define smoother boundaries of the one or more capillary segments.

(80) At step **240** of method **200**, a plurality of intermediate curves are generated based on the first set of resampled coordinates and the second set of resampled coordinates. These intermediate curves may be within the capillary segment defined by the internal contours points and the external contour points. The plurality of intermediate curves may include a middle curve, which may be used to define a plurality of curvilinear distances as in step **250** of method **200**.

(81) In step **260** of method **200**, a plurality of intensity values are extracted from the plurality of images. Each extracted intensity value corresponds to one of the plurality of images, one of the plurality of intermediate curves, and one of the plurality of curvilinear distances. That is, each extracted intensity value may be indexed by a vector including three values representing (1) a particular image, (2) a particular intermediate curve, and (3) a particular curvilinear distance.

(82) At step **270** of method **200**, the extracted intensity values are transformed to the Radon domain. In step **280** of method **200**, a plurality of maxima locations in the Radon domain correspond to a flow trajectory inside the capillary such that a visual gap in the flow trajectory inside the capillary indicates a WBC event.

(83) Capillary Data Collection

(84) According to some embodiments, capillary data (e.g., source images) for the analysis of blood cell dynamics may be obtained from various subjects including, but not limited to, humans and other mammals. In some embodiments, capillary data is collected or captured from one or more locations on or in the body of the subject. For example, capillary data may be collected and/or captured from nailfold capillaries, retinal capillaries, and/or oral mucosa capillaries.

(85) Source images may be captured using various methods. For example, source images may include a sequence of images extracted from a video clip. Each image in the sequence of the images may be captured at a different time point such that the analysis of blood cell dynamics may include, for example, the flow speed of WBCs.

(86) In some embodiments, a location on or in the body of the subject is illuminated by pulsed light sources, and source images are captured by a camera synchronized with the pulsed light sources. For example, a location may be illuminated by pulsed lasers of a particular wavelength (e.g., blue light at about 430 nm), at which WBCs (or other objects of interest) have good reflectivity, so as to improve the contrast of the resulting images.

(87) In some embodiments, the source images include one or more color images such that each pixel in the source images include three values corresponding to, for example, the values of the red, green, and blue components, respectively. In some embodiments, the source images include one or more gray-scale images such that each pixel in the source images has a bit depth of, for example, 2, 4, 6, 7, 8, or 10, corresponding to a gray level of 4, 16, 64, 128, 256, and 1024, respectively.

(88) In some embodiments, the capillary data (e.g., obtained at step **210** in FIG. **2**) includes a video acquired in 24-bit RGB format from a given subject. In general, video data may be viewed as a three-dimensional stack  $I$  of a sequence of image frames represented as  $N_{\text{sub.h}} \times N_{\text{sub.v}} \times N_{\text{sub.f}}$ , where  $N_{\text{sub.h}}$  and  $N_{\text{sub.v}}$  are the horizontal and vertical sizes (also referred to as pixel numbers) of each image frame, respectively, and  $N_{\text{sub.f}}$  is the total number of frames in the video data. Each pixel in this video data may be represented as  $I[k, l]$ , which corresponds to an RGB vector  $(R[k; 1], G[k; 1], B[k; 1])$ . The indices  $k=(k_{\text{sub.1}}, k_{\text{sub.2}})$  designate the location of a pixel within a certain frame, and  $l$  refers to the index of the frame in the plurality of frames included in the video data.  $R[k; 1]$ ,  $G[k; 1]$ , and  $B[k; 1]$  corresponds to the value of red, green, and blue component, respectively, of the pixel  $I[k, l]$ . For example,  $I[(15, 20), 5]$  points to a pixel located at the fifteenth row and the twentieth column in the fifth frame of the video data.

(89) FIG. **3** is an example image of a human nailfold that may be used in the methods described above for the analysis of blood cell dynamics in one or more of the nailfold capillaries. The image is a frame taken from a nailfold capillaroscopy video, which has a frame rate of  $r$  frames per second and a camera pixel size of  $S_{\text{sub.p}}$   $\mu\text{m}$ . In FIG. **3**, the relatively darker U-shaped profiles of capillaries **300** are readily identifiable in the image, despite the presence of white saturated areas **310** associated with non-ideal acquisition conditions.

#### (90) Capillary Data Preprocessing

(91) Some pre-processing steps of the images in the capillary data may be performed to facilitate subsequent processing and analysis. These pre-processing steps may include image normalization and/or image registration. In some embodiment, some or all aspects of these pre-processing steps can be implemented by one or more of the systems, apparatuses, and devices as described herein such as, for example, the system **2300** and/or the device **2340**, as described in greater detail with respect to FIG. **23**.

(92) In some embodiments, the capillary data includes one or more grayscale images. Normalization may be used to compress and/or stretch the gray level to a desired range. In some embodiments, the capillary data includes one or more color images. Normalization may be used to convert a color image into a grayscale image before compressing and/or stretching the gray level. The conversion from color images to grayscale images may be achieved via various methods. In one example, the resulting gray level of a color pixel is a sum of the red, green, and blue values in the pixel. In another example, the resulting gray level is the difference between the value of the red component and green component ( $R-G$ ) so as to emphasize the capillary structures. More sophisticated methods may be employed to calculate the gray level so as to emphasize specific objects of interest (e.g., a WBC or a red blood cell). For example, particular weighted averages of red, green, and blue components may be calculated, or in other types of channel conversion that are non-linear (e.g., RGB to HSV (Hue, Saturation, Value) conversion).

(93) In some embodiments, image registration includes one or more intensity-based methods, which compare intensity patterns in images via correlation metrics. Intensity-based methods can register entire images or sub-images. If sub-images are registered, centers of corresponding sub-images may be treated as corresponding feature points.

(94) In some embodiments, image registration includes one or more feature-based methods, which find correspondence between image features such as points, lines, and contours. Feature-based methods can establish a correspondence between one or more distinct points in an image. Knowing the correspondence between these distinct points in images, a geometrical transformation may be determined to map the target image to other images, thereby establishing point-by-point correspondence between a reference image and other images.

(95) In some embodiments, the capillary data includes a 24-bit RGB format video, including frames like the image in FIG. 3. In these embodiments, stack I may be converted into a single-channel version  $I_{\text{sub}.n}$  that can be suitably exploited for further profile segmentation and analysis. The scalar-valued stack  $I_{\text{sub}.n}[k; l]$  may be obtained by first averaging the RGB channels of I for each pixel point (“point-wise”) and then normalizing the resulting intensities. The normalization may be performed such that the mean and standard deviation of the intensity values of  $I_{\text{sub}.n}$  over every given frame  $l$  is 0 and 1, respectively. The frames constituting  $I_{\text{sub}.n}$  may be registered to, for example, compensate for camera movements. The frame registration may be achieved by applying respective corrective shifts to each frame  $l > 1$  of  $I_{\text{sub}.n}$  that is, using the first image ( $l=1$ ) as reference.

(96) More specifically and first, a point-wise operation may be performed to obtain temporary stack

$$(97) \quad I'[k; l] = R[k; l] - G[k; l], \quad (1)$$

for all  $k$  and  $l$ , i.e.,  $k_{\text{sub}.1}=1, 2, \dots, N_{\text{sub}.h}$ ;  $k_{\text{sub}.2}=1, 2, \dots, N_{\text{sub}.v}$ ; and  $k_{\text{sub}.3}=1, 2, \dots, N_{\text{sub}.f}$ . This operation emphasizes capillary-like structures while discarding surrounding artefacts.

(98) Second, binary-thresholded stack  $I_{\text{sub}.t'}$  may be obtained using a threshold value  $\tau_{\text{sub}.c}$  that is specified for every separate frame of the sequence, the value of which may be determined either experimentally, using a priori information existing in the images (e.g., total brightness, contrast, grayscale variance, skewness, etc.), or through feature learning from a training dataset. In this step, the pixel value at a location  $[k; l]$  in the temporary stack  $I'[k; l]$  is set to zero if  $I'[k; l]$  is smaller than  $\tau_{\text{sub}.c}$  and is set to one if  $I'[k; l]$  is equal to or greater than  $\tau_{\text{sub}.c}$ , that is:

$$(99) \quad I_t[k; l] = 0 \text{ if } I'[k; l] < \tau_{\text{sub}.c} \quad (2) \text{ and } I_t[k; l] = 1 \text{ if } I'[k; l] \geq \tau_{\text{sub}.c} \quad (3)$$

(100) Third, a 2D registered stack  $I_{\text{sub}.r}$  is calculated such that the applied corrective shifts can maximize the correlation (i.e., the normalized scalar product) between  $I_{\text{sub}.t'}[k; 1]$  and  $I_{\text{sub}.t'}[k; l]$ , for  $l > 1$ .

(101) Capillary Profile Segmentation

(102) Step 220 of method 200 in FIG. 2 is performed to achieve capillary profile segmentation, i.e., identify segments of capillaries in the images, in accordance with some embodiments. In some embodiments, segmentation is performed on the source images (with or without pre-processing). In some embodiments, segmentation is performed on normalized and/or registered images. In some embodiments, segmentation is performed on source images after some other processing, such as noise filtering and/or contrast improvements intended to emphasize capillary structures.

(103) In some embodiments, capillary segmentation is manual. A user may draw lines along the boundaries of the capillaries visible in the images. For example, step 220 may be performed by a user. The user may mark some internal contour points and external contour points on an image, after which a computer may retrieve the 2D coordinates of these marked internal and external contour points for further processing (e.g., resamples at step 230).

(104) In some embodiments, capillary segmentation is automated or semi-automated using methods such as thresholding and/or edge detection. Artificial intelligence methods may be used to train a computer-based pattern recognition model. In one example, a pattern recognition model may be based on historical images of capillaries such that the pattern recognition model can recognize similar capillary structures when a new image is provided. In another example, a pattern recognition model may be based on one or more capillary structures in one portion of an image

such that the pattern recognition model can recognize similar capillary structures in other portions of the image.

(105) In some embodiments, capillary segmentation may involve a hybrid approach, in which a user makes some initial and rough indications of the boundaries of capillaries and a computer-based program refines the initial indications using interpolation (e.g., linear interpolation, polynomial interpolation, or spline interpolation), curve fitting (e.g., using linear or nonlinear regression), and/or extrapolation (e.g., using linear extrapolation, polynomial extrapolation, conic extrapolation, or French extrapolation).

(106) In some embodiments, segmentation of each capillary is semi-automated with minimal user-defined 2D coordinates. For example, a user may define two sets of 2D coordinates,  $P_{\text{sub.int}}[j]$  and  $P_{\text{sub.ext}}[j]$ , with  $j=1, 2, \dots, N_{\text{sub.p}}$ , that follow the internal and external capillary boundaries as defined on the first frame of the stack  $I$ . Here,  $j$  is the index of the  $j$ th point on the contour, and  $N_{\text{sub.p}}$  is the total number of points specified by the user in each contour (internal or external). The total number of specified point  $N_{\text{sub.p}}$  can be dependent on several factors including, but not limited to, the complexity of the capillary boundaries and the length of the capillaries. Fewer points can be specified for straight capillaries or straight portions of capillaries, compared to capillaries with sharp turns. In some embodiments, the number of specified points  $N_{\text{sub.p}}$  may range from about 3 points to about 20 points. In some embodiments, the number of specified point  $N_{\text{sub.p}}$  may be about 5 points to about 10 points.

(107) The value of the point  $P_{\text{sub.int}}[j]$  or  $P_{\text{sub.ext}}[j]$  includes a vector that designates the location of this point in the 3D stack  $I$  or  $I_{\text{sub.r}}$ . For example,  $P_{\text{sub.int}}[5]$  refers to the fifth point on the internal contour of a capillary. The value of  $P_{\text{sub.int}}[5]$  may be, for example (20, 30), which indicates the 2D location of the point on the image, i.e., twentieth row and thirtieth column. After acquiring the 2D location of this point on the curve, the pixel value (or intensity) of the pixel may be retrieved from the image stack  $I$  or  $I_{\text{sub.r}}$ . In this way, index on the curve ( $j$ ), pixel location ( $k$ ), and pixel value are correlated to each other in a one-to-one manner.

(108) Resampling of Capillary Contour Points

(109) The contour points specified, for example, at step **220** of method **200**, are usually sparse and may only mark, for example, certain characteristic points on the internal and external boundaries of capillaries (e.g., starting point, ending point, or turning points). Therefore, at step **230** of method **200**, the specified internal and external contour points are resampled so as to further refine the boundaries for further processing in accordance with some embodiments.

(110) At least one of three methods and/or a combination thereof may be used to resample the specified contour points. In some embodiments, interpolation (e.g., linear interpolation, polynomial interpolation, or spline interpolation) is used to generate new data points between two adjacent specified points so as to fill the gap. In some embodiments, curve fitting (e.g., using linear or nonlinear regression) is used to fit the specified contour points to a curve, which generally has an analytic expression and therefore can contain an arbitrary number of data points for further processing. In some embodiments, extrapolation (e.g., using linear extrapolation, polynomial extrapolation, conic extrapolation, or French extrapolation) is employed to generate projected points beyond the curve section defined by the specified contour points. In further embodiments, a combination of two or more these methods is used.

(111) In some embodiments, a denser set of points  $P'_{\text{sub.int}}$  and  $P'_{\text{sub.ext}}$  is generated using cubic-spline interpolation of the original points with a resampling factor  $\alpha$ . The total number of contour points after resampling is therefore  $\alpha(N_{\text{sub.p}}-1)+1$ , where  $N_{\text{sub.p}}$  is the number of contour points specified. The resampling factor  $\alpha$  may be at least partially dependent on the desired resolution of the resampled contours, i.e., the distance between two adjacent resampled contour points (also referred to as point spacing). For example, if WBC events are to be detected, it is preferred to set the point spacing smaller than the size of WBCs so as to resolve each WBC in subsequent processing. In some embodiments, the point spacing may be substantially similar to the

pixel size in the source images in the capillary data.

(112) In some embodiments, resampling is performed directly on the 2D coordinates specified at step **220**. For example, 2D spline (also referred to as bicubic interpolation) may be used to resample the specified contour points. In some embodiments, the point-resampling operation at step **230** includes separate 1D resampling of the corresponding horizontal and vertical coordinate sequences (also referred to as row and column sequences, respectively). FIG. **4A** is a plot of a cubic spline interpolation of x-coordinates, and FIG. **4B** is a plot of a cubic spline interpolation of y-coordinates. In FIGS. **4A-4B**, the contour points specified at step **220** are marked as crosses (e.g., cross **400**) and the resampled contour points connect the crosses. Note that the resampled data points are so numerous that they appear as continuous curves (e.g., apparent curve **410**).

(113) Definition of Intermediate Curves and Curvilinear Distances

(114) At step **240** of method **200**, a series of intermediate curves are defined between the internal contour and the external contour of each identified capillary according to some embodiments. In some embodiments, the series of intermediate curves are evenly distributed in the space defined by the internal and external contours. In some embodiments, the distribution of intermediate curves is uneven. For example, the central portion of the capillary may have a higher density of intermediate curves compared to an edge portion of the capillary.

(115) In some embodiments, a series of N intermediate curves  $P'.sub.m[j]$  is generated by linear combinations of the form:

$$(116) \quad tP'_{int} + (1 - t)P'_{ext} \quad (4)$$

where  $m=1, 2, \dots, N.sub.c$ ,  $N.sub.c$  is the total number of intermediate curves;  $j=1, 2, \dots, \alpha(N.sub.p-1)+1$ ,  $\alpha(N.sub.p-1)+1$  is the total number of data points in each curve; and  $t=(m-1)/(N.sub.c-1)$  is a linear combination coefficient.

(117) The total number of intermediate curves  $N.sub.c$  may be dependent on the desired resolution of the collection of intermediate curves, i.e., the distance between two adjacent intermediate curves (also referred to as curve spacing). For example, if WBC events are to be detected, the curve spacing may be set smaller than the size of WBCs so as to resolve each WBC in subsequent processing. In some embodiments, the curve spacing may be substantially similar to the pixel size in the source images in the capillary data.

(118) The resampling of contour points at step **230** may be regarded as improving the longitudinal resolution (i.e., the resolution along the direction of the capillary) from specified contour points at step **220**. The creation of intermediate curves, on the other hand, may be regarded as improving the lateral resolution (i.e., the resolution along the cross-section of the capillary) based on two boundaries (i.e., the internal and external contours) of the capillary.

(119) In some embodiments, step **230** is performed before step **240** such that intermediate curves can be created based on the resampled contour points acquired at step **230**. In some embodiments, step **240** is performed before step **230**. For example, a series of intermediate points may be created between one user-specified point on the internal contour and one user-specified point on the external contour so as to fill gaps along the cross-section of the capillary. The same step may be performed for each pair of user-specified points, thereby generating a series of sets of intermediate contour points between the internal contour points and the external contour points. Then a resampling step, like the one at step **230**, may be performed for each set of intermediate contour points to string together the intermediate contour points, thereby generating a series of intermediate curves.

(120) At step **240**, a middle curve  $P'.sub.mid$  may be defined as:

$$(121) \quad P'_{mid} = 1 / 2P'_{int} + 1 / 2P'_{ext} \quad (5)$$

This middle curve  $P'.sub.mid$  may be used to define curvilinear distances. Curvilinear distance may be defined as the Euclidian norm between each point in  $P'.sub.mid[j]$  with respect to the starting point  $P'.sub.mid[1]$ . In some embodiments, for simplicity, the  $j$ th data points on different

intermediate curves  $P'.sub.m[j]$  are assigned the same curvilinear distances as  $P'.sub.mid[j]$ .

(122) FIG. 5 is a normalized and registered image frame  $I.sub.r$  from a video clip including capillary **500** and capillary **510**. Both capillaries are highlighted in the processed image along with the corresponding user-defined contour points (shown as crosses) and interpolated points (shown as curves) that follow the internal and external curves of each profile. The middle curve  $P'.sub.mid$  from which the curvilinear distances are computed is also shown. Note that the user has specified only six points and yet the resampled curves already appear to be in good agreement with the actual boundaries of the two capillaries.

(123) Intensity Profile Extraction

(124) At step **260** of method **200**, the intensities of the pixels (i.e., pixel values) within the capillary segments are extracted as a function of curvilinear distance so as to form a spatiotemporal profile  $f[j; m; l]$ , wherein  $j$  is the curvilinear index (the  $j$ th point on certain curve),  $m$  is the curve index (the  $m$ th curve in the plurality of curves including the internal boundary, the external boundary, and the intermediate curves generated in between), and  $l$  is the frame index (the  $l$ th image in a sequence of images). More specifically, each  $P'.sub.m[j]$  on  $I.sub.r$  is associated with an intensity value. In some embodiments, bilinear interpolation is used to compute the resulting intensities  $f[j; m; l]$  with sub-pixel precision at given curvilinear index  $j$ , curve  $m$ , and frame  $l$ .

(125) In some embodiments, given  $f[j; m; l]$ , the average of the capillary intensities of all curves can be computed for every frame and curvilinear distance so as to generate an averaged spatiotemporal profile  $f'[j; l]$  (i.e., averaged over all  $m$  from 1 to  $N.sub.c$ ). As an analogy, this averaging step can be regarded as collapsing all capillary curves (internal contour, external contour, and intermediate curves) into a single curve.

(126) In some embodiments, the averaged spatiotemporal profile  $f'[j; l]$  is resampled to generate a resampled spatiotemporal profile  $g[j; l]$ , which contains the same number of samples as  $f'[j; l]$  but with equidistant curvilinear spacing. The resampling may be performed using linear interpolation.

(127) Spatiotemporal Profile Analysis

(128) The profile  $g[j; l]$  may include an intensity profile evolving as a function of time for each point  $j$  along the curvilinear distance of each capillary. This profile can exhibit correlations in space and time, which may be extracted to overcome possible challenges in analyzing noisy source images taken at relatively low-frame-rate and/or with low-resolution.

(129) In some embodiments, to emphasize the intensity variations created by WBC events, a median-normalized version of  $g$  is computed. More specifically, the medians of the time-varying intensity lines of  $g[j; l]$  may be first set to zero at every curvilinear coordinate  $j$ . Then the same operation may be performed column-wise at every frame  $l$ . To reduce noise, the contrast-normalized profile  $g'$  may be filtered along the time axis with a symmetric and unit-sum rectangle function of size  $\sigma$ , which yields  $g''$ . The filtering operation may be performed through convolution with said rectangle function.

(130) FIG. 6A shows an example spatiotemporal profile  $g''$  of capillary **500** from FIG. 5. The spatiotemporal profile  $g''$  was generated based on the original spatiotemporal profile  $f[j; m; l]$ , after averaging over all  $m$  from 1 to  $N.sub.c$  (achieve  $f'[j; l]$ ), resampling to have equidistant curvilinear spacing (achieve  $g[j; l]$ ), median-normalization (to achieve  $g'[j; l]$ ), and filtering (to achieve  $g''[j; l]$ ). On the spatiotemporal profile shown in FIG. 6A, spatiotemporal trajectories corresponding to WBC events can be identified. FIG. 6B illustrates these trajectories by dashed lines spanning the 2D intensity plot. The slope of each line may be associated with the average speed of the corresponding WBC event inside the capillary. Therefore, the spatiotemporal profiles like those shown in FIGS. 6A-6B already provide important information about WBC events in the capillaries such as the number of events and the flow speed. This information may be extracted manually, automatically, or semi-automatically using the methods described above.

(131) Radon Transform

(132) At step **270** of method **200**, a Radon transform is performed on the spatiotemporal profiles

generated in step 260 according to some embodiments. The Radon transform maps 2D lines to peaks located at particular positions so as to identify events and their associated parameters. Event detection using Radon transform is not only convenient but robust to noise.

(133) Without being bound by any particular theory or mode of operation, given a continuous 2D image  $f(x)$ , wherein  $x$  is a 2D Cartesian coordinate defined with respect to the center of the image  $f(x)$ , the Radon transform called  $\{\text{circumflex over } (f)\} = Rf$  may be defined as

$$(134) \hat{f}(x', \theta) = \int_{-\infty}^{\infty} f(x_1' \cos \theta - x_2' \sin \theta, x_1' \sin \theta + x_2' \cos \theta) dx_2' \quad (6)$$

where the radial coordinate  $x'$  is defined as  $x' = [x_{\text{sub.1}} \cos \theta + x_{\text{sub.2}} \sin \theta, -x_{\text{sub.1}} \sin \theta + x_{\text{sub.2}} \cos \theta]$ .

(135) In some embodiments,  $f(x)$  is a discrete image, in which case a discrete-domain Radon transform  $R_{\text{sup.0}}$  involving a finite amount of radial-coordinate values and of angles in  $[0; \pi]$  may be used. The largest radial-coordinate value can correspond to half of the image-diagonal length. The profile in Radon-domain  $\hat{g}$  is thus represented as:

$$(136) \hat{g}[k, k_r] = R^0 g'' \quad (7)$$

The number of angles is denoted by  $N_{\text{sub.}\theta}$ , the number of radial coordinates  $N_{\text{sub.}r}$  being proportional to  $(N_{\text{sub.f.sup.2}} + N_{\text{sub.p.i.sup.2}})_{\text{sup.1/2}}$ , where  $N_{\text{sub.p.i}} = \alpha(N_{\text{sub.p}} - 1) + 1$  is the number of interpolated curvilinear points.

(137) FIG. 7 illustrates the application of the Radon transform on the spatiotemporal profile shown in FIGS. 6A-6B according to some embodiments. The projection angle  $\theta$  and radial coordinate  $R$  are shown in FIG. 7. The solid arrow illustrates the direction for trajectory-line detection.

Considering a predefined set of angles  $\theta$  and radial coordinates  $R$ , the Radon transform computes projections of the spatiotemporal-profile intensities (i.e., the intensities in the non-transformed domain, as shown in FIG. 7). More specifically, the Radon-transformed-domain value (see FIG. 8A) for a given angle  $\theta$  and radial coordinates  $R$  corresponds to the integral of all values (i.e., the intensity values in the non-transformed domain, as shown in FIG. 7) that are found on the line whose counterclockwise angular inclination with respect to the horizontal axis is  $\theta$  and whose radial coordinate is  $R$ .

(138) FIG. 8A shows the Radon transform  $\hat{g}$  of the map in FIG. 7 according to some embodiments. The horizontal and vertical axes correspond to the projection angle and to the associated normalized radial coordinate, respectively. In FIG. 8A, several peaks may be readily identified. Each peak may correspond to the linear trajectories observed in the spatial domain (e.g., FIG. 6B). These peaks may be identified and located based on, for example, local-maxima detection within a window of odd pixel size  $S_{\text{sub.w}} \times S_{\text{sub.w}}$ . In some embodiments, the local-maxima are limited to those greater than a threshold  $rm$ . In some embodiments, the maxima locations are limited to locations with angular values within the range  $[0; \pi/2]$ , thereby imposing one single flow direction inside the capillary.

(139) FIG. 8B shows the spatiotemporal profile in the Radon domain with identified peaks highlighted in circles. The original physical time and speed parameters of WBC events in the capillaries may be analytically deduced from the maxima locations based on the known frame rate and pixel size through elementary trigonometric relations. More specifically, the speed is associated with the tangent of the projection angle  $\theta$  in the Radon domain, and is thus proportional to the vertical slope of the corresponding trajectory line in the aforementioned spatiotemporal profile  $g''$ . The original physical time is associated with the intersection between said trajectory line and the time axis of said spatiotemporal profile. In some embodiments, the time of each WBC event corresponds to the first frame in which a visual gap appears in the capillary.

(140) FIG. 9A shows experimental results of WBC events occurring inside capillary 500, and FIG. 9B shows experimental results of WBC events occurring inside capillary 510 shown in FIG. 5 according to some embodiments. The experimental results are compared to manual counts performed by four trained human reviewers. In FIGS. 9A-9B, WBC events detected by the



methods described above are marked by a cross, while the event times estimated by a trained human reviewer are denoted by the dashed vertical lines. The horizontal lines represent the maximum and minimum blood-flow-related limits.

(141) The source images are taken from a video clip of a human nailfold. The acquisition parameters are  $N_{sub.h}=1280$ ,  $N=960$ ,  $N_{sub.f}=450$ ,  $r=15$ , and  $S_{sub.p}=0.65 \mu m$ , the duration of the video clip is 30 s. The threshold  $\tau_{sub.c}$  is heuristically set to  $\frac{3}{4}$  of the maximum intensity value for each frame  $l$  in  $I'$ . The amount of user specified curve points is set to  $N_{sub.p}=6$ , which can yield accurate segmentations. The number of interpolated curves is set to  $N_{sub.c}=10$ , using  $\alpha=100$  for resampling. The size of the filter used for noise reduction is set to  $\sigma=3$ . Finally, the window size and threshold value used for Radon-domain maxima detection are selected as  $S_{sub.w}=11$  and  $\tau_{sub.m}=7$ , the number of Radon angles being set to  $N_{sub.\theta}=400$ .

(142) In FIGS. 9A-9B, more than 80% of the WBC events detected by the methods described above are consistent with those of a trained human reviewer. Missed events may correspond to temporally adjacent visual gaps that can be challenging for automatic methods to resolve due to the poor frame rate.

(143) FIG. 10 shows a further comparison between the total WBC event counts obtained from methods described above in accordance with some embodiments and those obtained from all four trained human reviewers. FIG. 10 also shows significant inter-observer variability of manual counts. Each capillary is associated with a box where the central mark is the median. The edges of the box are the 25th and 75th percentiles, and the whiskers extend to the extreme data points. The crosses and the circles denote the counts completed by each of the four trained human reviewers and by the approaches described herein, respectively. The results obtained from the described methods are shown in these box plots to fall within the human inter-rater variability.

(144) The slope of the visual gap trajectories in FIGS. 6A-7B may be employed to compute the speed associated with WBC events for both capillary 500 and capillary 510. The results, represented in FIGS. 9A-9B, fall within the range for blood-flow values of human nailfold capillaries previously reported in literature, that is, about  $450 \mu m/s$  to about  $1200 \mu m/s$ .

(145) Interpolated inner and outer capillary curves,  $P_{sub.int}[j]$ ,  $P_{sub.ext}[j]$ , may be employed to extract the vessel radius  $r$ , which corresponded to approximately  $7.5 \mu m$  for both capillary 500 and capillary 510, a value consistent with previous published data.

(146) Without being bound any particular theory or mode of operation, capillaries may be assumed to have circular cross-sections. Given that the average speed  $v$  derived above is approximately  $600 \mu m/s$ , the total sampled blood volume per second  $V$  may be determined as:

$$(147) \quad V = vr^2 = \frac{600}{s} \cdot \frac{m}{s} \cdot (7.5 \text{ } m)^2 \approx 105 \cdot 10^{-6} \frac{L}{s} \quad (8)$$

(148) Given that a healthy WBC range is about 3500 WBCs per  $\mu L$  to about 9000 WBCs per  $\mu L$ , and given that the duration of the video clip is 30 seconds, a number  $c$  of WBC counts may be determined as:

$$(149) \quad c = [3.5, 9] \cdot 10^3 \frac{wbc}{L} 105 \cdot 10^{-6} \frac{L}{s} \cdot 30s \approx [11, 28] wbc \quad (9)$$

which is consistent with the median counts of ten WBC events and eleven WBC events obtained for capillary 500 and capillary 510, respectively.

Apparatus and Systems for Non-Invasive and In Vivo Analysis of Blood Cell Dynamics

(150) FIGS. 11A-11B are schematics of a system for detecting white blood cell (WBC) events in an in vivo and non-invasive manner according to some embodiments. In some embodiment, some or all aspects of the system of FIGS. 11A-11B can be structurally and/or functionally similar to one or more of the systems, apparatuses, and devices as described herein such as, for example, the system 2300 and/or the device 2340, as described in greater detail with respect to FIG. 23.

(151) FIG. 11A is a side view of the system, and FIG. 11B is a top view of the system. For purposes of illustration, embodiments described herein analyze WBC events in a human nailfold; however, the embodiments may be modified for analysis in other subjects and/or other locations in or on the

body of a subject. In FIGS. 11A-11B, system 1100 includes finger holder 1110 having finger hole 1112 to receive at least a portion of a human finger (e.g., a nailfold portion of the finger). Finger holder 1110 is also configured to receive imager 1120, which is in optical communication with the finger received by finger hole 1112 through transparent window 1114 so as to capture images or videos of the finger. The imager further includes focusing optic 1122 to collect light reflected or scattered from the finger and detector 1124 to receive the reflected or scattered light so as to form images of the finger. System 1100 further includes processor 1130 operably coupled to imager 1120 and memory 1140 operably coupled to processor 1130. Memory 1140 is encoded with processor-executable instructions, which, when executed by processor 1130, may perform the methods described above to analyze images received from imager 1120. System 1100 also includes display 1150, which can display the images or videos taken by imager 1120 and/or data associated with WBC events detected by processor 1130.

(152) In some embodiments, finger holder 1110 has an igloo shape (as shown in FIGS. 11A-11B) such that the hand can rest on the dome of the finger holder while a finger in the hand is received by finger hole 1112 for imaging. Finger holder 1110 may have other configurations such as a flat top, a handle configuration (the hand can grip the handle while a finger can be imaged), or any other configurations known in the art.

(153) In some embodiments, system 1100 also includes illumination source 1160 (shown in FIG. 11B) to illuminate the finger and facilitate image taking by imager 120. In some embodiments, illumination source 1160 includes a pair of light emission diodes (LEDs), each of which is disposed on one side of finger hole 1112. In some embodiments, illumination source 1160 is configured to emit monochromatic light. Capillary structures in the finger can have a high reflectivity at the wavelength of the monochromatic light.

(154) FIG. 11C shows a schematic of a system 1100 substantially similar to the system shown in FIGS. 11A-11B in accordance with some embodiments. The system 1100 includes an adjustable transparent window 1115 disposed between finger hole 1112 and imager 1120. By adjusting the height of window 1115, imagers 1120 having different sizes may be used to capture images of the finger.

(155) FIGS. 12A-12B are schematics of a system for capturing in vivo images for non-invasive analysis of WBC events according to some embodiments. In some embodiment, some or all aspects of the system of FIGS. 12A-12B can be structurally and/or functionally similar to one or more of the systems, apparatuses, and devices as described herein such as, for example, the system 2300 and/or the device 2340, as described in greater detail with respect to FIG. 23.

(156) FIG. 12A is a side view of system 1200, and FIG. 12B is a top view of system 1200. System 1200 includes finger holder 1210 having finger hole 1212 to receive at least a portion of a human finger (e.g., a nailfold portion of the finger). Finger holder 1210 is also configured to receive imager 1220, which is in optical communication with the finger received by finger hole 1212 through transparent window 1214 and mirror 1226 so as to take images or videos of the finger. The imager further includes focusing optic 1222 to collect light reflected or scattered from the finger and detector 1224 to receive the reflected or scattered light so as to form images of the finger. In system 1200, imager 1220 is disposed in a vertical configuration. Mirror 1226 is configured to reflect the image of the finger toward imager 1220. In some embodiments, mirror 1226 is coupled to an actuator (not shown), which can tilt mirror 1226 in two directions. The tilting may help imager 1220 point at the desired portion of the finger for imaging. Similar to system 1100, system 1200 also may have an illumination source 1260 to facilitate capturing images by imager 1220.

(157) FIG. 13 is a schematic of a system for performing in vivo and non-invasive analysis of blood cell dynamics using a camera-equipped device (e.g., a smartphone) according to some embodiments. In some embodiment, some or all aspects of the system of FIG. 13 can be structurally and/or functionally similar to one or more of the systems, apparatuses, and devices as described herein such as, for example, the system 2300 and/or the device 2340, as described in

greater detail with respect to FIG. 23.

(158) System **1300** includes finger holder **1310** having finger hole **1312** to receive at least a portion of a finger for imaging. Finger holder **1310** is also configured to receive smartphone **1320** such that the camera in smartphone **1320** is in optical communication with the finger in finger hole **1312** via transparent window **1315** and mirror **1326**. System **1300** also may include modifying optic **1322**, disposed in front of the camera in smartphone **1320**, so as to adapt smartphone **1320** for better image capture. For example, modifying optic **1322** may include a lens to adjust the focal length (optical zooming) of the camera in smartphone **1322**. Cameras in many smartphones do not have optical zooming, thus including lens **1322** may increase the optical flexibility of the camera. The focal length of the camera is also related to the resolution of the images captured by the camera. Therefore, use of lens **1322** also may adjust the resolution of the images for further processing.

(159) Smartphone **1320** generally includes its own memory and processor. Methods described in earlier sections of this application can be encoded as processor executable instructions into the memory of smartphone **1320**. In operation, images taken by the camera may be transmitted to the processor for the analysis of blood cell dynamics. In some embodiments, images taken by the camera are transmitted wirelessly (e.g., via Bluetooth, WiFi, 3G network, 4G network, or any other wireless communication protocols known in the art) to another processor for processing. In some embodiments, images taken by the camera are locally saved into the memory of smartphone **1320**.

(160) FIGS. **14A-14D** are images of systems and apparatus for in vivo and non-invasive analysis of blood cell dynamics according to some embodiments. In some embodiment, some or all aspects of the systems and apparatus of FIG. **14A-14D** can be structurally and/or functionally similar to one or more of the systems, apparatuses, and devices as described herein such as, for example, the system **2300** and/or the device **2340**, as described in greater detail with respect to FIG. 23.

(161) FIG. **14A** shows a finger holder coupled to an imager. The imager may use a commercially available capillaroscope (e.g., Dino-Lite Digital Microscope (available from BigC.com (Torrance, CA)). The imager may include its own illumination source such that when a finger is placed in the finger hole, the finger is well illuminated for imaging. FIG. **14B** shows an imager and a finger holder de-coupled. FIG. **14C** shows a finger holder when a finger is placed in the finger hole. FIG. **14D** shows a system including a finger holder, an imager, and a computer that is connected to the imager via, e.g., a USB connection. The computer may display, in real time, images or video captured by the imager. Methods described in earlier sections of this application may be saved as processor executable instructions in a memory of the computer, a processor of which then may perform analysis of the images to detect WBC events.

(162) FIGS. **15A-15G** are views of an adapter that can be attached to a smartphone for capturing images of a nail fold with a camera-equipped device for blood cell dynamics analysis in accordance with some embodiments. FIG. **15A** is a perspective view of adapter **1500** including window section **1510** and a plurality of suction cups **1520**. Window section **1510** may be aligned with the camera typically available in smartphones. Suction cups **1520** may secure adapter **1500** to, for example, a smartphone. While four suction cups are shown in FIG. **15A**, the number of the suction cups can be any number that is applicable. Alternatively or in addition, an adapter may be attached or secured to a smartphone or other device using a clip, adhesive, etc.

(163) FIG. **15B** shows adapter **1500** from perspective angle to illustrate the structure of window section **1510**, which further includes window **1512** and finger receptor **1514**. Window **1512** is substantially transparent or at least transparent at certain wavelengths so as to allow the camera to take images of fingers. Finger receptor **1514** has an internal contour that fits the general shape of fingers so as to firmly secure fingers with adapter **1500**, thereby reducing burden of image registration (e.g., due to movement) in subsequent processing.

(164) FIG. **15C** is a top view of adapter **1500**, FIG. **15D** is a first side view of adapter **1500**, and FIG. **15E** is a back view of adapter **1500** illustrating illumination channel **1516** and window **1512**. FIG. **15G** is a front view (the side

receiving the finger) of adapter **1500**. As shown in FIGS. **15E** and **15G**, illumination channel **1516** is generally not through the entire depth of adapter **1500**. Instead, illumination channel **1516** may be in optical communication with a flash light that is generally available in smartphones and other camera-equipped devices beside the camera lens. Illumination channel **1516** may receive light emitted by the flash light and reflect it toward window **1512** so as to illuminate at least a portion of the finger to be imaged.

(165) FIGS. **15H-15J** illustrate illumination channel **1516**. FIG. **15H** is a perspective view of adapter **1500**. FIG. **15I** is a perspective cross-sectional view of part of adapter **1500** to illustrate window **1512** and illumination channel **1516**. FIG. **15J** is a cross-sectional view of adapter **1500** to illustrate structures of illumination channel **1516**. In particular, illumination channel **1516** may include a curved surface **1517** that reflects received light toward window **1512** so as to illuminate a finger typically disposed in front of window **1512** for imaging.

(166) FIG. **16** is a schematic of a system including a smartphone and an adapter for capturing images of a nail fold for blood cell dynamics analysis in accordance with some embodiments. In some embodiment, some or all aspects of the system of FIG. **16** can be structurally and/or functionally similar to one or more of the systems, apparatuses, and devices as described herein such as, for example, the system **2300** and/or the device **2340**, as described in greater detail with respect to FIG. **23**.

(167) Adapter **1600** includes window **1612** in optical communication with camera **1632** of smartphone **1630**. Adapter **1600** also includes illumination channel **1616** in optical communication with LED light **1636** of smartphone **1630**. Illumination channel **1616** receives light emitted by LED light **1636**, and curved surface **1617** in illumination channel **1616** reflects the received light toward window **1612** so as to illuminate the finger **1640** (more specifically nailfold **1642**), which is in close contact with window **1612**.

(168) In some embodiments, window **1612** may include two lenses to change the focal length of camera **1632** in smartphone **1630**. Changing the focal length can also change the resolution of the images taken by camera **1632**. In some examples, index matched fluid **1618** may be disposed between window **1612** and nailfold **1642**. Index matched fluid **1618** may have a refractive index similar to that of a nailfold or of the material of window **1612** so as to reduce specular reflection at the surface of window **1612** or at the surface of nailfold **1642**. In some embodiments, index matched fluid **1618** has high viscosity. In some embodiments, index matched fluid **1618** may be replaced by a compliant reusable transparent plastic.

(169) FIG. **17A** shows a smartphone with an adapter attached to the smartphone so as to allow image taking of a nailfold according to some embodiments. FIG. **17B** shows the smartphone and the adapter when a finger is placed in front of the adapter for imaging. FIG. **18** is an image captured by the smartphone using the adapter shown in FIGS. **17A-17B**. Multiple capillary structures are visible in the image for further analysis of blood cell dynamics in accordance with some embodiments.

(170) FIG. **19** is a schematic of a clamp device for capturing images and performing blood cell dynamics analysis according to some embodiments. Clamp device **1900** includes spring-loaded casing **1910** for securely receiving finger **1950**. When finger **1950** is placed in clamp device **1900**, camera **1930** can take images of finger **1950** with finger **1950** illuminated by a pair of LED lights **1940a** and **1940b**. In some embodiments, LED lights **1940a** and **1940b** emit broad-spectrum white light. In some embodiments, LED lights **1940a** and **1940b** emit green light which can be effectively reflected by WBCs. Clamp device also may include a battery and/or processing unit **1920** for processing images taken by camera **1930** according to methods described above. FIG. **20** shows a clamp device coupled with a finger for blood cell dynamics analysis. As can be seen from FIG. **20**, the spring-loaded casing helps to secure the finger with the clamp device so as to reduce or eliminate relative movement between the finger and the camera.

(171) FIGS. **21A-21O** are views of an adapter for capturing images of a nailfold with a smartphone

camera for capillaroscopy and hematology analysis in accordance with some embodiments. In particular, FIGS. **21A-21F** are images of perspective views of a smartphone adapter. In FIGS. **21A-21E**, the adapter is attached to a smartphone such that the smartphone camera may be utilized. In FIG. **21F**, the adapter is shown unattached. FIGS. **21G-21O** are wireframes showing the side and perspective views of the adapter. FIGS. **22A-22D** illustrate a method of using a smartphone adapter attached to a smartphone such that the smartphone camera may be used for capillaroscopy and hematology analysis according to some embodiments. In FIG. **22A**, index matched fluid is disposed on the surface of a nail fold of a user. In FIGS. **22B-22D**, the smartphone is positioned over the finger such that the adapter rests on the finger and the smartphone camera is aligned with the nailfold.

(172) FIG. **23** is a schematic illustration of an environment/system **2300** in which non-invasive hematological measurements can be implemented and/or carried out. In some embodiments, aspects of the system **2300** can be structurally and/or functionally similar to the systems, apparatuses, and/or devices described herein with respect to FIGS. **1-22** and **31-60**, and/or can perform the methods described in FIGS. **1-2**.

(173) The system **2300** includes a platform **2310**, an illumination source **2330**, an imaging device **2320**, and a compute device **2340**. In some embodiments, all components of the system **2300** can be included in a common casing such as, for example, a single housing that presents the system **2300** as an integrated, one-piece device for a user. In other embodiments, at least some components of the system **2300** can be in separate locations, housings, and/or devices. For example, in some embodiments, the compute device **2340** can be a smartphone in communication with the illumination source **2320** and/or the imaging device **2330** via one or more networks, each of which can be any type of network such as, for example, a local area network (LAN), a wide area network (WAN), a virtual network, a telecommunications network, and/or the Internet, implemented as a wired network and/or a wireless network. Any or all communications can be secured (e.g., encrypted) or unsecured, as is known in the art. The system **2300** and/or the compute device **2340** can be or encompass a personal computer, a server, a work station, a tablet, a mobile device, a cloud computing environment, an application or a module running on any of these platforms, and/or the like.

(174) It is understood that while described herein as a system for hematological measurements in a nailfold portion for ease of explanation, aspects of the systems, devices, and methods disclosed herein are useful for hematological measurements in any tissue having a capillary structure (e.g., a capillary bed, superficial capillaries, peripheral capillaries, capillaries in other portions of the finger of the user, and/or the like) that can be imaged as described herein. Non limiting examples include capillaries in retina, ear lobes, lips, gums, and/or the like. As an example, the platform **2310** can be adapted to be pressed against a gum line of a user during use for hematological measurements in a capillary bed of the gum line. As another example, the platform **2310** can encompass a tonometer-like instrument for pressing against the retina during use for hematological measurements in capillaries of the retina.

(175) In some embodiments, the platform **2310** receives a finger of a user during use. In some embodiments, the platform **2310** can be structurally and/or functionally similar to the finger holder(s) described in FIGS. **11-14, 19**. In some embodiments, the platform **2310** is shaped to guide the placement of the finger of a user so as to position a nailfold portion of the finger in a predetermined location within the platform.

(176) The illumination source can be any suitable source of substantially monochromatic light including, but not limited to, light emitting diodes (LEDs), laser light, filtered light, and/or the like. The illumination source can be positioned with respect to the platform **2310** to illuminate the nailfold portion of the finger of the user during use.

(177) The imaging device **2330** can include any suitable imager as disclosed herein, including a smartphone camera, a capillaroscope, and/or the like. In some embodiments, the imaging device

**2330** captures images of the nailfold portion of the finger of the user during use in response to the illumination of the nailfold portion by the illumination source **2330**, such as, for example, based on a synchronization/timing signal from the device **2340**. In some embodiments, the imaging device **2330** captures a set of images per acquisition such as, for example, a time-lapse series. In some embodiments, the imaging device **2330** captures the set of images as a video/video file at a capture rate of, for example, 60 frames/second, for 60 seconds.

(178) In some embodiments, the platform **2310** is optically coupled to the illumination source **2330** and the imaging device **2330** via any suitable and independent means such as, for example, beam shaping and/or beam steering optics, one or more optical conduits such as optical fiber(s), direct/optics-free coupling, and/or the like.

(179) The compute device **2340** includes at least a controller **2350** and a memory **2360**. FIG. 23 also illustrates a database **2370**, although it will be understood that, in some embodiments, the database **2370** and the memory **2360** can be a common data store. In some embodiments, the database **2370** constitutes one or more databases. Further, in other embodiments (not shown), at least one database can be external to the device **2340** and/or the system **2300**. The compute device **2340** can also include one or more input/output (I/O) interfaces (not shown), implemented in software and/or hardware, for other components of the system **2300**, and/or external to the system **2300**, to interact with the device **2340**.

(180) The memory **2360** and/or the database **2370** can independently be, for example, a random access memory (RAM), a memory buffer, a hard drive, a database, an erasable programmable read-only memory (EPROM), an electrically erasable read-only memory (EEPROM), a read-only memory (ROM), Flash memory, and/or so forth. The memory **2360** and/or the database **2370** can store instructions to cause the controller **2350** to execute processes and/or functions associated with the system **2300**.

(181) The controller **2350** can be any suitable processing device configured to run and/or execute a set of instructions or code associated with the device **2340**. The controller **2350** can be, for example, a general purpose processor, a Field Programmable Gate Array (FPGA), an Application Specific Integrated Circuit (ASIC), a Digital Signal Processor (DSP), and/or the like.

(182) The controller **2350** receives the set of images/video data from the imaging device **2330**. The controller **2350** can execute computer-executable instructions (e.g., those stored in the memory **2360** and/or the database **2370**) to process the set of images in any suitable manner. In some embodiments, for example, given an input raw video/set of images with a resolution of  $1280 \times 1024$  pixels and a frame rate of 60 frames/images per second, and given an input initial frame index, the controller **2350** can extract two uncompressed videos restricted to a duration of one minute (3600 frames) starting from that initial frame index. In some embodiments, the first video at the native pixel resolution, is downsampled at, for example, half of the pixel resolution ( $640 \times 512$ ), in order to accelerate processing during registration and capillary detection, as described herein. An uncompressed image is also extracted as the first frame/image of the second video.

(183) In some embodiments, the controller **2350** executes a global registration process on the set of images to eliminate movements that occur between frames/images. For example, in some embodiments, the controller **2350** aligns all images with respect to the first image of the set of images. In some embodiments, the alignment includes correcting for horizontal and/or vertical translations of the view captures in the set of images. In some embodiments, the controller **2350** corrects the horizontal and/or vertical translation for each image in a manner that maximizes its cross-correlation with the first image.

(184) In some embodiments, prior to such an alignment process, the controller **2350** normalizes the intensity of each image of the set of images by, for example, a spatial high-pass filter based on predetermined characteristics (e.g., a square filter of size  $75 \times 75$  pixels), and/or any other suitable image-flattening techniques. In this manner, the resulting, processed set of images (sometimes also referred to simply as “the set of images”) are cropped to a viewing area that remains in view across

the entire set of images.

(185) The controller **2350** can execute computer-executable instructions to (e.g., those stored in the memory **2360** and/or the database **2370**) detect, in each image of the processed set of images, one or more capillaries in the nailfold portion of the finger to identify a first set of capillaries across the set of images. In some embodiments, detecting the first set of capillaries includes detecting each capillary of the first set of capillaries on at least one image of the set of images.

(186) In some embodiments, the controller **2350** detects each capillary of the first set of capillaries as follows. The controller **2350** receives training data that includes images of capillaries that fulfill one or more predetermined criterion for one or more attributes (e.g., at least for a first attribute of the one or more attributes) of the identified capillaries. In some embodiments, the one or more attributes include structural attributes of the capillary itself such as, but not limited to, capillary length (e.g., a sufficient length such that a cellular event moving at a typical or maximum blood flow speed would appear in more than one frame given the imager/imaging device's frame rate), capillary width (e.g., a capillary width from about 10  $\mu\text{m}$  to about 20  $\mu\text{m}$ , including all values and sub-ranges in between), capillary depth (e.g., a capillary depth from about 10  $\mu\text{m}$  to about 350  $\mu\text{m}$ , including all values and sub-ranges in between), average capillary diameter, lateral capillary diameter, vertical capillary diameter, capillary shape (e.g. capillaries must exhibit clear arterial and venous limbs), and/or the like.

(187) The average capillary diameter can be generally characterized as any average of multiple diameter measurements of the capillary, either at a single cross section, or at multiple cross sections along the length of the capillary. In some embodiments, the structural attribute is average capillary diameter, and the predetermined criterion is that the average capillary diameter must be between about 10  $\mu\text{m}$  to about 20  $\mu\text{m}$ .


(188) In some embodiments, the one or more attributes include flow attributes such as, but not limited to, blood flow speed in the capillary, transit time for a cell within the visible portion of the capillary, volumetric flow rate, mass flow rate, directionality of the flow, blood flow speed stability, and/or the like.


(189) In some embodiments, the one or more attributes include imaging attributes of the image of the capillary such as, but not limited to, contrast (e.g., based on measurement of luminance contrast, root mean square (RMS) contrast, Weber contrast, Michelson contrast, histogram-based techniques, and/or the like), focus/detail (e.g., as measured by gradient-based operators, Laplacian operators, wavelet operators, discrete cosine transform (DCT), frequency domain analysis, phase coherency, luminance map, singular value decomposition, learning algorithm(s), and/or the like), signal-to-noise ratio, image stability (e.g. as measured by image registration techniques, optical flow and/or the like), and/or the like. In some embodiments, a combination of structural and imaging attributes can be employed. In some embodiments, the training data is human-expert generated data that also accounts for requirements that the capillaries be generally clear (e.g., no air bubbles can occlude the capillaries) and have clear morphology (e.g., have clear arterial and venous limbs). The controller **2350** trains a deep learning neural network (e.g., a fully convolutional neural network, such as the deep learning YOLO method/technique as generally disclosed in Joseph Redmon et al. 2016, The IEEE Conference on Computer Vision and Pattern Recognition, the entire disclosure of which is incorporated herein by reference) based on the training data to recognize the first set of capillaries in the set of images.

(190) In some embodiments, the controller **2350** generates, for each detected capillary in each image of the set of images, a bounding box around that capillary, and also generates a confidence value associated with the likelihood that the detection corresponds to a capillary, and not another structure/artifact. In some embodiments, the first set of capillaries include those detected capillaries having a corresponding confidence value that meets or exceeds a predetermined confidence threshold.

(191) In some embodiments, the controller **2350** identifies a second set of capillaries from the first

set of capillaries. In some embodiments, the second set of capillaries includes those capillaries that are detectable in a threshold number of images, of the set of images. For example, if the set of images includes 60 images, the second set of capillaries can include those capillaries visible in at least 40 of the 60 images. In some embodiments, the second set of capillaries includes those capillaries that are detectable in a threshold number of images and are associated with a confidence value that exceeds the confidence threshold in a minimum or all of those images. In some embodiments, the controller **2350** generates an indication of the threshold number of images based on training data.

(192) In an example embodiment, the controller **2350** feeds the neural network as described herein with 130 training images having 795 corresponding bounding boxes (around capillaries) created manually. The training images were extracted as the first frames/images of 130 distinct capillary videos/sets of images stemming from 43 distinct patients, thus ensuring sufficient data diversity. The bounding boxes were manually defined by one human expert around each capillary that fulfill the set of criteria as described herein. The image dataset is split into a first set and a second set based on temporal order of acquisition, and the confidence threshold was set to  custom character =0.45 to avoid detections of unsuitable capillaries or artefacts. This condition detected, as the first set of capillaries, in the first set, 66 images from 23 patients with a total of 416 annotated bounding boxes around identified capillaries, and in the second set, 64 images from 19 patients with a total of 379 annotated bounding boxes around identified capillaries. The neuronal network was fed with the first set and the second for a total of 900 iterations each time, thus creating corresponding learned weights  $W_{sub.s1}$  and  $W_{sub.s2}$ . Explained with reference to the exemplified YOLO technique, in some embodiments, these learned weights  $W_{sub.s1}$  and  $W_{sub.s2}$  are determined as the free parameters of a convolutional-neural-network structure and optimized in such a way that the capillaries detected by the neural network, when executed on the images from the training set, best match those that the human-rater pre-labeled on these same images as a reference.

(193) Following the above single-frame-detection step/identification of the first set of capillaries, each capillary was then tracked with a given identifier. The capillary tracking is based on overlapping and Kalman filtering, in the event missed detection occurs during frames, though it is understood that any other suitable technique may be used for capillary tracking including, but not limited to, mathematical morphology, cross-correlation, mutual information, optical flow, machine learning, and/or the like. A capillary is selected for the second set of capillaries if it is in at least  $t_{sub.f}$  images (threshold number of images) i.e., if it is associated with a bounding box exceeding the confidence parameter  custom character in  $t_{sub.f}$  images, as shown in FIGS. **24A-24B**. The parameter  $t_{sub.f}$  was empirically set to 600, except if less than 3 capillaries were selected. In the latter case,  $t_{sub.f}$  was set such that 3 capillaries were detected if possible (i.e., provided that at least 3 distinct capillaries were detected in single images).

(194) To test the selection of the first set of capillaries, the steps mentioned herein (for detecting the first set of capillaries) are run on the first set with the weight  $W_{sub.s2}$ , and the set second set with the weight  $W_{sub.s1}$ . To validate the detection of the first set of capillaries, a comparison is made to a reference of 24 first images from 24 distinct sets of reference images/reference videos, where capillary boxes are annotated by two human experts who selected capillaries according to the following set of criteria: (A) Illumination. Capillaries must be visible with sufficient contrast to an observer; (B) Focus. Detailed capillary structures/dynamics must be visible and not blurred out; (C) Flow. Blood flow must exist to allow for potential events to be identified and counted; (D) Stability. Capillaries must fully remain within the video FOV in all frames; (E) Visibility. No object (e.g., air bubbles) can occlude capillaries. (F) Morphology. Capillaries must exhibit clear arterial and venous limbs. In the test videos/sets of images, for instance, 95% of the videos had 3 or more detected capillaries, and is associated with improved classification results. An example of capillary detection performed as detailed herein is illustrated in FIG. **25**.

(195) Referring again to FIG. **23**, in some embodiments, the controller **23** detects, in the second set



of capillaries, a set of (i.e., one or more) cellular events. In some embodiments, each cellular event of the set of cellular events is associated with passage of a white blood cell in a capillary of the second set of capillaries. As described in more detail herein, since red blood cells exhibit greater optical absorption than white blood cells at the wavelength(s) described herein, passage of a white blood cell in a capillary results in an “absorption gap” due to the presence of the white blood cell. (196) Accordingly, the term “cellular event” as used herein, and also sometimes referred to as a “gap” or simply an “event”, can refer to one or more of the following: a) detection of an area of relatively greater absorption (indicative of the likely presence of red blood cells) adjacent to an area of relatively lower absorption compared to the first area (indicative of the likely presence of one or more white blood cells) within a capillary; b) detection of a first area of relatively greater absorption (indicative of the likely presence of red blood cells) adjacent to a second area of relatively lower absorption compared to the first area (indicative of the likely presence of one or more white blood cells downstream of the first area), where the second area is adjacent to a third area of differing absorption than that of the second area (indicative of either the likely presence of red blood cells downstream of the second area, or of an area substantially devoid of any cells) within a capillary.

(197) It is understood that while disclosed herein for detection of white blood cells in capillaries, aspects of this disclosure are useful for detecting any other suitable cells as long as those cells exhibit a contrast in absorption relative to red blood cells. As an example, circulating tumor cells (CTCs) may be detectable by selecting capillaries (i.e., by selecting the first set of capillaries or the second set of capillaries) having a diameter similar to that of CTCs. As another example, one or more white blood cell types (e.g., neutrophils, lymphocytes, monocytes, eosinophils, and/or basophils) may be detectable by suitable capillary selection as described herein.

(198) In some embodiments, for every capillary of the second set of capillaries, the controller **2350** detects one or more cellular events that flow through that capillary as follows. In some embodiments, the controller **2350** loads all the images showing the capillary as a 3D matrix into the memory **2360** and/or the database **2370**, with matrix dimensions associated with to the x pixel location, the y pixel location, and the image. Every matrix value corresponds to a brightness level for that pixel. In some embodiments, the controller normalizes the brightness level of the 3D matrix by a) normalizing the brightness level spatially with respect to the first image showing that capillary to compensate for potential brightness variations associated with the illumination source **2320**. In some embodiments, this is accomplished by a) flattening individual images by dividing (for each pixel) the pixel brightness by local brightness averages estimated with a Gaussian filter with a standard deviation of 25 pixels, and b) adjusting the average brightness of every image showing that capillary such that brightness values remain closest to those in the first image showing that capillary (in terms of mean-squared error).

(199) Each pixel in this preprocessed, normalized 3D matrix has a time-signal associated with it that will be similar for all pixels under which the same cellular event passes; the main difference between these pixels will be a pixel specific time shift. Another difference is that not all time signals are equally strong/of adequate amplitude. As a first approximation, the controller **2350** chooses a pixel away from the edge of the image with the ‘strongest’ time-signal to be a reference pixel. Generally, a strong/desirable signal is one having a large contrast between the bright gaps (indicative of likely presence of a white blood cell) and the dark red blood cells such as, for example, a contrast that exceeds the noise level in the signal by a predetermined threshold. This signal can be a candidate reference signal for temporal alignment. In some embodiments, the controller estimates the strength of this candidate reference signal based on the ratio between the sum of its squared values and the sum of its absolute values; this ratio can be interpreted as an estimation of the strength of its peaks relative to its nominal fluctuations. In some embodiments, the reference signal estimation can employ the following pre- and post-normalization steps: (a) local temporal averages are subtracted from the time signals based on an averaging window (e.g., a

window size of 200 ms), (b) for robustness, the aforementioned ratio is estimated as the median of 10 estimates from 10 successive time chunks of same size, (c) the resulting ratio estimates, which form a 2D map for the set of images showing the capillary, are further filtered spatially (across the spatial dimensions) with a Gaussian filter with standard deviation of 1 pixel. In some embodiments, the controller **2350** ignores and/or does not otherwise account for other capillaries near the edge of the region-of-interest, as there may be intensity fluctuations due to imperfect registration, by introducing a weighting factor to penalize reference-pixel candidates that are near the border of the frame. The controller **2350** then chooses the pixel that maximizes the product of the peak intensity of the preprocessed time-signal and its distance from the edge of the region of interest.

(200) In some embodiments, the controller **2350** further filters out other structures that are not likely to be a cellular event through spatial filtering of every separate frame. In some embodiments, this is accomplished by, for every frame, applying a band-pass filter in the discrete Fourier domain to remove all features of unsuitable size, the low-frequency and high-frequency band-pass parameters being adjusted to fit the range of expected cellular event sizes/expected white blood cell size.

(201) In some embodiments, the controller **2350** further sets the intensity of a red-blood-cell-filled capillary to zero. The goal of this step is to ensure that flow without events will display proper contrast with respect to the passage of events, the latter being then ideally associated with (significant) non-zero brightness values after bias removal. In some embodiments, the controller accomplishes this by subtracting the temporal (frame-wise) medians from all corresponding pixels in all images showing that capillary. The pixel-wise operation is performed on all pixels separately and indiscriminately, i.e., independently of whether the pixels are inside or outside a capillary. An assumption of this step is that a capillary is filled with red blood cells for most of its length, and for most of the time.

(202) The controller **2350** then compares the time-signal that is associated with every pixel location of the images showing the capillary of the second set of capillaries to the reference time signal at the reference pixel, that was estimated as disclosed herein. First, the controller **2350** suppresses long-term intensity fluctuations by applying a high-pass filter to every separate time signal along the time dimension. The controller **2350** then estimates the correlation between every time signal and the reference time signal, which results in an amplitude and a phase value for each pixel. A large positive amplitude indicates a strong correlation, and the phase indicates the time shift with respect to the signal at the reference pixel. This per-pixel amplitude and phase information is used as described below to estimate an averaged signal that is more robust to noise. The controller **2350** performs all operations by replicating the first and last frame to avoid false detections at the start or end of the sequence of images showing the capillary.

(203) Based on the reference time signal and on the other times signals with associated phase and amplitude correlation information, the controller **2350** generates an averaged time signal that is relatively more robust to noise. This averaged time signal combines all time signals that are deemed to be part of the capillary. In some embodiments, the controller **2350** retains any time signals where a) their correlation with the reference signal exceed the reference-signal autocorrelation times a threshold value, and b) the time signal's (positive or negative) time delay with respect to the reference signal (i.e., the phase) is no larger than the maximum time that a gap/cellular event takes to flow through the capillary, which is a relatively fixed parameter.

(204) The controller **2350** then calculates a superior reference time signal as follows: (a) all time signals are aligned in time with respect to the reference time signal, based on the phase information, (b) the aligned time signals are averaged, (c) the resulting averaged signal is high-pass-filtered in time, based on a fixed minimum-frequency parameter. The resulting filtered one-dimensional signal is useful for detection of cellular events, noting that the time at which cellular events are detected is associated with the reference pixel position. FIGS. 26A-C illustrates an example of a real time signal produced by analyzing a set of images for one capillary, and also

shows the types of time-signal profiles that can be expected around a single cellular event versus a plasma gap. It is hypothesized that gaps containing a white blood cell have a higher concentration of red blood cells, corresponding to a darker area, upstream, as best illustrated in FIG. 26B.

(205) Each gap/cellular event is associated with an uninterrupted stream of values for which the averaged time signal, which reflects the spatially averaged normalized brightness in the capillary, exceeds a threshold value. While all non-zero values should reflect a passing event, due to noise, the threshold value can be set as a non-zero, positive value. In some embodiments, the threshold value is optimized to achieve the best possible separation between the signal and the noise. For example, in some embodiments, the threshold value is set to capture most peak signal information (associated with values above that threshold) while rejecting most noise artefacts (associated with values below that threshold). In some embodiments, the controller 2350 sets this threshold value as a multiple of the noise's standard deviation, where the noise is estimated following a positive exponential model (i.e., a decaying exponential is fitted to the positive part of the signal distribution). In some embodiments, the standard deviation of the signal itself can serve as a noise estimate. In some embodiments, before thresholding, the controller checks the averaged time signal to avoid repeated spurious event detections: specifically, if the ratio between the median-filtered version of the signal (e.g., with filter size of 240 frames) and the first-quartile thereof exceeds unity, the controller locally divides the signal by this ratio. For each detected gap/cellular event, associated time information is defined with respect to the reference pixel; if the signal exceeds the threshold for more than one image showing that capillary, the controller chooses the center image in the series of images showing that capillary.

(206) In some embodiments, the controller maps the cellular events back to a series of x, y, and t in the 3D matrix, maximum one per image for that capillary. Each cellular event can occur in multiple images, a number that depends on the flow speed, capillary length, and the frame rate of the acquisition. The ability to detect a cellular event is limited by the maximum crossing time of a gap around the reference frame, the frame in which the gap passed the reference pixel. For each image, controller 2350 marks the brightest pixel that is deemed to be inside the capillary.

(207) For each capillary of the second set of capillaries, the controller 2350 then generates an associated event count. As described in more detail herein, in some embodiments, after averaging the event count across all capillaries in the second set of capillaries, each set of images can be used for classification of the user.

(208) FIGS. 27A-27B illustrate results from cellular event detection on 26 raw videos/sets of images, with comparison to human raters. Comparing against one of the individual raters, F1 score is used as a metric measuring the consistency of the detected events (defined as the harmonic mean of precision P and recall R, where  $P = TP / (TP + FP)$  and  $R = TP / (TP + FN)$ ). For individual experts (3 in total), the F1 score was evaluated against the cellular events consistently detected by the rest of experts (i.e., groups of 2). For the embodiments disclosed herein, the F1 score was evaluated as an average between the results with respect to these 3 groups of 2 experts, which ensured an unbiased comparison. The F1 score takes true positives, false positives, and false negatives into account.

(209) FIGS. 28A-28D illustrate an example, overall approach to cellular event detection as described herein with respect to the controller 2350.

(210) Referring again to FIG. 23, in some embodiments, the controller 2350, based on the number of cellular events detected in the second set of capillaries, classifies the user to a user type of a set of user types. In some embodiments, at least one of the user types is associated with a diagnosis of neutropenia (absolute neutrophil count <500 cells/ul), and at least one other user type is associated with the user not being neutropenic. In some embodiments, the controller 2350 executes a weighting approach (i.e., employing a weighted average of event count across all capillaries) to improve classification quality. In some embodiments, the weighting approach can be based on the estimated quality of the set of images.

(211) In some embodiments, the controller 2350 generates a single event index value (also

sometimes referred to as a “Leuko-index value”) summarizing all event counts. In some embodiments, the controller compares the event index value against an event threshold, that can (in some embodiments) be a learned parameter, as described in more detail herein. The classification of the user to a user type (e.g., a first user type) associated with severe neutropenia is if the event index value  $< \mu$ , and to another user type (e.g., a second user type). While described herein for two user types, it is understood that the controller **2350** can classify the user to three, four, or more user types, depending on the thresholding parameter(s).

(212) As noted herein, the controller **2350** can assign weights to each capillary of the second set of capillaries based on the estimated quality of that capillary. As an example, in some embodiments, the weight for a capillary can be set to 1/10 if the threshold used to detect events was greater than a fixed level relative to the standard deviation of the signal (which indicated a lower quality) and to 1 otherwise.

(213) As noted above, in some embodiments, the event threshold can be a learned parameter. For example, in some embodiments, the event threshold was determined based on a total of 116 raw videos/sets of images. Specifically, a total of 116 imaging sessions (mostly associated with 1 raw video/set of images each) from 42 patients were employed. From these sessions, 60 corresponded to a reference blood-draw value of  $ANC < 500$  and 56 to  $ANC > 500$  (15 of which to  $500 < ANC < 1,500$ ). In cases where consecutive daily blood draws showed a transition from  $ANC < 500$  to  $ANC > 500$ , the imaging session took place within 8 hours of the first one.

(214) FIGS. **29A-29B** shows results from classification of the aforementioned data using the systems, devices, and methods disclosed herein. A performance of 9% of false alarms (i.e., 9% of cases wrongly deemed severely neutropenic) under a 96% rate of detected severe neutropenia ( $AUC=0.96$ ) was obtained. In these results, 20% of sessions were deemed unsuitable during analysis and were thus discarded. The corresponding conditions are: (a) no session with  $< 3$  detected capillaries, (b) no session with zero Leuko index: individual capillaries (i.e., individual capillaries with no detected events) being also discarded as part of (b). FIGS. **61A-61B** illustrates how classification can be affected by the length of the video/number of images in the set of images employed.

(215) FIG. **30** illustrates a method **3000** for non-invasive hematological measurements, according to some embodiments. The method **3000** can be carried out by the system **2300**, or a structurally and/or functionally similar variant thereof. The method **3000** includes, at **3100**, acquiring a set of images of at least a nailfold portion of a finger of a user. In some embodiments, step **3100** further includes acquiring the set of images as a set of frames of a video. In some embodiments, the method **3000** further includes illuminating the nailfold portion, the acquiring the set of images being in response to the illumination of the nailfold portion.

(216) The method **3000** further includes, at **3200**, detecting, in each image of the set of images, one or more capillaries in the nailfold portion of the finger to identify a first set of capillaries across the set of images. The detecting can include estimating one or more attributes of each capillary of the first set of capillaries. The one or more attributes includes one or more structural attributes, one or more flow attributes, one or more imaging attributes, or combinations thereof, such that a first attribute of the one or more attributes of each capillary of the first set of capillaries meets a predetermined criterion for the first attribute. In some embodiments, the one or more structural attributes selected from the group consisting of average capillary diameter, lateral capillary diameter, vertical capillary diameter, capillary length, capillary shape, and/or the like. In some embodiments, the one or more flow attributes is selected from the group consisting of blood flow speed in the capillary, transit time for a cell within the visible portion of the capillary, volumetric flow rate, mass flow rate, and/or the like. In some embodiments, the one or more imaging attributes selected from the group consisting of contrast, focus, signal-to-noise ratio, image stability, and/or the like. In some embodiments, the first attribute is average capillary diameter, wherein each capillary of the second set of capillaries has an estimated average capillary diameter from about 10

μm to about 20 μm.

(217) In some embodiments, the method **3000** can further include generating a confidence value associated with the image of each capillary of the first set of capillaries in the set of images. The first set of capillaries can include those capillaries for which the confidence value, for each image in which that capillary is detected, exceeds a confidence threshold.

(218) In some embodiments, the method **3000** can further include receiving a set of training images including a specification of one or more capillaries visible within each image of the set of training images. The method **3000** can further include training a neural network on the set of training images, and applying the set of images to the neural network to detect the first set of capillaries.

(219) In some embodiments, the detecting the first set of capillaries further including applying the set of images to a neural network, the neural network being trained on a set of training images including a specification of one or more capillaries visible within each image of the set of training images.

(220) The method **3000** further includes, at **3300**, identifying a second set of capillaries from the first set of capillaries such that each capillary of the second set of capillaries is visible in a predetermined number of images of the set of images.

(221) In some embodiments, the method **3000** further includes detecting, for the set of images and in the second set of capillaries, a set of cellular events. Each cellular event of the set of cellular events is associated with passage of a white blood cell in a capillary of the second set of capillaries. The method **3000** can further include estimating an event count for the second set of capillaries based on the set of cellular events.

(222) In some embodiments, the method **3000** further includes, for each capillary of the second set of capillaries, estimating a quality factor. The method **3000** can further include estimating the event count based on the set of cellular events and the quality factor associated with each capillary of the second set of capillaries.

(223) In some embodiments, the method **3000** further includes receiving a set of training images associated with nailfold portions of a set of training users. The method **3000** can further include generating, via supervised learning, an event count threshold based on the set of training images. The method **3000** can further include classifying the user to a first user type of a set of user types based on the event count and the event count threshold, at least one user type of the set of user types associated with a diagnosis of neutropenia. The method **3000** can further include transmitting an indication of the first user type to the user (e.g., via an interface of the system **2300**, of the device **2340**).

(224) Additional detail on various embodiments of the systems, devices, and methods as laid out herein are provided below.

(225) Volumetric Estimation and Capillary Sub-Selection for Improved Accuracy of Counts

(226) As described above (e.g., with reference to Equation (8)), the WBC concentration can be estimated based on the estimation of the number of WBC cells (e.g., as estimated by the number of cellular events) and the volume of blood passing through the capillary of interest during the total video-acquisition time. The total blood volume passing through a given capillary section usually depends on the local diameter of the capillary section and the average local speed of the blood. In addition, the conservation of volume (or conservation of the mass of the blood) indicates that the total blood volume of interest can be maintained at a constant value during propagating within the capillary. In other words, the total blood volume can be a constant independent of the capillary section that is considered. Therefore, the estimation of the volume of a capillary section can be employed as an estimation of the blood volume of interest.

(227) Based on this observation, a method of robust volumetric estimation is based on cross-correlation or optical flow techniques.

(228) At least two approaches can be used to estimate the volume of a capillary section. In one approach, it can be assumed that the capillary section at issue has a perfectly cylindrical shape. In

this case, the width of the capillary, as acquired from the video or image, can be used also as the depth of the capillary.

(229) In another approach, a method of estimating the volume of a capillary section is performed based on the analysis of pixel-intensity values. Specifically, the capillary depth at a given position in the image plane is expected to inversely correlate with the measured light intensity due to light absorption. The vertical and horizontal diameter of the capillary may not be equal, meaning that diameter of the visible projection may not be representative of the vertical diameter. In other words, a lower pixel value indicates a larger value of capillary depth and vice versa. Accordingly, this resolved depth estimation can be used to more accurately compute the cross sectional area of the capillary section.

(230) FIGS. **31A-31F** illustrate a method of estimating the volume of a capillary section based on analysis of pixel intensities. In some embodiment, some or all aspects of the method of FIGS. **31A-31F** can be executed by one or more of the systems, apparatuses, and devices as described herein such as, for example, the system **2300** and/or the device **2340**.

(231) FIGS. **31A** and **31B** show two images of capillary sections, where the pixel value in FIG. **31A** is greater than the pixel value in FIG. **31B** (i.e. FIG. **31A** is brighter). The two capillary sections have the same width of about 15  $\mu\text{m}$  at a given location indicated in FIGS. **31A** and **31B**. In conventional methods, this width is also used as the depth of the capillary sections and the reconstructed capillary cross sections are perfectly round, as shown in FIGS. **31C** and **31D**. In contrast, when the pixel intensities are taken into account, the different pixel values indicate that the depths of the two capillary sections are different. FIGS. **31E** and **31F** show the reconstructed cross sections corresponding to the capillary sections shown in FIGS. **31A** and **31B**, respectively, using the method based on pixel intensity analysis. As seen from FIGS. **31E** and **31F**, the larger pixel value in FIG. **31A** indicates a smaller depth, while the lower pixel value in FIG. **31B** indicates a greater depth. The cross sectional shapes of the two capillary sections are now elliptical instead of being circular.

(232) The same analysis can be performed along the entire capillary shown in FIGS. **31A** and **31B** and a cross sectional area  $A$  as a function of the curvilinear coordinate (e.g., length  $l$ ) can be acquired. The total volume of the capillary  $V$  can then be calculated by taking the integral of  $A(l)$  with respect to  $l$ , i.e.,  $V = \int A(l) dl$ .

(233) The volume calculated from the above method can also be used for volume resampling of the capillary profile. This method can analyze the flow speed in one given capillary using a one-dimensional curvilinear coordinate system. In one example, coordinates in a one-dimensional curvilinear coordinate system are usually a function of length along the capillary (see, e.g., FIGS. **6A** and **6B** and descriptions above). In another example, the coordinates in a one-dimensional curvilinear coordinate system can be a function of the cumulative capillary volume. One advantage of resampling coordinates according to the cumulative capillary volume is that the particle/event speed can become constant in the particular coordinate system, thereby facilitating accurate estimation using cross-correlation or similar techniques.

(234) FIGS. **32A-32C** illustrate volume resampling of a capillary profile. FIG. **32A** shows a representation of a capillary having a constant blood flow speed but varying diameters along the capillary length. Due to light absorption, red blood cells are represented in black whereas a single white blood cell squeezing through the capillary is represented in white. FIG. **32B** shows a spatio-temporal map representing the gray-scale values (color map from blue—dark—to red—bright—) along the linear capillary length (y-axis) across time (x-axis). FIG. **32C** shows a spatio-temporal map acquired using volume resampling and the map is shown with the capillary length coordinates (y-axis) as a function of the cumulative capillary volume at each cross-section in FIG. **32A**. In this case, the white blood cell trajectory (red—bright—line) at constant speeds becomes a straight line thus being easier and more accurate to estimate using cross-correlation or similar techniques.

(235) Sub-Selection of Capillary Events

(236) Further improvement of WBC detection and estimation (e.g., as generally described herein with respect to FIGS. **23-30**) can be achieved via sub-selection of capillaries whose events are most easily detectable and most likely to correlate with the presence of WBCs. The sub-selection of capillary events can be carried out according to several criterions.

(237) In one example, the sub-selection can be according to the observed size, i.e., average diameter and/or diameter profile. The size usually correlates with the presence of clear, high-contrast, and whole-capillary-diameter events for a given range, such as the range between about 10  $\mu\text{m}$  and about 20  $\mu\text{m}$ ). FIG. **33** shows the range of capillary diameters with the presence of clear gaps. Sub-selecting capillaries based on their diameter can improve correlation with WBCs.

(238) In another example, the sub-selection can be according to the temporal distribution in the arrival of clear, high-contrast, and whole-capillary-diameter events, which are showed to be different in the presence/absence of white blood cells. FIG. **34A** shows the distribution of the time of arrival (TOA) between gaps in a sample with 5,500 WBC/ $\mu\text{L}$ . With this high concentration of WBC, the TOA substantially follows a Poisson distribution. In contrast, FIG. **34B** shows the distribution of TOA between gaps in a sample with 100 WBC/ $\mu\text{L}$ , much lower than the concentration shown in FIG. **34A**.

(239) In yet another example, the sub-selection can be performed according to the dynamical behavior of the capillaries. In this approach, a method can directly sub-select capillaries based on the event features, including length, contrast-to-noise ratio, and speed. For example, clogging effects can be identified as being due to red blood cells in some small-diameter capillaries.

(240) Acquisition of High-Speed, High-Contrast, and Stable Videos of Multiple Nailfold Capillaries

(241) FIGS. **35A-35C** illustrate an apparatus for detecting severe neutropenia based on images of nailfold capillaries. In some embodiment, some or all aspects of the apparatus of FIGS. **35A-35C** can be structurally and/or functionally similar to one or more of the systems, apparatuses, and devices as described herein such as, for example, the system **2300** and/or the device **2340**.

(242) FIG. **35A** shows a rendered 3D model of the apparatus employed to record microscopy videos of the microcirculation in nailfold capillaries of patients, with its different components. FIG. **35B** illustrates that patients place their ring finger in a 3D-printed holder, which plays a dual role: achieving stability throughout the one-minute recording duration and holding the oil employed for optical coupling. FIG. **35C** shows that the finger is placed in such a way that illumination and imaging is directed at the nailfold area (purple circled area as indicated in the figure).

(243) The apparatus shown in FIG. **35A** can be used to record high-quality microscopy videos of the microcirculation in human nailfold capillaries, and employed it on ASCT patients (see, FIG. **36**). The patient's finger is inserted from the top into the well of a 3D-printed semi-spherical easily-sanitized hand rest (FIG. **35B**), which is designed to ergonomically hold the patient's hand with sufficient stability to record one-minute videos. Capillary videos are acquired from the nailfold region in the finger of a subject (FIG. **35C**).

(244) FIGS. **37A** and **37B** show examples of raw images acquired by the apparatus shown in FIG. **35A**. The pair of wide-field videos was acquired with the apparatus from one ASCT patient at two time points where the same capillaries can be observed (three numbered pairs shown). FIG. **37A** shows the image taken with baseline neutrophil concentration (i.e., greater than 1,500/ $\mu\text{L}$ ) and FIG. **37B** shows the image taken with when the patient had severe neutropenia (neutrophils concentration less than 500/ $\mu\text{L}$ ). The scale bar in the images is 100  $\mu\text{m}$ .

(245) It can be seen from FIGS. **37A** and **37B** that the apparatus can optically capture capillary-nailfold videos with appropriate contrast, resolution, stability, and depth of focus. Raw videos acquired with the apparatus contain multiple capillaries within the field of view. The acquisition of several capillaries was made particularly convenient with this simple optical approach which allowed imaging of multiple capillaries at a time in the same field of view. In contrast, many existing techniques, such as encoded confocal microscopy (SECM), can only image a single

capillary at one time.

(246) FIGS. **38A-38E** illustrate an example of optical gap flowing in a capillary. The image sequence shows several raw frames of a video centered on one capillary acquired with the apparatus on one of the patients at baseline. The dark loop corresponds to the capillary vessel filled with RBCs that absorb light at the illumination wavelength. An optical absorption gap in the microcirculation, approximately the same size as the capillary width (about 15  $\mu\text{m}$ ) can be observed flowing through the arterial limb of the capillary (indicated as black arrowheads). Frame numbers are labeled at the top right corner. The frame rate was 60 frames per second and the exposure time was 16.7 ms. The contrast was adjusted for the region of interest shown.

(247) These capillaries in the acquired images are very narrow, with typical widths of about  $m$  to about 20  $\mu\text{m}$ . In this case, the WBCs are typically forced to squeeze through the capillaries one by one. Focusing in on a single capillary, the frames reveal the passage of an event in the microcirculation, which can be perceived as a moving “bright” object, approximately of the same size as the capillary diameter (about 15  $\mu\text{m}$ ). The bright object (or a gap in the dark background) has a brightness that is significantly higher than the surrounding RBCs and therefore can be readily observed and monitored.

(248) The event movement can be clearly followed across successive frames and, as such, are visually identifiable by a human observer. Accordingly, all events in the capillary videos were marked and labeled by three blinded human raters, following specific visual criteria (see more details below). Spatio-temporal (ST) maps provide a convenient alternative representation for showing all event trajectories with the marks from these raters in the one-minute capillary videos.

(249) FIGS. **39A-39E** show results of blind event rating using the images acquired by the apparatus shown in FIG. **35A**. Three human raters independently labeled one event they observed in one of the 98 capillaries employed in the study. FIGS. **39A-39C** show capillary-video frames (indexed at top right) with cross-shaped event marks from rater **1** (blue), **2** (green) and **3** (yellow). FIG. **39D** shows aggregated positions of all event marks from all three raters.

(250) FIG. **39E** shows an ST map displaying the recorded brightness levels along the segmented capillary length (vertical axis) as a function of time (horizontal axis) for a 1.7-second interval around the event of interest. A bright trajectory created by the passage of the event can be clearly identified in the center of the ST map. Blue, green, and yellow crosses correspond to the spatio-temporal coordinates where each of the three raters labeled the event. Event trajectories visible on the ST map correspond well with events identified by the raters from the videos.

(251) Microcirculation Events with Specific Features can be Used as Proxies of WBC

(252) FIG. **36** illustrates two different timing points to acquire images from patients in the clinical study. The patients enrolled in the study are undergoing an ASCT, process that results in a very predictable evolution of their neutrophil counts due to the controlled administration of chemotherapy. This provides an opportunity to record capillary videos at two different time points for each patient: (1) baseline ( $>1,500$  neutrophils/ $\mu\text{L}$ ) and (2) severe neutropenia ( $<500$  neutrophils/ $\mu\text{L}$ ).

(253) The acquired video images were analyzed at the two different time points shown in FIG. **36** in **10** ASCT patients undergoing chemotherapy: pre-chemotherapy ( $>1,500$  neutrophils per  $\mu\text{L}$ ; baseline) and during severe neutropenia ( $<500$  neutrophils per  $\mu\text{L}$ ). The same sets of capillaries were acquired at baseline and during severe neutropenia for every patient to minimize the amount of potential confounding factors as well as selection bias (see more details below). Acquiring one-minute videos can overcome the shot noise associated with the discrete nature of the events.

(254) In these videos, the consistency with which events were identified in the capillary microcirculation by the three raters depended on whether capillary videos were acquired at baseline or during severe neutropenia. In instances where raters identified and counted events in capillary videos acquired during baseline, 67% of those events were validated (i.e., two or more raters identified the same event). In instances of capillary videos acquired during severe neutropenia, only



22% of events were validated. The visual features of rated events tended to be more consistent in baseline cases (see FIGS. **48A** and **48B** below)

(255) These results suggested that events with consistently detectable visual features correlate with the presence of WBC and neutrophils. The validated-event counts were therefore treated as proxies to WBC counts. The fact that most validated events happened in capillary sections comparable to the size of a WBC (see FIG. **47**) also corroborates findings from previous literature, which relate observed gaps to combinations of WBCs and plasma flowing through the capillary.

(256) Non-Invasive Detection of Severe Neutropenia

(257) White-blood-cell (WBC) count can be used as one indicator of immunological status in the diagnosis and treatment of multiple medical conditions, including cancer, infectious diseases, sepsis, and autoimmune disorders. WBC count is also used in immunosuppressant drugs. However, current methods of WBC counting usually involves personal visits to healthcare centers for phlebotomy performed by trained clinical personnel, even with finger-prick technologies. This limitation restricts both frequency and time duration of the monitoring. In addition, traditional blood testing typically uses specific reagents and sterile conditions, which may preclude applicability in resource-limited environments. In contrast, a non-invasive approach to WBC measurement can circumvent many of these requirements, drawing parallels to existing non-invasive technologies for the monitoring of blood oxygen saturation levels.

(258) One step towards non-invasive WBC analysis includes non-invasive screening for severe neutropenia, which can be defined as low levels of neutrophils (e.g., less than 500 per p L)—a common type of WBC. This condition is one of the main toxicities in patients receiving common chemotherapy regimens. It is responsible for a significant amount of morbidity and a significant risk of mortality because of its associated increased risk of infection. However, the monitoring of severe neutropenia is currently insufficient for the aforementioned reasons. This barrier to rapid clinical care interferes with the timely life-saving interventions of prophylactic antibiotics or growth colony stimulating factors in afebrile patients with prolonged severe neutropenia. In that regard, a non-invasive method can substantially impact the outpatient care and management of patients at high risk for severe neutropenia-related immunosuppression.

(259) Systems, apparatus, and methods described herein can provide a screening tool for severe neutropenia based on non-invasive and portable optical visualization of capillaries. When capillary diameter approaches WBC diameter (e.g., about 10  $\mu\text{m}$  to about 20  $\mu\text{m}$ ), the WBC can completely fill the capillary lumen. This typically causes a red-blood-cell (RBC) depletion downstream of the WBC in the microcirculation where WBCs flow with a lower velocity than the velocity of the RBCs. In this situation, proper illumination (e.g., at specific wavelengths) can render WBCs transparent and RBCs dark, and the passage of a WBC can appear as an optical absorption gap in the continuous RBC stream that moves through the capillary.

(260) Using white-light trans-illumination microscopy, this “gap” phenomenon can be observed in a rabbit ear window model. The results explicitly showed RBCs accumulating upstream of WBCs with a RBC-depleted area downstream when the capillary and WBC were of comparable diameters. The same phenomenon was also observed in rat-cremaster and bat-wing microcirculation, using blue-light transillumination to maximize contrast between RBCs—peak absorption for oxy- and deoxyhemoglobin is blue at 420 nm—and low-absorption regions that lack RBCs. Observing the flow of RBCs over time revealed the capillary morphology, in which brighter regions associated with optical-absorption gaps inside the capillary lumen. Fluorescent labeling can also be used to confirm that gaps were associated with WBCs.

(261) The idea that such absorption gaps relate to WBCs was investigated in humans by taking advantage of the blue entoptic phenomenon, where WBCs transmit blue light through as they flow in front of the retina, thus creating bright spots that the subject can see. For example, subjects can have their eyes illuminated with blue light and were asked how many bright spots they perceived. Group differences in amounts of perceived spots between baseline, leukopenic, and leukocytotic

subjects-related to normal, abnormally low, and abnormally high ranges of WBC counts, respectively-were reported. One limitation of these methods, however, is their reliance on subject self-assessment. They are thus prone to individual biases and poor repeatability that do not make them amenable for clinical screening.

(262) Overall, these findings suggest that flowing gaps in capillaries could provide a basis for a new method to measure WBC counts non-invasively. Systems, apparatus, and methods described herein use nailfold capillaries that are superficial (e.g., about 50  $\mu\text{m}$  to about 100  $\mu\text{m}$  deep), have diameters comparable to WBC size, and run substantially parallel to the skin surface, and can thus be visualized non-invasively with simple, affordable optical equipment.

(263) In this technique, optical imaging is used to screen for severe neutropenia in human subjects by counting events defined as instances of moving optical absorption gaps in the nailfold microcirculation. To do so, a portable apparatus is constructed to produce optical microscopy videos of capillaries (see, e.g., FIGS. 35A-35C). The technique can maximize RBC to non-RBC contrast over multiple capillaries within one field of view while ensuring adequate resolution, depth of focus, stability, and frame rate. Based on this apparatus, a clinical study was conducted (see, e.g., FIG. 34) involving 10 patients undergoing high-dose chemotherapy and autologous stem-cell transplantation (ASCT) given the predictability of their neutrophil nadir and recovery kinetics. For each patient, one-minute videos of the same capillary set were acquired with the apparatus at two time points: pre-chemotherapy baseline (about 1,500 neutrophils per  $\mu\text{L}$ ) and severe neutropenia (about 500 neutrophils per  $\mu\text{L}$ ) (see, e.g., FIGS. 29A and 29B). Based on these data, a method can be developed and validated to tag event counts (see, FIGS. 38A-39D) and to discriminate between baseline and severe neutropenia across all patients (see, e.g., FIGS. 40 and 41).

(264) The Baseline State can be Classified from the Severe-Neutropenic State Non-Invasively

(265) FIG. 40 shows the number of validated events per minute in all studied capillary pairs. Values at baseline (blue dots) showed a statistically significant difference when compared to their corresponding values at severe neutropenia (red squares). Only validated events are considered in order to maximize the objectivity of the event selection and discard noise. All capillaries were analyzed both at baseline and severe neutropenia (98 pairs in total; black dotted lines).

(266) The number of validated-event counts in a capillary imaged during severe neutropenia was consistently less than the counts in the same capillary imaged during baseline as seen in FIG. 40. Specifically, the paired capillary counts showed a highly statistically significant difference ( $P < 10^{-8}$ ; Wilcoxon signed-rank test) between baseline and severe neutropenia. Counts from distinct capillaries tended to vary across the same patient, sometimes reaching low values even at baseline. Such variations may be associated with several factors, which motivated the aggregation of counts from several capillaries for every patient (see more details below).

(267) FIG. 41 shows the discrimination between baseline and severe neutropenia. The median number of validated events observed per minute, when aggregating all available capillaries per patient, allows discriminating between baseline (blue dots) and severe neutropenia (red dots) for the 20 acquired videos and 10 patients of the study. The corresponding cross-capillary variability is also shown for each patient (blue and red bars). The optimal threshold to separate baseline from severe neutropenia is seven events per capillary minute (dotted black line). The X-axis is labeled with the patient IDs together with their amount of analyzed capillaries (brackets). The median amount of capillaries used per patient was four.

(268) The distinction between the neutropenic and baseline states is also apparent when aggregating the data across all the capillaries from a given patient at a given time (FIG. 41); the results showed a statistically significant difference ( $P = 0.002$ ; Wilcoxon signed-rank test) between baseline and severe neutropenia. Furthermore, in this capillary-aggregated case, the distribution of validated-event counts at baseline does not overlap the distribution when severely neutropenic. Indeed, at a threshold of 7 counts, the median count for capillaries in a given patient could correctly classify 9 of 10 neutropenic cases. The two or three first added capillaries accounted for most gain

in classification performance (see FIGS. 44A and 44B).

(269) The above study demonstrated that severe neutropenia can be detected non-invasively in humans based on optical imaging. It also validates the overall classification strategy as a proof of principle involving the optical apparatus, experimental protocol, and data-analysis techniques.

(270) By design, the clinical study involved baseline absolute neutrophil counts (ANCs) ( $>1,500$  neutrophils/ $\mu\text{L}$ ) and severe neutropenia ( $<500$  neutrophils/ $\mu\text{L}$ ) in the same patients. While the classification approach was not assessed in the mild (grade II,  $<1,500$  neutrophils/ $\mu\text{L}$ ) and moderate (grade III,  $<1,000$  neutrophils/ $\mu\text{L}$ ) neutropenia cases, the current results can be extrapolated to these additional ranges assuming that average event counts vary accordingly. This may involve additional clinical studies with more representative data throughout the different grades of neutropenia. Meanwhile, the event counts obtained for each patient in the study (shown in FIG. 41) are consistent with the corresponding reference cell concentrations shown in Table 1 below.

(271) TABLE-US-00001 TABLE 1 Reference values obtained from hospital clinical laboratory.

Patient	Leukocytes (cells/ul)	Neutrophils (cells/ul)	ID	Baseline	Severe N.	Baseline	Severe N.
01	5500	100	4060	10	02	2000	300
1280	10	03	5860	210	5660	0	04
4290	40	2830	20	05	2530	20	1950
10	06	2930	100	1840	30	07	7430
90	7100	0	08	6370	50	6040	0
09	3180	40	2770	10	10	5350	120
3700	0						

(272) Specifically, assuming an average blood-flow speed of  $800 \mu\text{m/s}$  and an average capillary diameter of  $15 \mu\text{m}$ , the median values of the aggregated patient counts for baseline and severe neutropenia, i.e., 31.73 and 1.96, yield WBC-concentration estimates of about 3,700 and 200 cells/ $\mu\text{L}$ . Both estimates fall within the ranges of the corresponding references from the gold standard laboratory assays (Table 1).

(273) The event rating can be performed automatically on the input capillary videos. Such an algorithm can follow approaches used for detecting objects moving through capillaries or more advanced strategies, such as machine learning techniques. Several event features, such as contrast, size, or persistence, can be employed. Besides the mere counts, the algorithmic estimation of capillary blood flow may improve the precision and accuracy of the results by providing estimates that are physically consistent with WBC concentrations.

(274) Further improvements on the apparatus can increase the amounts of capillaries per patient that satisfy the quality and consistency criteria required for further analysis. This can be useful for a future translation of this technology to clinical practice. The constraint of following the same capillaries for the same patients may be relaxed to ease the clinical applicability of the method.

(275) One extension to this study can be to investigate whether specific WBC ranges can be identified beyond screening for severe neutropenia. This can broaden the applicability of the technique described herein not only within the context of chemotherapy, but also to new settings, such as infectious diseases, while still following a similar conceptual approach. Non-invasive differential WBC counts may also be achieved based on similar techniques/data, knowing that distinct WBC types lead to distinct optical properties and image features, e.g., non-granular and granular WBC correspond to distinct event lengths and backscattering properties in a capillary.

(276) Overall, this study proved that chemotherapy-induced severe neutropenia can be detected non-invasively through the fingernail with an ad-hoc developed prototype. This study represents the first proof of concept for a technology that could measure an important toxicity of chemotherapy by optical means. The automatization, replication, and refinement of these results may lead to a new paradigm in the monitoring of cancer patients at risk of severe neutropenia. Furthermore, from a more general standpoint, the proposed imaging technique and conceptual approach could constitute one first step towards non-invasive, in-vivo WBC counting.

Example

(277) A pilot diagnostic validation study was conducted to test the a-priori hypothesis that the non-invasive technique allows the classification of severe neutropenia ( $<500$  neutrophils/ $\mu\text{L}$ ) versus the

baseline status ( $>1,500$  neutrophils/ $\mu\text{L}$ ) in patients. A cohort of patients who were undergoing high-dose chemotherapy followed by ASCT was enrolled. The kinetics of neutrophil counts in these patients is predictable because the intensity of the chemotherapy applied prior to transplantation ensures the passage through a severe-neutropenia stage followed by recovery. In the framework of this study, no power analysis was carried out and a convenience sample of 10 subjects (as selected from the initial patient pool) was considered sufficient to test the study hypothesis. Non-parametric tests were used as well as ROC curve analyses. All human raters who analyzed the data were blinded, as detailed below.

(278) In total, 23 patients were recruited, with 16 and 7 patients from the Massachusetts General Hospital, Boston, MA, USA, and Hospital Universitario La Paz, Madrid, Spain, respectively. Each recruited patient signed an informed consent. All the information obtained was anonymous and the participants were not identifiable.

(279) The patient inclusion criteria used for recruitment were the following: (a) patients must have a scheduled ASCT of hematopoietic progenitors; (b) patients must be 18 years or older; (c) patients must have the ability to understand and the willingness to sign a written consent document; (d) at baseline, patients must have a leukocyte count equal to or greater than 3,000 cells/ $\mu\text{L}$  and a neutrophil count equal to or greater than 1,500 cells/ $\mu\text{L}$ . Patients were excluded if suffering from myelodysplasia or from a history of allergic reactions to components of chemical compositions similar to the oil used for optical coupling in the clinical device, or if their skin phototype was larger than four in the Fitzpatrick scale.

(280) The MGH clinical study was approved by the Dana-Farber/Harvard Cancer Center (DFHCC) institutional review board, and by the MIT Committee on the Use of Humans as Experimental Subjects (COUHES) as COUHES Protocol #1610717680. This study was also registered at Clinicaltrials.gov. The La Paz clinical study was approved by the La Paz Ethics Committee in the document HULP PI-2353. The analysis of anonymized data from these pilot studies was also approved by the Ethics Committee of Universidad Politécnica de Madrid.

(281) Optical Apparatus

(282) One example configuration of the apparatus (shown in FIG. 35A) used for video acquisition in ASCT patients includes the following elements. This configuration is for illustrative purposes only and variations may be made by one of ordinary skill in the art. 1. Imaging objective. Edmund Optics TECHSPEC 5X. The optical features of this objective are a  $5\times$  magnification and a maximum numerical aperture of 0.15 reduced through the use of a 3D-printed iris of 2.5 mm diameter, which maximizes the depth of focus and imaging multiple capillaries simultaneously. The working distance is 16.2 mm, and the maximum field of view (FOV)  $1.8\times1.32$  mm. Its dimensions correspond to a 50 mm fixed tube length and a 93.81 mm total length. Its height, azimuth, and focal position are manually adjustable. 2. CMOS camera. Thorlabs DCC3240N. This CMOS camera is mounted to the objective and computer-powered through a USB connection. It comprises a global/rolling shutter. Its field of view (FOV) is  $1280\times1024$  pixels, or  $1360\times1088$   $\mu\text{m}$  at  $5\times$  magnification, corresponding to a pixel size of  $1.0625\times1.0625$   $\mu\text{m}$ . Its frame rate is about 60 frames per second (FPS) in full frame, thus ensuring enough temporal resolution to detect and track events given that the range of blood flow speeds in nailfold capillaries is 100-1,000  $\mu\text{m/s}$ . The frame rate can reach 229 FPS if restricted a FOV of  $320\times240$  pixels. Its bit depth is 10 bits per pixel monochrome. 3. Illuminators. Rapid prototyped LED holders, cage-mounted with heat sinks at angles of about 70 degrees from the detection axis were used. They include high-power Luxeon LEDs emitting light in deep blue, i.e., at 420 nm. This illumination wavelength allows to maximize the contrast between RBCs—which appear dark in the videos—and optical-absorption gaps. Each LED emits 161 Lumens at 700 mA, using an aspheric collection lens with  $F=20.1$  mm,  $NA=0.6$  and an adjustable collimation slit Thorlabs VA100C. 4. Power driver. Used to drive both LED illuminators continuously at constant DC power level. 5. Disposable hand rest. A 3D-printed and rigidly mounted platform used to hold the finger in a stable position for at least one-minute

imaging. This platform comprises a one-size-fits-all finger well. Optical-coupling oil (Johnson & Johnson, refractive index=1.51) remains in the finger well. 6. Laptop and software. A laptop connected to the CMOS camera was used for power and image acquisition. Specifically tailored LabView software was used for the acquisition and storage of the videos. The output data collected for every patient and acquisition session with this software consist of a set of uncompressed videos, and for each of the videos, the time stamps providing information on the exact acquisition times associated with each frame.

(283) As part of the clinical study, two units of this apparatus were mounted and employed at the Massachusetts General Hospital, Boston, MA, USA, and at La Paz, Madrid, Spain, respectively. Following every use of the apparatus on a patient, disinfectant wipes were employed on the system components. The use of this device was approved for clinical research as the DF/HCC protocol #15-070.

#### (284) Data Collection

(285) In the study, videos were acquired from the same sets capillaries at baseline and during severe neutropenia for every given patient. Tracking the same capillaries at both time points allowed avoiding potential biases in the capillary selection, and minimizing confounding factors, e.g., this was expected to minimize changes in capillary geometry between the baseline and severe-neutropenic time points, thus ensuring that changes in count values within one given capillary pair reflects the underlying change in WBC concentration most accurately.

(286) In order to obtain videos containing common capillaries in a given patient, the optical-prototype user located at least one capillary area similar to baseline during severe neutropenia. This process was performed manually during live data acquisition, which proved challenging in certain cases for logistical reasons. Meanwhile, the variety of capillary distributions and morphologies potentially allowed for the accurate identification of regions acquired previously in the baseline acquisition. In addition, the capillary-area-identification process was simplified by the fact that the nailfold capillaries of interest are selected near from the nail boundary; the capillary regions of interest were thus restricted accordingly.

(287) Out of the 23 recruited patients, 10 were deemed compliant with the quality criteria and eligible for further processing (see capillary selection). Specifically, six whole-patient datasets were excluded due to insufficient imaging quality, and four were excluded due to lack of correspondence between the capillaries studied in baseline and severe-neutropenic time points. For each of the 10 eligible patients, at least one pair of videos was selected, corresponding to the acquisitions of the same capillary area in both clinical states. This amounts to 20 raw-video datasets, with two distinct capillary regions acquired for Patients 01 and 02. In total, 49 distinct capillaries were selected to be followed and analyzed at baseline and during severe neutropenia.

(288) Videos were acquired within eight hours of a corresponding blood test that provides reference information. Specifically, in addition to the selected videos and capillaries, the WBC and ANC concentrations from the state-of-the-art blood-cell analytics were obtained for every patient together with their clinical state (see Table 1). The reference blood-analytics values from this table reveal the decrease in WBC and ANC concentrations between baseline and severe neutropenia.

#### (289) Pre-Processing Workflow

(290) FIG. 42 illustrates a pre-processing workflow in the clinical study. Given a raw video acquisition of a patient (top left), the set of capillaries of suitable quality is selected by two human experts (top right; green rectangles). For each selected capillary (top right; example identified by arrow), a motion-corrected video of the corresponding region of interest is then created (bottom right). The following step (bottom left) includes event labeling by three blinded human raters, which allows for subsequent analysis and event counting, aggregation, and visualization.

(291) Each raw input video of interest was processed according to the pre-processing workflow shown in FIG. 42. Following capillary selection, each of the capillary videos included in the study was cropped to the corresponding region of interest and registered with respect to a reference frame

in the sequence to correct for motion during acquisition. The motion-corrected videos were anonymized/shuffled and then used by blind experts to identify events, deriving event counts accordingly. The data with labeled events could then be visualized a posteriori. Details on these steps are provided below.

#### (292) Capillary Selection

(293) Given the raw videos acquired from one given patient, two human experts separately defined sets of suitable capillaries based on qualitative empirical a-priori criteria defined below. In order to avoid potential biases, only capillaries selected by both blinded raters were included in the study. Each expert individually selected the best capillaries in raw videos according to the following criteria: A. Illumination. Capillaries are visible with sufficient contrast to an observer. B. Focus. Detailed capillary structures/dynamics are visible and not blurred out. C. Flow. Blood flow exists to allow for potential events to be identified and counted. D. Stability. Capillaries fully remain within the field of view of the video in all frames. E. Visibility. No object (e.g., air bubbles) can occlude capillaries. F. Morphology. Capillaries exhibit clear arterial and venous limbs. G. Fulfillment of conditions A-F both in baseline and severe-neutropenia acquisitions.

(294) For every patient, each expert first followed this procedure for the baseline-state videos. The goal was to acquire paired capillary videos for every patient, the set of candidate capillaries in severe neutropenia being limited by the choices already made during baseline. Resulting capillary-video pairs—at least one per patient—are the ones complying with the above criteria in both baseline and severe neutropenia and according to both experts (see FIGS. 49-60).

#### (295) Creation of Capillary Videos

(296) Based on the raw video data and on the above capillary-selection procedure, individual capillary videos were created based on (a) the definition, on the first video frame, of rectangular regions of interest enclosing each of the capillaries of interest, followed by (b) video motion-compensation software, which locally compensates camera movements and ensures that the position of every capillary remains stable within the corresponding region of interest for the whole duration of the video. Note that all raw videos were first flattened, i.e., their local brightness was normalized through Gaussian filtering to remove potential effects of non-uniform illumination.

(297) Step (a) was carried out based on a simple graphical user interface, and step (b) was performed based on a specifically tailored motion-compensation algorithm. Both implementations were done in MATLAB. Based on the raw video and on a given rectangular region of interest, the algorithm outputs a motion-corrected capillary video applying a rigid registration technique; specifically, it aligns all video frames with the first one assuming that potential camera movements in the region of interest are mere combinations of X and Y translations, excluding rotations.

(298) While frame movements in the raw video can involve deformations, visual inspection of the registration results proved successful when applied to every capillary field of view separately. As a similarity metric and optimization criterion, the algorithm uses mutual information, which is a measure based on information theory that copes with slight contrast changes and guarantees accurate sub-pixel alignment. Prior to this registration process, a preliminary coarse-registration step is performed to ensure a suitable initialization. This initialization step performs frame pre-alignment based on cross-correlation analysis of pixel values and spatial gradients.

#### (299) Event Rating

(300) Based on a graphical user interface, three human raters followed specific visual criteria to identify all events in the capillary videos. Under this visual criteria, the consequence of the passage of a WBC through a capillary of approximately the same diameter includes creating a region depleted of RBCs. Specifically, moving optical-absorption gaps referred to as events having the following properties.

(301) In one example, the events are noticeably brighter than the surrounding capillary flow. In another example, the events can be identified as clear objects moving along the capillary flow. In yet another example, the events occupy the whole capillary diameter and extend along the flow

direction.

(302) Raters were blinded with respect to the others and to the corresponding blood-analytics, physiological state, patient, and temporal information. Each rater labeled the corresponding frames and spatial locations inside the capillary where these events happened.

(303) The indexing of the videos made available to the raters for event identification and counting was obtained by randomly shuffling the original-video names, thus rendering access to the original indexing impossible for the raters, though the corresponding content was similar. Furthermore, the amount of frames was always the same for all videos acquired from the same patient. No side information making such identification possible was included in the corresponding files. All videos—in non-shuffled and shuffled-index versions—were anonymized in the sense that no information in the video content and naming could be used to identify patients or neutropenic state. Following blind rating, all marked events could be visualized based on a specifically developed method.

(304) Statistical Analysis

(305) The counts obtained from all three independent raters allowed the determination of joint rating properties, i.e., whether one single expert, or whether two or more experts agreed on the same event being observed. By convention, it is assumed that at least  $R$  raters have jointly marked a given event if the average mark times from at least  $R$  raters lie within at most ten frames ( $\frac{1}{6}$  seconds) from each other, which is substantially smaller than expected event rates in capillary videos (see FIG. 46 below). Exact spatial overlay of the labels is not required. A specific case of interest is majority rater agreement, for which  $R$  is equal or greater than 2 in this setting, which yields validated events. Counts were then performed accordingly, i.e., summing events from every capillary video accordingly.

(306) Validated counts from several capillaries were combined for each patient (see FIG. 41 and FIGS. 44A and 44B below) because the precision of individual count values in single capillaries (a) is limited by shot noise, which is proportional to the square root of the amount of counts, (b) is limited by potential WBC phenomena not complying with the event criteria and occurring in some capillaries, such as margination, (c) is dependent on the particular capillary geometry and flow rate, and (d) is dependent on the particular positioning of the capillary on the underlying capillary-network dynamics. When considering count combinations of fixed amounts of capillaries per patient (FIGS. 44A and 44B), the corresponding sets of capillaries were picked randomly and results were computed based on 10,000 trials. This is akin to Monte-Carlo integration, and allowed to effectively handle the exponentially increasing amounts of cross-patient combinations that are otherwise intractable.

(307) When comparing the counts between capillaries or combined sets thereof, the analysis tools that was used was the Wilcoxon signed-rank test on the paired data, which avoids the statistical assumption that counts are normally distributed while testing/refuting the hypothesis  $H_0$  that there is no difference between counts obtained in baseline and severe neutropenia for the same capillaries. In addition, the study generated receiver operating characteristic (ROC) curves and corresponding area-under-curve (AUC) values, which tests the performance of binary-class classification between baseline and severe neutropenia as a function of a varying threshold count.

(308) Visualization of Marked Events

(309) In order to visualize marked events in capillaries, a method was developed to simultaneously visualize the frames of the capillary video of interest and the corresponding ST intensity profile of the capillary, both for the whole video duration and around a given frame. This allowed events to be visualized both explicitly as a moving object through the corresponding video frames and as a fixed profile in their ST map representation. In the context of the clinical study, this visualization technique allowed retrospective analysis of the distribution of labeled events in the videos as well as the relevance of majority rater agreement.

(310) The concept of a ST map for capillary-flow visualization was described above. It is motivated by the fact that events can be conveniently observed in that representation: events

associated with WBCs are expected to appear as thick, high-contrast, sparse, and unidirectional trajectories. These properties also relate to the visual criteria that were defined for the raters, e.g., event brightness. ST maps make the rater-marked events appear as well-defined salient trajectories surrounded by a darker background (see FIG. 39E above).

(311) To create the ST maps, the method extracts capillary brightness—as averaged over the cross-section—as a function of time and as a function of the cumulative capillary length, based on segmented capillary boundaries. In order to improve the visualization of event trajectories, the map values were normalized by subtracting their local temporal averages as obtained between 50 frames before and after every time point. The initial capillary-segmentation procedure was performed based on an image extracted from the corresponding registered video.

(312) Since the capillary profile may be incomplete in a single video frame due to the presence of absorption gaps in the flow, a temporally integrated image was extracted for nailfold capillaries, where temporally variable features associated with the capillary flow are also enhanced to maximize contrast between the capillary and its surroundings. This approach also relates to the concept of motion-contrast enhancement. Specifically, the image that were used for segmentation was obtained through the integration of temporal-frequency components whose periods were empirically chosen to lie in the [0.25, 1.5]-second interval.

(313) Capillary boundaries were first segmented manually in a first step, and then refined with the help of an active-contour technique. The segmentation of both capillary boundaries was then automatically resampled so as to include 1,000 points each, and such that the center of every point pair at the same index of both boundaries lies on the medial axis of the capillary, where the medial axis is the loci of all circles inscribed in the capillary. Finally, based on this segmentation, separations between the arterial limb, venous limb, and loop of the capillary were defined on a case-to-case basis for visualization (see FIGS. 45A-45C).

(314) Acquisition Time Under Shot Noise

(315) The video-acquisition time  $t$  was set to one minute because it remains suitable for clinical settings while being long enough to allow sampling significantly higher amounts of events  $N$  in baseline cases compared to severe-neutropenia cases. Even under the shot noise that originates from the quantized nature of events, the count distributions associated with both cases are expected to be disjoint within at least one standard deviation of their means  $N_{\text{sub.b}}$  and  $N_{\text{sub.n}}$ , respectively, as expected from the calculations detailed below.

(316) To determine this result, a worst-case scenario was considered using a lower-limit case for baseline ( $C_{\text{sub.b}}=1,500$  neutrophils/ $\mu\text{L}$ ) and a higher-limit case for severe neutropenia ( $C_{\text{sub.n}}=500$  neutrophils/ $\mu\text{L}$ ), which is most difficult to discriminate since the difference between cell concentrations  $C$  from both categories is minimized. Typical values from the literature were then assumed for capillary diameter ( $D=15\ \mu\text{m}$ ) and flow speed ( $v=800\ \mu\text{m/s}$ ), which allowed estimating expected amounts of events from concentrations. Specifically,  $N=\pi \cdot \text{Math.}$

$(D/2)_{\text{sup.2}} \cdot \text{Math.} \cdot C \cdot \text{Math.} \cdot v \cdot \text{Math.} \cdot t$ , which yields  $N_{\text{sub.b}}=4.24$  and  $N=12.72$ . Finally, the shot-noise statistics imply that counts vary around these means with standard deviations  $N_{\text{sub.b}}_{\text{sup.1/2}}=2.06$  and  $N_{\text{sub.n}}_{\text{sup.1/2}}=3.57$ , respectively. Potentially, this results in count ranges allowing for clear discrimination (see FIG. 46).

(317) FIG. 35 shows the number of events labeled by one single rater. Baseline counts not reaching agreement between two or more experts (blue dots), as obtained in the 98 capillaries of the study, do not display any statistically significant difference ( $P=0.12$ ; Wilcoxon signed rank) with respect to the corresponding counts in severe neutropenia (red squares). This result indicates that events labeled by single raters are less objective and contain less information than those with multiple-rater agreement. Capillary pairs are grouped by patient ID.

(318) FIGS. 44A and 44B show the discrimination between baseline and severe neutropenia using capillary aggregates. FIG. 44A shows the number of event counts resulting from integrating  $N=1, 2, 3, 4, 5$  capillaries per patient. FIG. 44B shows the ROC curves for classification of baseline vs.



severe neutropenia based on integrating  $N=1, 2, 3, 4, 5$  capillaries per patient. The patient-level distributions of the resulting count values show that their discriminatory power increases with the amount of combined capillaries per patient. Specifically, the minimum area under curve (AUC) consistently increases with the amount of combined capillaries from 0.61 to 0.84, 0.92, 0.96 and 1.00 when including 1, 2, 3, 4 and 5 capillaries, respectively.

(319) FIGS. **45A-45C** show example of a capillary segmentation. FIG. **45A** shows capillary from patient 02. FIG. **45B** shows the same capillary with supervised segmentation (red). The scale bar is 20  $\mu\text{m}$ . FIG. **45C** shows the separations between arterial limb (green), venous limb (blue), and loop (red) of the capillary can be defined on a case-to-case basis for visualization.

(320) FIG. **46** shows expected amounts of events per capillary minute under shot noise. Assuming typical capillary-diameter and speed values from the literature, amounts of expected events in baseline (blue; 1,500 neutrophils/ $\mu\text{L}$ ) exceed the corresponding amounts in severe neutropenia (red; 500 neutrophils/ $\mu\text{L}$ ) for a single minute of acquisition, even under shot noise. Shown are expected count averages (central dots) along with expected variations originating from shot noise up to one standard deviation (bars).

(321) FIG. **47** shows the distribution of capillary diameters at events positions. The distribution of the capillary-diameter values at the positions where the three blinded raters labeled an event is shown. Detected events tend to appear in capillary segments of approximately the same size range as WBCs, i.e., [10-20]  $\mu\text{m}$ , thus confirming observations made in prior literature and the usability of events as proxies of WBCs.

(322) FIGS. **48A** and **48B** show ST maps of capillaries with high versus low ratio ratios of validated events. For each event, the first click from each of the three human raters is displayed with a red, blue, and green dot, respectively. Inter-rater agreement was higher in baseline capillaries (top map) compared to the case of severe neutropenia (bottom map), indicating that events in baseline correspond to more objective physical phenomena.

(323) FIG. **49** shows capillary selection from both experts in raw-video pair from Patient 01, region 1. The videos acquired in baseline and severe-neutropenic states are displayed. The green boxes outline the selected capillary pairs which, according to each of the two experts complied with the quality criteria for both baseline and severe-neutropenia acquisitions. The red regions/capillaries are discarded due to non-compliance with the quality criteria, i.e., due in this instance to (b) lack of focus, (c) lack of blood flow, and (d) out-of-field-of-view movements. The red lines/corners in the baseline videos outline the effective field of view outside which capillaries must be discarded as they disappear during several frames due to camera movements during acquisition. The yellow boxes outline capillaries that were initially selected in baseline but were discarded later due to non-compliance in the severe-neutropenia acquisition (g). Both experts made the selection process independently and, after that, only capillaries where both experts agreed (black numbers), discarding the rest of them (red numbers).

(324) FIG. **50** shows capillary selection from both experts in raw-video pair from Patient 01, region 2. The videos acquired in baseline and severe-neutropenic states are displayed. The green boxes outline the selected capillary pairs which, according to each of the two experts complied with the quality criteria for both baseline and severe-neutropenia acquisitions. The red regions/capillaries are discarded due to non-compliance with the quality criteria, i.e., due in this instance to (b) lack of focus, (d) out-of-field-of-view movements, and (e) occlusions. The red lines/corners in the baseline videos outline the effective field of view outside which capillaries must be discarded as they disappear during several frames due to camera movements during acquisition. The yellow boxes outline capillaries that were initially selected in baseline but were discarded later due to non-compliance in the severe-neutropenia acquisition (g). Both experts made the selection process independently and, after that, only capillaries where both experts agreed (black numbers), discarding the rest of them (red numbers).

(325) FIG. **52** shows capillary selection from both experts in raw-video pair from Patient 02, region

1. The videos acquired in baseline and severe-neutropenic states are displayed. The green boxes outline the selected capillary pairs which, according to each of the two experts complied with the quality criteria for both baseline and severe-neutropenia acquisitions. The red regions/capillaries are discarded due to non-compliance with the quality criteria, i.e., due in this instance to (a) poor illumination, (b) lack of focus, (c) lack of blood flow, and (e) occlusions. The red lines/corners in the baseline videos outline the effective field of view outside which capillaries must be discarded as they disappear during several frames due to camera movements during acquisition. The yellow boxes outline capillaries that were initially selected in baseline but were discarded later due to non-compliance in the severe-neutropenia acquisition (g). Both experts made the selection process independently and, after that, only capillaries where both experts agreed (black numbers), discarding the rest of them (red numbers)

(326) FIG. 52 shows capillary selection from both experts in raw-video pair from Patient 02, region 2. The videos acquired in baseline and severe-neutropenic states are displayed. The green boxes outline the selected capillary pairs which, according to each of the two experts complied with the quality criteria for both baseline and severe-neutropenia acquisitions. The red regions/capillaries are discarded due to non-compliance with the quality criteria, i.e., due in this instance to (b) lack of focus, (c) lack of blood flow, (e) occlusions, and (f) lack of clear morphology. The red lines/corners in the baseline videos outline the effective field of view outside which capillaries must be discarded as they disappear during several frames due to camera movements during acquisition. The yellow boxes outline capillaries that were initially selected in baseline but were discarded later due to non-compliance in the severe-neutropenia acquisition (g). Both experts made the selection process independently and, after that, only capillaries where both experts agreed (black numbers), discarding the rest of them (red numbers).

(327) FIG. 53 shows capillary selection from both experts in raw-video pair from Patient 03. The videos acquired in baseline and severe-neutropenic states are displayed. The green boxes outline the selected capillary pairs which, according to each of the two experts complied with the quality criteria for both baseline and severe-neutropenia acquisitions. The red regions/capillaries are discarded due to non-compliance with the quality criteria, i.e., due in this instance to (a) poor illumination, (b) lack of focus, (c) lack of blood flow, (d) out-of-field-of-view movements, and (e) occlusions. The red lines/corners in the baseline videos outline the effective field of view outside which capillaries must be discarded as they disappear during several frames due to camera movements during acquisition. The yellow boxes outline capillaries that were initially selected in baseline but were discarded later due to non-compliance in the severe-neutropenia acquisition (g). Both experts made the selection process independently and, after that, only capillaries where both experts agreed (black numbers), discarding the rest of them (red numbers).

(328) FIG. 54 shows capillary selection from both experts in raw-video pair from Patient 04. The videos acquired in baseline and severe-neutropenic states are displayed. The green boxes outline the selected capillary pairs which, according to each of the two experts complied with the quality criteria for both baseline and severe-neutropenia acquisitions. The red regions/capillaries are discarded due to non-compliance with the quality criteria, i.e., due in this instance to (b) lack of focus. The red lines/corners in the baseline videos outline the effective field of view outside which capillaries must be discarded as they disappear during several frames due to camera movements during acquisition. The yellow boxes outline capillaries that were initially selected in baseline but were discarded later due to non-compliance in the severe-neutropenia acquisition (g). Both experts made the selection process independently and, after that, only capillaries where both experts agreed (black numbers), discarding the rest of them (red numbers).

(329) FIG. 55 shows capillary selection from both experts in raw-video pair from Patient 05. The videos acquired in baseline and severe-neutropenic states are displayed. The green boxes outline the selected capillary pairs which, according to each of the two experts complied with the quality criteria for both baseline and severe-neutropenia acquisitions. The red regions/capillaries are

discarded due to non-compliance with the quality criteria, i.e., due in this instance to (b) lack of focus, (c) lack of blood flow, (d) out-of-field-of-view movements, and (e) occlusions. The red lines/corners in the baseline videos outline the effective field of view outside which capillaries must be discarded as they disappear during several frames due to camera movements during acquisition. The yellow boxes outline capillaries that were initially selected in baseline but were discarded later due to non-compliance in the severe-neutropenia acquisition (g). Both experts made the selection process independently and, after that, only capillaries where both experts agreed (black numbers), discarding the rest of them (red numbers).

(330) FIG. **56** shows capillary selection from both experts in raw-video pair from Patient 06. The videos acquired in baseline and severe-neutropenic states are displayed. The green boxes outline the selected capillary pairs which, according to each of the two experts complied with the quality criteria for both baseline and severe-neutropenia acquisitions. The red regions/capillaries are discarded due to non-compliance with the quality criteria, i.e., due in this instance to (b) lack of focus, (c) lack of blood flow, (d) out-of-field-of-view movements, and (f) lack of clear morphology. The red lines/corners in the baseline videos outline the effective field of view outside which capillaries must be discarded as they disappear during several frames due to camera movements during acquisition. The yellow boxes outline capillaries that were initially selected in baseline but were discarded later due to non-compliance in the severe-neutropenia acquisition (g). Both experts made the selection process independently and, after that, only capillaries where both experts agreed (black numbers), discarding the rest of them (red numbers).

(331) FIG. **57** shows capillary selection from both experts in raw-video pair from Patient 07. The videos acquired in baseline and severe-neutropenic states are displayed. The green boxes outline the selected capillary pairs which, according to each of the two experts complied with the quality criteria for both baseline and severe-neutropenia acquisitions. The red regions/capillaries are discarded due to non-compliance with the quality criteria, i.e., due in this instance to (a) poor illumination, (b) lack of focus, (d) out-of-field-of-view movements, and (e) occlusions. The red lines/corners in the baseline videos outline the effective field of view outside which capillaries must be discarded as they disappear during several frames due to camera movements during acquisition. The yellow boxes outline capillaries that were initially selected in baseline but were discarded later due to non-compliance in the severe-neutropenia acquisition (g). Both experts made the selection process independently and, after that, only capillaries where both experts agreed (black numbers), discarding the rest of them (red numbers).

(332) FIG. **58** shows capillary selection from both experts in raw-video pair from Patient 08. The videos acquired in baseline and severe-neutropenic states are displayed. The green boxes outline the selected capillary pairs which, according to each of the two experts complied with the quality criteria for both baseline and severe-neutropenia acquisitions. The red regions/capillaries are discarded due to non-compliance with the quality criteria, i.e., due in this instance to (b) lack of focus, (d) out-of-field-of-view movements, (e) occlusions, and (f) lack of clear morphology. The red lines/corners in the baseline videos outline the effective field of view outside which capillaries must be discarded as they disappear during several frames due to camera movements during acquisition. The yellow boxes outline capillaries that were initially selected in baseline but were discarded later due to non-compliance in the severe-neutropenia acquisition (g). Both experts made the selection process independently and, after that, only capillaries where both experts agreed (black numbers), discarding the rest of them (red numbers).

(333) FIG. **59** shows capillary selection from both experts in raw-video pair from Patient 09. The videos acquired in baseline and severe-neutropenic states are displayed. The green boxes outline the selected capillary pairs which, according to each of the two experts complied with the quality criteria for both baseline and severe-neutropenia acquisitions. The red regions/capillaries are discarded due to non-compliance with the quality criteria, i.e., due in this instance to (a) poor illumination, (b) lack of focus, (c) lack of blood flow, and (e) occlusions. The red lines/corners in

the baseline videos outline the effective field of view outside which capillaries must be discarded as they disappear during several frames due to camera movements during acquisition. The yellow boxes outline capillaries that were initially selected in baseline but were discarded later due to non-compliance in the severe-neutropenia acquisition (g). Both experts made the selection process independently and, after that, only capillaries where both experts agreed (black numbers), discarding the rest of them (red numbers).

(334) FIG. **60** shows capillary selection from both experts in raw-video pair from Patient 10. The videos acquired in baseline and severe-neutropenic states are displayed. The green boxes outline the selected capillary pairs which, according to each of the two experts complied with the quality criteria for both baseline and severe-neutropenia acquisitions. The red regions/capillaries are discarded due to non-compliance with the quality criteria, i.e., due in this instance to (b) lack of focus, (d) out-of-field-of-view movements, and (f) lack of clear morphology. The red lines/corners in the baseline videos outline the effective field of view outside which capillaries must be discarded as they disappear during several frames due to camera movements during acquisition. The yellow boxes outline capillaries that were initially selected in baseline but were discarded later due to non-compliance in the severe-neutropenia acquisition (g). Both experts made the selection process independently and, after that, only capillaries where both experts agreed (black numbers), discarding the rest of them (red numbers).

(335) Each of the following references is incorporated herein by reference in their entirety. Tsukada, Kosuke, et al. "Image correlation method for measuring blood flow velocity in microcirculation: correlationwindow'simulation and in vivo image analysis." *Physiological measurement* 21.4 (2000): 459. Langeder, Florian, and Bernhard G. Zagar. "Image processing strategies to accurately measure red blood cell motion in superficial capillaries." *Systems, Signals and Devices*, 2009. SSD'09. 6th International Multi-Conference on. IEEE, 2009. Wu, Chih-Chieh, et al. "Red blood cell velocity measurements of complete capillary in finger nail-fold using optical flow estimation." *Microvascular research* 78.3 (2009): 319-324. Huang, Tzung-Chi, et al. "Experimental estimation of blood flow velocity through simulation of intravital microscopic imaging in micro-vessels by different image processing methods." *Microvascular research* 80.3 (2010): 477-483. Wu, Chih-Chieh, et al. "Accuracy evaluation of RBC velocity measurement in nail-fold capillaries." *Microvascular research* 81.3 (2011): 252-260. Lo, Lun-Chien, et al. "Pseudo three-dimensional vision-based nail-fold morphological and hemodynamic analysis." *Computers in biology and medicine* 42.9 (2012): 873-884. Wang, Mingyi, et al. "Full-field velocity imaging of red blood cells in capillaries with spatiotemporal demodulation autocorrelation." *Journal of biomedical optics* 21.3 (2016): 036007-036007. J. Crawford, D. C. Dale, and G. H. Lyman (2004). Chemotherapy-induced neutropenia: risks, consequences, and new directions for its management. *Cancer*, 100(2), 228-237. M. E. van Wolfswinkel, K. Vliegthart-Jongbloed, M. de Mendonça Melo, P. C. Wever, M. B. McCall, R. Koelewijn, J. J. van Hellemond, and P. J. van Genderen (2013). Predictive value of lymphocytopenia and the neutrophil-lymphocyte count ratio for severe imported malaria. *Malar. J.*, 12(1), 101. T. Honda, T. Uehara, G. Matsumoto, S. Arai, and M. Sugano (2016). Neutrophil left shift and white blood cell count as markers of bacterial infection. *Clin. Chim. Acta*, 457, 46-53. T. B. Newman, D. Draper, K. M. Puopolo, S. Wi, and G. J. Escobar (2014). Combining immature and total neutrophil counts to predict early onset sepsis in term and late preterm newborns: use of the I/T2. *Pediat. Infect. Dis. J.*, 33(8), 798. A. Velo-García, S. G. Castro, and D. A. Isenberg (2016). The diagnosis and management of the haematologic manifestations of lupus. *J. Autoimmun.*, 74, 139-160. D. C. Dale (2014). Understanding neutropenia. *Curr. Opin. Hematol.*, 21(1), 1-2. V. S. Hollis, J. A. Holloway, S. Harris, D. Spencer, C. van Berkel, and H. Morgan (2012). Comparison of venous and capillary differential leukocyte counts using a standard hematology analyzer and a novel microfluidic impedance cytometer. *PloS one*, 7(9), e43702. C. L. Ghai (2012). *A textbook of practical physiology*. JP Medical Ltd. S. Sharma, J. Zapatero-Rodriguez, P. Estrela, and R. O'Kennedy (2015). Point-of-care diagnostics in

low resource settings: present status and future role of microfluidics. *Biosensors*, 5(3), 577-601. Y. Mendelson (1992). Pulse oximetry: theory and applications for noninvasive monitoring. *Clin. Chem.*, 38(9), 1601-1607. A. Trotti, A. D. Colevas, A. Setser, V. Rusch, D. Jaques, V. Budach, C. Langer, B. Murphy, R. Cumberlin, C. N. Coleman, and P. Rubin (2003, July). CTCAE v3.0: development of a comprehensive grading system for the adverse effects of cancer treatment. In *Semin. Radiat. Oncol.* (Vol. 13, No. 3, pp. 176-181). WB Saunders. G. H. Lyman, M. S. Poniewierski, J. Crawford, D. C. Dale, and E. Culakova (2015). Cost of Hospitalization in Patients with Cancer and Febrile Neutropenia and Impact of Comorbid Conditions. *Blood*, 126(23), 2089-2089. G. H. Lyman, C. H. Lyman, O. Agboola, and Anc Study Group. (2005). Risk models for predicting chemotherapy-induced neutropenia. *Oncologist*, 10(6), 427-437. J. De Naurois, I. Novitzky-Basso, M. J. Gill, F. M. Marti, M. H. Cullen, F. Roila, and ESMO Guidelines Working Group. (2010). Management of febrile neutropenia: ESMO clinical practice guidelines. *Ann. Oncol.*, 21(suppl 5), v252-v256. G. W. Schmid-Schonbein, S. Usami, R. Skalak, and S. Chien (1980). The interaction of leukocytes and erythrocytes in capillary and postcapillary vessels. *Microvasc. Res.*, 19(1), 45-70. S. H. Sinclair, M. Azar-Cavanagh, K. A. Soper, R. F. Tuma, and H. N. Mayrovitz (1989). Investigation of the source of the blue field entoptic phenomenon. *Invest. Ophthalmol. Vis. Sci.*, 30(4), 668-673. A. Roggan, M. Friebe, K. Dorschel, A. Hahn, and G. Muller (1999). Optical properties of circulating human blood in the wavelength range 400-2500 nm. *J. Biomed. Opt.*, 4(1), 36-46. A. Uji, M. Hangai, S. Ooto, K. Takayama, N. Arakawa, H. Imamura, K. Nozato, and N. Yoshimura (2012). The source of moving particles in parafoveal capillaries detected by adaptive optics scanning laser ophthalmoscopy. *Invest. Ophthalmol. Vis. Sci.*, 53(1), 171-178. U. Schmidt-Gross (1954). Entoptische Beurteilung der Leukocytenzahl. *Klin. Wochenschr.*, 32(33-34), 817-819. T. Rimmer, E. M., Kohner, and J. M. Goldman (1988). Retinal blood velocity in patients with leukocyte disorders. *Arch. Ophthalmol.*, 106(11), 1548-1552. G. Fuchsjager-Mayrl, M. Malec, E. Polska, B. Jilma, M. Wolzt, and L. Schmetterer (2002). Effects of granulocyte colony stimulating factor on retinal leukocyte and erythrocyte flux in the human retina. *Invest. Ophthalmol. Vis. Sci.*, 43(5), 1520-1524. C. E. Curtis, W. G. Iacono, and M. Beiser (1999). Relationship between nailfold plexus visibility and clinical, neuropsychological, and brain structural measures in schizophrenia. *Biol. Psychiatry*, 46(1), 102-109. F. Lefford and J. C. Edwards (1986). Nailfold capillary microscopy in connective tissue disease: a quantitative morphological analysis. *Ann. Rheum. Dis.*, 45(9), 741-749. Z. Nagy and L. Czirjak (2004). Nailfold digital capillaroscopy in 447 patients with connective tissue disease and Raynaud's disease. *J. Eur. Acad. Dermatol. Venereol.*, 18(1), 62-68. L. K. Mercer, T. L. Moore, H. Chinoy, A. K. Murray, A. Vail, R. G. Cooper, and A. L. Herrick (2010). Quantitative nailfold video capillaroscopy in patients with idiopathic inflammatory myopathy. *Rheumatology*, 49(9), 1699-1705. A. K. Murray, A. Vail, T. L. Moore, J. B. Manning, C. J. Taylor, and A. L. Herrick (2012). The influence of measurement location on reliability of quantitative nailfold videocapillaroscopy in patients with SSc. *Rheumatology*, 51(7), 1207-1214. H. M. Hofstee, E. H. Sernd, C. Roberts, R. Hesselstrand, A. Scheja, T. L. Moore, M. Wildt, J. B. Manning, A. V. Noordegraaf, A. E. Voskuyl, and A. L. Herrick (2011). A multicentre study on the reliability of qualitative and quantitative nail-fold videocapillaroscopy assessment. *Rheumatology*, 50(4), 643-650. S. J. Simnett, L. A. Stewart, J. Sweetenham, G. Morgan, and P. W. Johnson (2000). Autologous stem cell transplantation for malignancy: a systematic review of the literature. *Clin. Lab. Haematol.*, 22(2), 61-72. L. Golan, D. Yeheskely-Hayon, L. Minai, E. J. Dann, and D. Yelin (2012). Noninvasive imaging of flowing blood cells using label-free spectrally encoded flow cytometry. *Biomed. Opt. Express*, 3(6), 1455-1464. N. Mugii, M. Hasegawa, Y. Hamaguchi, C. Tanaka, K. Kaji, K. Komura, I. Ueda-Hayakawa, S. Horie, M. Ikuta, K. Tachino, F. Ogawa, S. Sato, M. Fujimoto, and K. Takehara (2009). Reduced red blood cell velocity in nail-fold capillaries as a sensitive and specific indicator of microcirculation injury in systemic sclerosis. *Rheumatology*, 48(6), 696-703. A. Bourquard, I. Butterworth, A. Sinchez-Ferro, L. Giancardo, L. Soenksen, C. Cerrato, R. Flores, and C. Castro-Gonzalez (2015, August). Analysis of white blood

cell dynamics in nailfold capillaries. In Conf. Proc. IEEE Eng. Med. Biol. Soc., 2015 37th Annual International Conference of the IEEE (pp. 7470-7473). C. Castro-Gonzalez, I. Butterworth, A. Bourquard, and A. Sanchez-Ferro (2015). Systems, apparatus, and methods for analyzing blood cell dynamics. U.S. patent application Ser. No. 14/951,260. C. C. Wu, G. Zhang, T. C. Huang, and K. P. Lin (2009). Red blood cell velocity measurements of complete capillary in finger nail-fold using optical flow estimation. *Microvasc. Res.*, 78(3), 319-324. T. C. Huang, W. C. Lin, C. C. Wu, G. Zhang, and K. P. Lin (2010). Experimental estimation of blood flow velocity through simulation of intravital microscopic imaging in micro-vessels by different image processing methods. *Microvasc. Res.*, 80(3), 477-483. C. C. Wu, W. C. Lin, G. Zhang, C. W. Chang, R. S. Liu, K. P. Lin, and T. C. Huang (2011). Accuracy evaluation of RBC velocity measurement in nail-fold capillaries. *Microvasc. Res.*, 81(3), 252-260. C. H. Wu, T. D. Wang, C. H. Hsieh, S. H. Huang, J. W. Lin, S. C. Hsu, H. T. Wu, Y. M. Wu, and T. M. Liu (2016). Imaging Cytometry of Human Leukocytes with Third Harmonic Generation Microscopy. *Sci. Rep.*, 6. T. C. Shih, G. Zhang, C. C. Wu, H. D. Hsiao, T. H. Wu, K. P. Lin, and T. C. Huang (2011, January). Hemodynamic analysis of capillary in finger nail-fold using computational fluid dynamics and image estimation. *Microvasc. Res.* 81(1), 68-72. D. Mattes, D. R. Haynor, H. Vesselle, T. K. Lewellyn, and W. Eubank (2001, July). Nonrigid multimodality image registration. In *Med. Imaging* (pp. 1609-1620). International Society for Optics and Photonics. G. W. Schmid-Schonbein, R. Skalak, S. Usami, and S. Chien (1980). Cell distribution in capillary networks. *Microvasc. Res.*, 19(1), 18-44. J. H. Lee, J. Jiménez, I. R. Butterworth, C. Castro-González, S. K. Shukla, B. Marti-Fuster, L. Elvira, D. S. Boning, and B. W. Anthony (2015, October). Measurement of very low concentration of microparticles in fluid by single particle detection using acoustic radiation force induced particle motion. In 2015 *IEEE Int. Ultrason. Symp.* (pp. 1-4). J. Tam, P. Tiruveedhula, and A. Roorda (2011). Characterization of single-file flow through human retinal parafoveal capillaries using an adaptive optics scanning laser ophthalmoscope. *Biomed. Opt. Express*, 2(4), 781-793. P. D. Allen, C. J. Taylor, A. L. Herrick, and T. Moore (1998, September). Enhancement of Temporally Variable Features in Nailfold Capillary Patterns. In *BMVC* (pp. 1-10). M. Kass, A. Witkin, and D. Terzopoulos (1988). Snakes: Active contour models. *Int. J. Comput. Vision*, 1(4), 321-331.

## CONCLUSION

(336) While various inventive embodiments have been described and illustrated herein, those of ordinary skill in the art will readily envision a variety of other means and/or structures for performing the function and/or obtaining the results and/or one or more of the advantages described herein, and each of such variations and/or modifications is deemed to be within the scope of the inventive embodiments described herein. More generally, those skilled in the art will readily appreciate that all parameters, dimensions, materials, and configurations described herein are meant to be exemplary and that the actual parameters, dimensions, materials, and/or configurations will depend upon the specific application or applications for which the inventive teachings is/are used. Those skilled in the art will recognize, or be able to ascertain using no more than routine experimentation, many equivalents to the specific inventive embodiments described herein. It is, therefore, to be understood that the foregoing embodiments are presented by way of example only and that, within the scope of the appended claims and equivalents thereto, inventive embodiments may be practiced otherwise than as specifically described and claimed. Inventive embodiments of the present disclosure are directed to each individual feature, system, article, material, kit, and/or method described herein. In addition, any combination of two or more such features, systems, articles, materials, kits, and/or methods, if such features, systems, articles, materials, kits, and/or methods are not mutually inconsistent, is included within the inventive scope of the present disclosure.

(337) The above-described embodiments can be implemented in any of numerous ways. For example, embodiments disclosed herein may be implemented using hardware, software or a combination thereof. When implemented in software, the software code can be executed on any

suitable processor or collection of processors, whether provided in a single computer or distributed among multiple computers.

(338) Further, it should be appreciated that a computer may be embodied in any of a number of forms, such as a rack-mounted computer, a desktop computer, a laptop computer, or a tablet computer. Additionally, a computer may be embedded in a device not generally regarded as a computer but with suitable processing capabilities, including a Personal Digital Assistant (PDA), a smart phone or any other suitable portable or fixed electronic device.

(339) Also, a computer may have one or more input and output devices. These devices can be used, among other things, to present a user interface. Examples of output devices that can be used to provide a user interface include printers or display screens for visual presentation of output and speakers or other sound generating devices for audible presentation of output. Examples of input devices that can be used for a user interface include keyboards, and pointing devices, such as mice, touch pads, and digitizing tablets. As another example, a computer may receive input information through speech recognition or in other audible format.

(340) Such computers may be interconnected by one or more networks in any suitable form, including a local area network or a wide area network, such as an enterprise network, and intelligent network (IN) or the Internet. Such networks may be based on any suitable technology and may operate according to any suitable protocol and may include wireless networks, wired networks or fiber optic networks.

(341) The various methods or processes outlined herein may be coded as software that is executable on one or more processors that employ any one of a variety of operating systems or platforms. Additionally, such software may be written using any of a number of suitable programming languages and/or programming or scripting tools, and also may be compiled as executable machine language code or intermediate code that is executed on a framework or virtual machine.

(342) Also, various inventive concepts may be embodied as one or more methods, of which an example has been provided. The acts performed as part of the method may be ordered in any suitable way. Accordingly, embodiments may be constructed in which acts are performed in an order different than illustrated, which may include performing some acts simultaneously, even though shown as sequential acts in illustrative embodiments.

(343) All publications, patent applications, patents, and other references mentioned herein are incorporated by reference in their entirety.

(344) All definitions, as defined and used herein, should be understood to control over dictionary definitions, definitions in documents incorporated by reference, and/or ordinary meanings of the defined terms.

(345) The indefinite articles “a” and “an,” as used herein in the specification and in the claims, unless clearly indicated to the contrary, should be understood to mean “at least one.”

(346) The phrase “and/or,” as used herein in the specification and in the claims, should be understood to mean “either or both” of the elements so conjoined, i.e., elements that are conjunctively present in some cases and disjunctively present in other cases. Multiple elements listed with “and/or” should be construed in the same fashion, i.e., “one or more” of the elements so conjoined. Other elements may optionally be present other than the elements specifically identified by the “and/or” clause, whether related or unrelated to those elements specifically identified. Thus, as a non-limiting example, a reference to “A and/or B”, when used in conjunction with open-ended language such as “comprising” can refer, in one embodiment, to A only (optionally including elements other than B); in another embodiment, to B only (optionally including elements other than A); in yet another embodiment, to both A and B (optionally including other elements); etc.

(347) As used herein in the specification and in the claims, “or” should be understood to have the same meaning as “and/or” as defined above. For example, when separating items in a list, “or” or “and/or” shall be interpreted as being inclusive, i.e., the inclusion of at least one, but also including

more than one, of a number or list of elements, and optionally, additional unlisted items. Only terms clearly indicated to the contrary, such as “only one of” or “exactly one of,” or, when used in the claims, “consisting of,” will refer to the inclusion of exactly one element of a number or list of elements. In general, the term “or” as used herein shall only be interpreted as indicating exclusive alternatives (i.e. “one or the other but not both”) when preceded by terms of exclusivity, such as “either,” “one of,” “only one of,” or “exactly one of” “Consisting essentially of,” when used in the claims, shall have its ordinary meaning as used in the field of patent law.

(348) As used herein in the specification and in the claims, the phrase “at least one,” in reference to a list of one or more elements, should be understood to mean at least one element selected from any one or more of the elements in the list of elements, but not necessarily including at least one of each and every element specifically listed within the list of elements and not excluding any combinations of elements in the list of elements. This definition also allows that elements may optionally be present other than the elements specifically identified within the list of elements to which the phrase “at least one” refers, whether related or unrelated to those elements specifically identified. Thus, as a non-limiting example, “at least one of A and B” (or, equivalently, “at least one of A or B,” or, equivalently “at least one of A and/or B”) can refer, in one embodiment, to at least one, optionally including more than one, A, with no B present (and optionally including elements other than B); in another embodiment, to at least one, optionally including more than one, B, with no A present (and optionally including elements other than A); in yet another embodiment, to at least one, optionally including more than one, A, and at least one, optionally including more than one, B (and optionally including other elements); etc.

(349) In the claims, as well as in the specification above, all transitional phrases such as “comprising,” “including,” “carrying,” “having,” “containing,” “involving,” “holding,” “composed of,” and the like are to be understood to be open-ended, i.e., to mean including but not limited to. Only the transitional phrases “consisting of” and “consisting essentially of” shall be closed or semi-closed transitional phrases, respectively, as set forth in the United States Patent Office Manual of Patent Examining Procedures, Section 2111.03.

## Claims

1. A system for non-invasive in vivo hematological measurement, the system comprising: a platform to receive a body portion of a user during use, the body portion having capillary structure; an imaging device coupled to the platform and to acquire a time-lapse series of images of the capillary structure, wherein each image resolves multiple capillaries; and an imaging objective coupled to the imaging device, wherein the imaging device is configured to provide the time-lapse series of images of the capillary structure to a controller; and the controller that is adapted to: process the time-lapse series of images to perform the hematological measurement for one or more capillaries of the multiple capillaries, wherein the hematological measurement comprises: detecting passage, along a length of a capillary of the one or more capillaries, of a cell that produces a contrast in optical absorption relative to red blood cells in the capillary in the time-lapse series of images; and generating an event count for the capillary based on detected cellular events for the capillary, wherein a cellular event of the detected cellular events is associated with the passage of the cell along the length of the capillary.

2. The system of claim 1, wherein the cell is a circulating tumor cell or a white blood cell (WBC).

3. The system of claim 1, wherein the cell is a WBC and the controller is further adapted to: generate the event count based on the detected cellular events in the one or more capillaries, wherein each cellular event of the detected cellular events is associated with passage of a type of WBC in the capillary of the one or more capillaries; compare the event count to an event count threshold associated with a minimum number of cellular events for classification of the user to a first user type, wherein the one or more capillaries comprises those capillaries having a diameter



selected to be approximately equal to or less than a diameter of any WBC of the one or more types of WBCs; and classify, based on the event count comparison to the event count threshold, the user to a first user type of a set of user types, at least one user type of the set of user types associated with a condition of neutropenia.

4. The system of claim 3, wherein the controller is further adapted to detect each cellular event of the cellular events by detecting an optical absorption gap during passage of the one or more types of WBCs in the capillary of the one or more capillaries.

5. The system of claim 3, wherein the controller is further adapted to: detect each cellular event of the detected cellular events based on the contrast in absorption relative to red blood cells.

6. The system of claim 3, further comprising an illumination source (**2320**) to illuminate the capillary structure with blue light.

7. The system of claim 3, wherein the diameter is from 10 microns to 20 microns.

8. The system of claim 3, wherein the controller is further adapted to apply the time-lapse series of images to a neural network to identify the one or more capillaries.

9. The system of claim 3, wherein the controller is further adapted to: receive a set of training images associated with capillary beds in body portions of a set of training users; and generate, via supervised learning, the event count threshold based on the set of training images.

10. The system of claim 3, wherein the controller is further adapted to: generate a bounding box for each detected capillary in each image of the time-lapse series of images; generate a confidence value associated with a likelihood that detection of the detected capillary corresponds to a capillary and not another structure/artifact; and include the detected capillary in the one or more capillaries if the confidence value meets or exceeds a predetermined confidence threshold.

11. The system of claim 3, wherein the controller is further adapted to: apply a band-pass filter in the discrete Fourier domain, the band-pass filter having a low-frequency band-pass parameter and a high-frequency band-pass parameter fitting a range of expected cellular event sizes.

12. The system of claim 3, wherein the controller is further adapted to: compile profiles extracted from the time-lapse series of images into at least one spatiotemporal profile to analyze WBC events for a capillary of the one or more capillaries.

13. The system of claim 12, wherein the controller is further adapted to determine a flow speed of WBCs from the at least one spatiotemporal profile.

14. The system of claim 12, wherein the controller is further adapted to determine a total number of WBC events per microliter from the at least one spatiotemporal profile.

15. A method for non-invasive in vivo hematological measurement, the method comprising: receiving on a platform a body portion of a user, the body portion having capillary structure; acquiring, with an imaging device comprising an imaging objective, a time-lapse series of images of the capillary structure, wherein each image resolves multiple capillaries; providing the time-lapse series of images of the capillary structure to a controller, wherein the controller is communicatively coupled to the imaging device; and processing, by the controller, the time-lapse series of images to perform the hematological measurement for one or more capillaries of the multiple capillaries, wherein the hematological measurement comprises: detecting passage, along a length of a capillary of the one or more capillaries, of a cell that produces a contrast in optical absorption relative to red blood cells in the capillary in the time-lapse series of images; and generating, by the controller, an event count for the capillary based on detected cellular events for the capillary, wherein a cellular event of the detected cellular events is associated with the passage of the cell along the length of the capillary.

16. The method of claim 15, wherein the cell is a circulating tumor cell or a white blood cell (WBC).

17. The method of claim 15, further comprising: generating, by the controller, the event count based on the detected cellular events in the one or more capillaries, wherein each cellular event of the detected cellular events is associated with passage of a type of WBC in the capillary of the one

or more capillaries; comparing, by the controller, the event count to an event count threshold associated with a minimum number of cellular events for classification of the user to a first user type, wherein the one or more capillaries comprises those capillaries having a diameter selected to be approximately equal to or less than a diameter of any WBC of the one or more types of WBCs; and classifying, by the controller, based on the event count comparison to the event count threshold, the user to a first user type of a set of user types, at least one user type of the set of user types associated with a condition of neutropenia.

18. The method of claim 17, further comprising: detecting, by the controller, each cellular event of the detected cellular events based on the contrast in absorption relative to red blood cells.

19. The method of claim 17, further comprising: receiving, by the controller, a set of training images associated with capillary beds in body portions of a set of training users; and generating, via supervised learning, the event count threshold based on the set of training images.

20. The method of claim 17, further comprising: generating, by the controller, a bounding box for each detected capillary in each image of the time-lapse series of images; generating, by the controller, a confidence value associated with a likelihood that detection of the detected capillary corresponds to a capillary and not another structure/artifact; and including, by the controller, the detected capillary in the one or more capillaries if the confidence value meets or exceeds a predetermined confidence threshold.

---